# Supramolecular Organization of the Antimicrobial Peptide Alamethicin in Fluid Membranes

Doctoral Thesis
2009

Jianjun Pan

Advisor
Prof. John F. Nagle

Department of Physics
Carnegie Mellon University, Pittsburgh, PA 15213

# Abstract

The antimicrobial peptide alamethicin (Alm) is well known to form ion channels (peptide bundles) in lipid membranes. Due to its simple chemical structure and complex electrical properties, Alm serves as a model for describing intrinsic ion channels in mammalian systems. In this thesis we investigated the supramolecular organization of Alm in fluid lipid model membranes by using x-ray scattering.

Oriented multilayer samples of Alm/lipid mixtures are used in this thesis. When the hydration level is sufficiently high, the interactions between the peptide bundles in different layers are negligible. Bragg rod shaped in-plane scattering side peaks caused by Alm bundles are obtained. To account for the positional correlations between the peptide bundles in a single bilayer, a hard disk model with and without long distance interactions is considered. The $q_r$ dependence of the form factor, which is the Fourier transform of the electron density distribution of the peptide bundle, is modeled in two ways. One approximates the bundle as a cylinder (solid bundle) and the other uses the bundle structure from molecular dynamics simulations (MD bundle). The lateral in-plane scattering intensity is fit by the product of the structure factor and the form factor. The fitting results indicate that the number N of peptides per bundle is 6 in DOPC and $N \geq 8$ in diC22:1PC. The difference is well described by the hydrophobic matching mechanism.

When the Alm/lipid sample is progressively dehydrated, the maximum position of

the side peaks shifts away from the equator ($q_z$=0). This is consistent with repulsive interactions at short distances between peptide bundles in different layers. The observed shifting is demonstrated by two types of correlations between neighboring layers, a hard disk correlation and a Lennard-Jones type correlation. Crystal like scattering peaks are obtained by removing most of the water molecules from the sample. The scattering pattern does not fit the proposed hexagonal close-packed or the rhombohedral structure. The pattern was better fit by the body centered tetragonal and the monoclinic structure.

A second diffuse peak located at $q_r$ ~0.7 $Å^{-1}$ is obtained in well-hydrated samples of both DOPC and diC22:1PC at all peptide concentrations. A phase separated 2-D hexagonal packing cluster model in equilibrium with Alm bundles is proposed.

# Acknowledgements

I am deeply grateful to my thesis advisor Prof. John Nagle. He has been very patient in guiding me through my graduate study. Thanks to him I am now used to think more about why and how than just what to do.

I am in deep debt to Prof. Stephanie Tristram-Nagle. Without her beautiful sample the project of this thesis would be impossible. She has also been very encouraging during the process of this thesis. Her expertise in scientific writing has been a great help in improving my writing skills. I also owe great debt to Dr. Thalia T. Mills. She has been extremely helpful in improving my programming skills using matlab. Without her method of wide angle x-ray scattering analysis, I would probably end up with far less papers. She has also been very helpful in improving my language skills. I am very grateful to Prof. Randall Feenstra. He shaped my idea of how to be a good experimenter. I also leaned a lot of experimental skills by working in his lab for one and half years. I thank my collaborator Prof. Peter Tieleman. He has been very kind to provide me results from MD simulations which are part of the analysis in this thesis. My thanks also go to other colleagues, Drs. Richard Epand, Evan Evans, Edgar Kooijman, Norbert Kučerka, John Mathai, Georg Pabst, Jonathan Sachs, Huey Huang, and Mark Zeidel. I thank the CHESS staff members, especially Dr. Arthur Woll, for their help with the synchrotron experiments. I would also like to thank professors Markus Deserno, Stephen Garoff, Mathias Lösche, Robert Suter, and Pei Tang. They have been very helpful and

encouraging during the process of this thesis.

I thank the professors in this physics department, Roy Briere, Thomas Ferguson, Gregg Franklin, Kunal Ghosh, Fred Gilman, Robert Griffiths, Richard Holman, Leonard Kisslinger, Ling-Fong Li, Sara Majetich, Manfred Paulini, Brian Quinn, James Russ, and Robert Swendsen. They have been very helpful in guiding my study and my life at CMU. My thanks also go to the staff, Albert Brunk, Patrick Carr, Charles Gitzen, Hillary Homer, Mary Jane Hutchison, Mary Placeway, Donna Thomas, Gary Wilkin, and Laura Youree. They have made my study at CMU enjoyable. I thank Dr. Florin Manolache for his expertise in Linux OS.

Special thanks to my friends Changshi Xiao, Yi Yang, Li Yu, Yang Dong, Tiandan Chen, Shu Nie, Yi Ding, Xiaohui Liu, Lulin Yu, Jun Zhao, Lei Wang, Chunlei Liu, Nanjun Chu, Peng Zheng, Libo Xie, Sandeep Gaan, Dong Joo Kim, Nadia Akhunzada, Pradeep Uppamoochikkal, Yuriy Zubovski, Deren Guler, Dipon Ghosh, Rob Chen, Radu Moldovan, Gabriel Altay, and Benjamin Beppler.

Last but not least, I thank my family, especially my wife Yuli Wei, for their selfless support.

# Contents

# List of Figures

# List of Tables

# Glossary

| | | |
|---|---|---|
| 2-D | two dimensional | 4 |
| 3-D | three dimensional | 9 |
| a | inside radius of Alm bundle | 64 |
| $a_1$,$a_2$,$a_3$ | primitive vectors | 100 |
| AA | all atom | 155 |
| AB | hexagonal AB stacking | 4 |
| ABC | hexagonal ABC stacking | 4 |
| Alm | alamethicin | 1 |
| AMPs | antimicrobial peptides | 5 |
| A(q) | scattering amplitude | 40 |
| b | outside radius of Alm bundle | 64 |
| $b_1$,$b_2$,$b_3$ | reciprocal primitive vector | 100 |
| BAM | Brewster angle microscopy | 164 |
| BCT | body centered tetragonal | 105 |
| CCD | charged coupled device/x-ray dector | 14 |
| CG | course grained | 155 |
| Chol | cholesterol | 163 |
| CHESS | Cornell high Energy Synchrotron Source | 16 |
| diC22:1PC | 1,2-dierucoyl-*sn*-glycero-phosphatidylcholine | 3 |
| D | lamellar repeat spacing | 9 |

| | | |
|---|---|---|
| $D_C$ | hydrocarbon thickness | 91 |
| DLPC | 1,2-dilauroyl-*sn*-glycerol-phosphatidylcholine | 163 |
| DMPC | 1,2-dimyristoyl-*sn*-glycerol-phosphatidylcholine | 71 |
| DOPC | 1,2-dioleoyl-*sn*-glycero-phosphatidylcholine | 3 |
| DOPE | 1,2-dioleoyl-*sn*-glycero- phosphatidylethanolamine | 163 |
| DPPC | 1,2-dipalmitoyl-*sn*-glycerol-phosphatidylcholine | 10 |
| $D_W$ | water spacing between neighboring bilayers | 33 |
| EPR | electron paramagnetic resonance | 4 |
| F(q) | form factor | 40 |
| GUV | Giant unilamellar vesicle | 163 |
| h | height of Alm/hydrophobic thickness | 48/91 |
| H,K,L | Miller indices | 101 |
| I(q) | scattering intensity | 40 |
| $J_0$ | zeroth order Bessel function of the first kind | 142 |
| $J_1$ | first order Bessel function of the first kind | 49 |
| $K_A$ | area stretch modulus | 91 |
| $K_C$ | bending modulus | 91 |
| LAXS | low angle x-ray scattering | 16 |
| L-J | Lennard-Jones | 49 |
| MC | Monte Carlo | 9 |
| MD | molecular dynamics | 4 |
| MLV | multilamellar vesciles | 9 |

| | | |
|---|---|---|
| Mo | molybdenum | 21 |
| n(r) | radial pair distribution function | 42 |
| N | number of peptides per bundle/number of disks | 1/31 |
| NMR | nuclear magnetic resonance | 3 |
| P | pitch length | 159 |
| PC | phosphatidylcholine | 2 |
| PE | phosphatidylethanolamine | 2 |
| POPC | 1-palmitoyl-2-oleoyl-*sn*-glycerol-phosphatidylcholine | 77 |
| **q** | scattering vector in the reciprocal space | 106 |
| $q_r$ | scattering vector along parallel to bilayer | 37 |
| $q_z$ | scattering vector along bilayer normal | 21 |
| r | peptide radius | 46 |
| R | hard disk radius | 46 |
| $R_h$ | helical radius | 159 |
| RSS | residual sum of squares | 72 |
| S | sample to CCD distance | 23 |
| S(q) | structure factor | 41 |
| $S_{0,0}(q)$ | structure factor in a single bilayer | 45 |
| $S_{1,0}(q)$ | structure factor between neighboring bilayers | 45 |
| SOPC | 1-stearoyl-2-oleoyl-*sn*-glycerol-phosphatidylcholine | 163 |
| TLC | thin layer chromatography | 6 |
| TM | transmembrane | 4 |

| | | |
|---|---|---|
| V(r) | interaction potential | 30 |
| WAXS | wide angle x-ray scattering | 16 |
| $\alpha$ | glancing angle | 16 |
| $\xi$ | lipid range affected by peptide incorporation | 97 |
| $\varepsilon$ | amplitude of Lennar-Jones potential | 50 |
| $\sigma$ | length scale of L-J interaction/decay length of Gaussian repulsion | 50/74 |
| $\lambda$ | wavelength | 22 |
| $\eta$ | area packing fraction | 31 |
| $\rho_P$ | peptide electron density | 56 |
| $\rho_W$ | water electron density | 64 |
| $\rho_C$ | hydrocarbon chain electron density | 64 |
| $\rho_H$ | headgroup electron density | 64 |
| $\rho_L$ | lipid electron density | 56 |

# Chapter 1

## Motivation for study and overview of alamethicin

### 1.1 Motivation for study

Extensive studies on membrane-protein systems have revealed that the cell membrane does not provide just a passive matrix, but rather plays an essential role in shaping the energetics and kinetics as well as distribution of integral proteins [1, 2]. One such mechanism is through membrane deformation caused by hydrophobic coupling between the hydrophobic core of the lipid membrane and the protein's hydrophobic domain [3]. The incurred energy cost of such deformation depends on membrane thickness, bending elasticity, area stretch modulus, and intrinsic curvature [4-6]. As a result, protein function can be modulated by varying the membrane mechanical and structural properties [7].

One particular interest in this thesis is to investigate how the size distribution of the ion channels formed by the antimicrobial peptide alamethicin (Alm) changes as a function of lipid properties. Both macroscopic [8-14] and single channel [15-17] conductance measurements have shown that the conductance behavior of the Alm channel depends on lipid properties. A particular example is that when Alm was incorporated into a series of monoglyceride/squalene membranes with chain length ranging from monomyristolein (14 carbons) to monoeicosaenoein (20 carbons), the apparent mean number of peptides per channel N increases as the membrane thickness

increases [12]. A larger probability for higher conductance states (larger N) has also been observed when Alm inserts into PE lipids which have a smaller headgroup than the typical bilayer forming PC lipids [18].

Several mechanisms have been proposed to account for the lipid property influence on peptide aggregate size distribution. By ignoring the thickness mismatch, line tension calculations suggested that the non-ideal cylindrically shaped inclusions can distort the neighboring lipid molecules. Because the distortion depends on the lipid spontaneous curvature and the bending modulus, this will give rise to the observed lipid dependent aggregate size distribution [19]. Unlike the line tension which focuses on the lipid molecules in the vicinity of the aggregate, the lateral stress coupled with the lateral excluded area of the peptide aggregate have also been suggested to be responsible for the lipid effect on the aggregate size distribution [20]. It has also been suggested that the average number of peptides present in an aggregate depends on the degree of mismatch of the hydrophobic thickness between the peptide inclusions and the lipid bilayer [21].

Stable channels through which the antimicrobial activity of Alm is carried out have also been observed by applying neutron [22, 23] and x-ray [24, 25] scattering techniques where no external voltage was present. These stable channels are different from the dynamic single channels in the conductance measurements [24]. However, the results of the stable channel size are difficult to reconcile due to the different techniques and sample preparation methods. Our first mission of this thesis is to investigate the effects of lipid

properties on the stable Alm channel size by using two lipid model membranes, DOPC and diC22:1PC shown in Fig. 1.1 which have different bilayer thickness by ~7 Å.

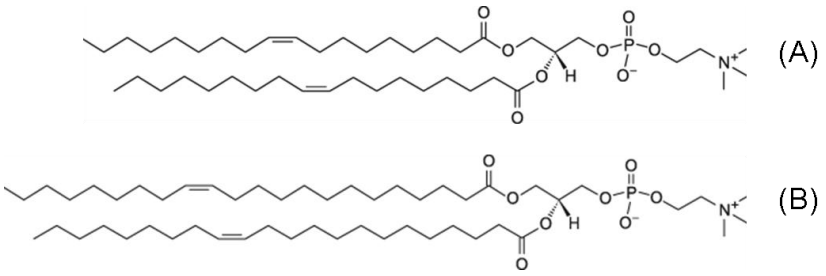


Figure 1.1: Lipid structures of (A) DOPC and (B) diC22:1PC (images from Avanti Polar Lipids).

The vast interest in the antimicrobial peptide Alm has lasted for more than 40 years, during which many of its intriguing electrical and structural properties have been discovered and a number of models concerning its voltage-gating mechanisms have been proposed (see review articles [16, 26-31]). Many such channel models are based on the crystal structure [32, 33] and the structure obtained from NMR [34] with the assumption of a barrel-stave like arrangement of the multimonomeric channel [35]. It is very difficult to obtain direct structural information of the ion channel in lipid membranes. One major problem is the fluid-like lipid membrane environment with thermal fluctuations that abolishes the higher scattering orders needed for high resolution structural characterization [36].

To alleviate this difficulty one may dehydrate the sample and consequently decrease

the fluctuations of the lipid membranes [37]. Indeed, crystal-like scattering from antimicrobial peptides, magainin and protegrin, embedded in lipid model membranes has been observed at low hydration conditions [38]. Based on the scattering patterns, several packing structures have been suggested including hexagonal close-packed (hexagonal AB stacking) structure [39], rhombehedral (hexagonal ABC stacking) structure [24, 38], and 2-D monoclinic structure [38]. However, only a few orders in the in-plane direction were observed. This limitation not only makes the packing structure determination ambiguous (several packing structures can fit the same set of data) but also causes the electron density construction in the in-plane direction difficult. The second mission of this thesis is to explore the Alm packing structure in lipid model membranes at very dehydrated conditions by applying a transmission scattering setup.

A recent molecular dynamics (MD) simulation study showed that Alm forms a large cluster spontaneously in lipid membranes [40]. However, an early EPR spectra measurement suggested that the majority of the Alm peptides were monomeric when they were incorporated into lipid membranes [41, 42]. Similar controversial results have been reported for spin labeled samples [43, 44]. Aside from this, different peptide aggregation states have been observed in other proteins such as the striated domain formation in supported lipid bilayers [45-48], parallel segregation at monolayer/water interface [49, 50], and spontaneous 2-D array formation of transmembrane (TM) proteins in purple membranes [51-53]. Our third mission of this thesis is to probe the aggregation state of Alm in lipid membranes.

## 1.2 Overview of alamethicin

Alm was discovered in the culture broth of the fungus *Trichoderma viride* in 1967 [54]. It is a member of the antimicrobial peptides (AMPs) which have a broad spectrum of antimicrobial activities against microorganisms through membrane disruption [55, 56] illustrated by the three models in Fig. 1.2. In the barrel-stave model which was first introduced to account for the single channel conductance of Alm [35], the amphipathic peptides form a barrel like bundle which acts as the channel wall. In the worm-hole (also called toroidal) model which was proposed to describe the maganin (a 23-residue AMP) induced pore [57, 58], each monolayer bends continuously at the channel region. The lipid headgroups stagger with the helical peptides forming the channel structure. In the carpet model, the peptides crowd together at the surface of the lipid bilayer leading to micellization [59].

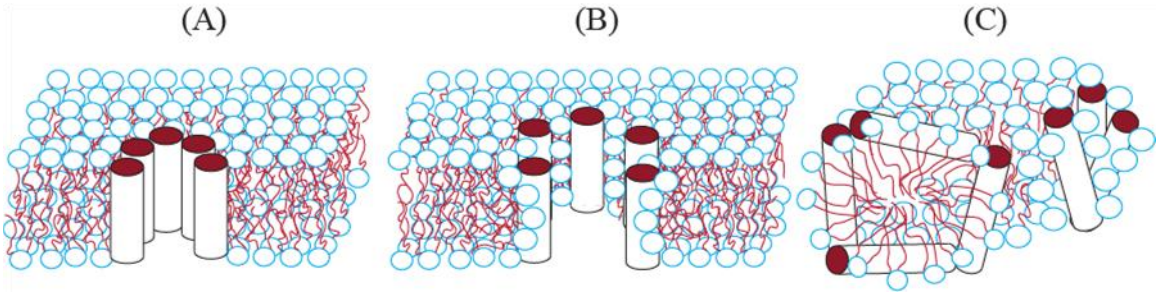


Figure 1.2: Three models illustrating the antimicrobial mechanisms. (A) Barrel-stave model, (B) Worm-hole (toroidal) model, (C) Carpet model.

The primary structure of Alm consists of 20 amino acids with a phenylalaninol (Phol)

at the C-terminal end and the N-terminal end being acetylated. Due to the lack of free α-amino groups, Alm was first though to be cyclic [54, 60]. The linear sequence was established later by performing NMR [61, 62] and by comparing the solid phase synthetic analogue to the naturally occurring compound [63, 64]. Thin layer chromatography (TLC) [65] revealed that there is more than one component in the naturally occurring Alm peptide even though sedimentation analysis suggested a reasonably homogeneous molecular weight [66]. The main components were later identified as F30 and F50 according to their mobility. The primary structure of F30 is acetyl-Aib-Pro-Aib-Ala-Aib-Ala-Gln-Aib-Val-Aib-Gly-Leu-Aib-Pro-Val-Aib-Aib-Glu-Gln-Phol. F50 is different from F30 by replacing $Glu^{18}$ with $Gln^{18}$ [67].

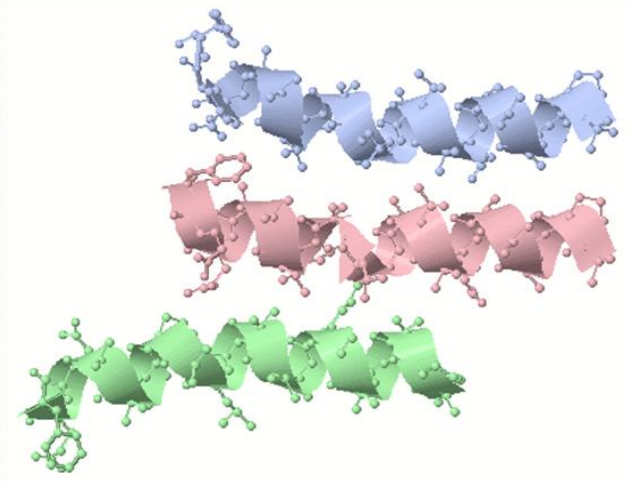

Figure 1.3: Crystal structures of three Alm molecules in one unit cell [32].

Structure: The high content of the α-amino-isobutyric acid (Aib), which is believed to act as helix former [68-71], decreases the flexibility of the peptide chain and produces a highly helical backbone. The crystal structure of Alm is shown in Fig 1.3 [32, 33]. The

main conformation of the peptide is an α-helix except some deviation in the C-terminal segment ($3_{10}$ helix). In order to accommodate the ring structure of $Pro^{14}$ into the α-helical backbone, the helix axis bends away from the ring direction. The resulting Alm conformation can be idealized as two α-helical segments (1-13 and 14-20) with an angle ~$20^{o}$ between the two axes. An interesting result is that the two residues $Gln^{7}$ and $Glu^{18}$ with polar side chains in addition to the solvent accessible carbonyl oxygen atoms of $Aib^{10}$ and $Gly^{11}$ lie on a strip which is believed to form the interior of the ion channel. The existence of the polar strip was later confirmed by a H-bonding measurement between the peptide resides and methanol using $^{13}C$ and $^{15}N$ NMR spectroscopy [72].

Other methods have also been applied to explore the peptide conformation in organic solvent and lipid membranes. The N-terminal segment was always found to be α-helical [34, 73-76], consistent with the crystal structure. However, the C-terminal segment is less conclusive [76, 77]. Both extended β-sheet [34, 73] and α-helix similar to the crystal structure [74] have been proposed.

Energetics of channel formation: The helical structure of Alm enables us to treat it as a macro-dipole with dipole moment ~40-80 Debye [78, 79]. It is mysterious then how the peptides can form a parallel bundle (open channel) with such strong repulsive dipole interactions present. One mechanism stabilizing the bundle structure is the H-bonds between the side chains of $Gln^{7}$ [32]. Indeed, when the side chain of $Gln^{7}$ is replaced with shorter ones, the channel becomes less stable and eventually the channel activity vanishes

when Ala replaces $Gln^{7}$ [80]. Other mechanisms contributing to channel stabilization have been revealed by MD simulations. Significant amounts of H-bonds between $Gln^{7}$ and the inner-bundle water molecules that stabilize the bundle structure have been reported [81]. Further examination of the energetics indicates that the electrostatic component of the bundle/water interaction is about 10 times larger than the helix/helix interaction. Peptide/lipid H-bonds between the side chains of $Glu^{18}$, $Gln^{19}$, $Phol^{20}$ and the phosphate, glyceryl, acyl oxygens of the neighboring lipid molecules have also been reported [82]. These H-bonds help to further stabilize the helix bundle by anchoring it to the lipid bilayer and slow down the peptide migration rate [83]. This also explains the preference for the insertion through the N-terminal segment and the asymmetrical current-voltage curve when Alm was added to one side of lipid membranes [9, 10, 84 ].

# Chapter 2

# Experimental and Monte Carlo simulations

## 2.1 Introduction

We used oriented multilayer samples in this thesis. They have the advantage over the 3-D powder averaged multilayer vesicles (MLV) in that the lateral organization (r direction) can be separated from the organization along the bilayer normal (z direction). Due to the length scale (~30Å) of the Alm peptide, the scattering intensity is concentrated at $q_z \leq 2\pi/30 = 0.2$ $Å^{-1}$. A small glancing angle α was applied to study the in-plane scattering by Alm bundles. A transmission scattering experiment was also employed in order to obtain the scattering at $q_z = 0$.

In this chapter, first we will discuss some experimental details of the optical setup, the background subtraction, the hydration level measurement (lamellar repeat spacing D) and the hydration level control for both the grazing incident and the transmission scattering experiment. After that, we will introduce Monte Carlo (MC) simulations that will be applied to estimate the positional correlation between the peptide bundles in oriented multilayer samples in later chapters.

## 2.2 Oriented multilayer sample preparation

DOPC (di18:1PC) and di22:1PC were purchased form Avanti Polar Lipids (Alabaster, AL). Alm was purchased from Sigma-Aldrich (Milwaukee, WI). This is a natural, purified 20 amino-acid peptide from *Trichoderma viride* consisting of 85% Alm I (F30) and 15% Alm II. These differ in the amino acid at the $6^{th}$ position: alanine in Alm I and aminoisobutyric acid (Aib) in Alm II.

4 mg of pure lipid was added to a chloroform:trifluoroethanol (TFE) solvent mixture (v:v 2:1 or 1:1) and to this was added the appropriate amount of Alm from a chloroform stock solution (1 mg/ml). Peptide to lipid mole ratios between 1:75 and 1:10 were studied. The mixture was plated onto the 1.5cm×3cm surface of a polished silicon wafer using the rock and roll procedure [85, 86]. The samples were allowed to dry for one day in a glove box with solvent-rich atmosphere and an additional day in a fume hood. They were then trimmed to a strip 0.5cm×3cm in the center of the silicon wafer and stored at $2^{o}$C in a dessicator prior to x-ray measurements.

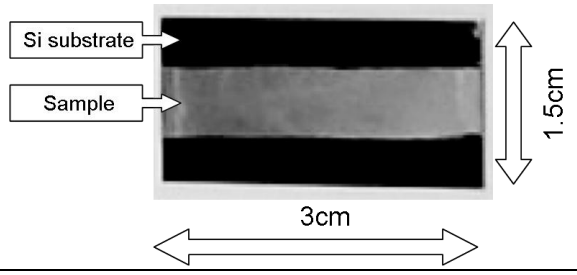


Figure 2.1: An example of the oriented sample (DPPC) deposited on a Si substrate (picture was taken from [86]).

## 2.3 Chamber

Resolution of the vapor pressure paradox, in which an oriented multilayer sample hydrated through the vapor has a reduced level of hydration compared to a sample immersed in excess water, required excellent temperature control [87]. Our thick-walled sample chamber enables us to hydrate the oriented sample to full hydration.

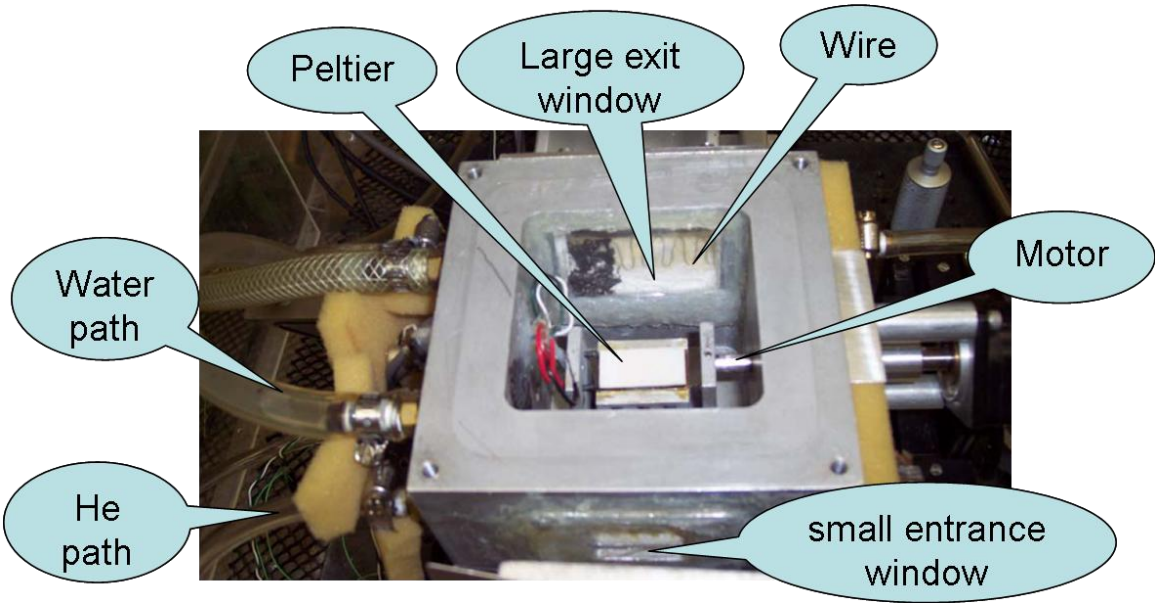


Figure 2.2: An image of the NIH chamber used to control the hydration level and the temperature of the oriented multilayer samples and manipulate the sample rotation and position. The walls are 1" thick and a 1" thick cover (not shown) screwed onto the top. Each window has mylar covering both the outer (visible for the entrance window) and inner (visible for the exit window) hole in the chamber wall.

The sample chamber we used for all of our experiments is the NIH chamber which was designed and built by Drs. Stephanie Tristram-Nagle, John Nagle, Horia Petrache

and Adrian Parsegian at the NIH in Bethesda [88]. Figure 2.2 shows a top view of the chamber. There are several essential design features which has been described in [88, 89]:

1. A Peltier stage which cools or heats the sample relative to the rest of the chamber in order to vary the sample hydration level. The Peltier is the same size as the silicon substrate used to deposit our sample. Dow Corning heatsink compound is used to achieve better thermal contact between the sample substrate and the Peltier stage.
2. A rotation motor which rotates the sample holder independently from the rest of the chamber in order to sample all relevant angles. The rotation motor enables us to rotate the sample continuously so we can look at all of the lamellar peaks. It is also important for background subtraction as will be discussed in the following sections.
3. Two tubes connected to a temperature-controlled water bath (Julabo) in order to control the temperature uniformly. The tubes bring the water into channels within thick walls of the aluminum chamber. In this way we were able to adjust the chamber temperature quickly and maintain uniform, constant temperature.
4. Two helium ports which allow for the replacement of air by helium to reduce background scattering.
5. Double mylar windows for both the entrance and the exit x-ray paths. Between each window, there is a heating wire. By running a small current though the wire, the heat generated was sufficient to prevent water condensation onto the inside mylar window due to the temperature gradient between the inside and outside of the chamber.
6. A water pool below the Peltier stage that provides the moisture to hydrate the sample within the chamber.

7. A piece of ashless filter paper which is glued to the top of the chamber with one end immersed in the water pool in order to increase water evaporation surfaces.

During the experiment, the chamber is attached to a large motorized stage which is capable of moving both laterally and vertically. In this way we can adjust the position of the sample that is x-rayed.

## 2.4 Optical setup

The grazing incident x-ray scattering experiments were carried out at the G-1 station (May 2008) at the Cornell High Energy Synchrotron Source (CHESS). Figure 2.3 shows the optical schematic of the G-1 beamline. In the G cave, a W:$B_4C$ multilayer (APS Optics Lab, Argonne, IL) was used to select the x-ray energy and suppress high order harmonics. The energy dispersion is ~1.1%. In our experiment, a wavelength $\lambda$ of 1.18Å was used. The upstream slits S1 and S2 are primarily used to define the beam size (~0.2 $\times$1 mm). The most downstream slit SG acts as guard slit to block parasitic scattering from slits, air, and other sources. The two ion chambers, I1 and I0, were used to measure the energy and the photon flux ($3\times10^{11}$/sec) of the incident x-ray.

For the transmission scattering experiment, we used a Rigaku RUH3R microfocus rotating anode at the power of 40kV×100mA (Woodlands, TX) equipped with a Xenocs FOX2D focusing collimation optic. The x-ray wavelength is 1.54 Å (Cu $K_\alpha$).

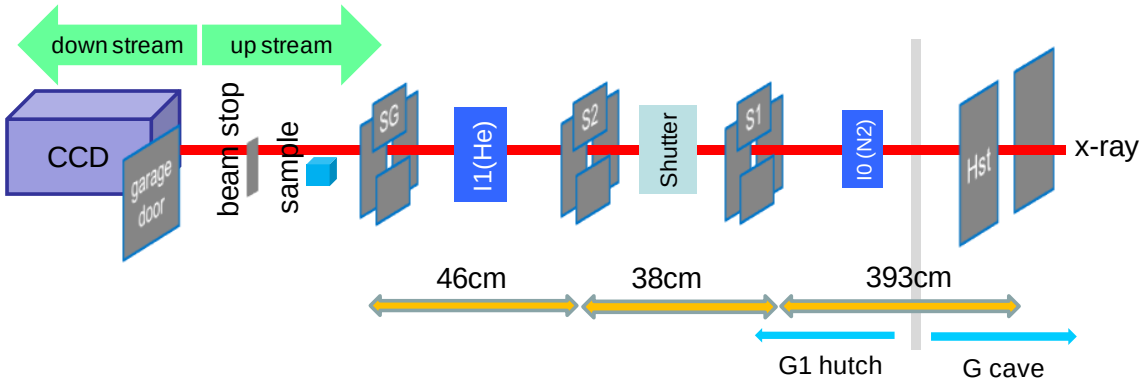


Figure 2.3: Optical schematic for G-1 beamline at CHESS (drawing adapted from Arthur Woll). Garage door is for the protection of the CCD; SG is the guard slit; I1 (He) and I0 (N2) are two ion chambers filled with He and N2 respectively; S2 and S1 are the two slits in the hutch; Hst is the horizontal slit in the cave.

## 2.5 CCD Detector

A CCD detector "Flicam" (Finger Lakes Instrumentation, Lima, NY) with 1024×1024 (0.070mm/pixel) size was used at CHESS and a Rigaku Mercury CCD detector with 1024×1024 (0.069mm/pixel) size was used at CMU to measure the scattered x-rays. Before processing any image, some standard corrections need to be done [90].

Zinger elimination: when using a CCD x-ray detector each image will have a random distribution of bright spots called zingers. Zingers come from cosmic rays, alpha particle decay and other radioactive events in the glass in the fiber optic taper. Although few pixels have zingers they tend to dominate averaging processes because of their great intensity. This is why they need to be identified and eliminated. One technique for doing so is statistical dezingering. Consider a pixel on N identical images. The average

intensity can be estimated by the median value and the deviation σ can then be predicted. The probability that an individual intensity value lies outside of ±5σ is less than one in a million unless a zinger occurs. Conversely, if a value contains a zinger it will easily lie outside this range. Excluding all such values should eliminate zingers without eliminating information about the x-ray image. In general, the number of zingers scales with the length of the exposure. For this reason, it is advantageous to add together many short scans as opposed to taking one long scan. Figure 2.4 shows two images before and after the statistical dezingering. As the process uses more than one image, the signal to noise ratio in Fig. 2.4B is improved compared to a single image in addition to the elimination of the bright spots in Fig. 2.4A

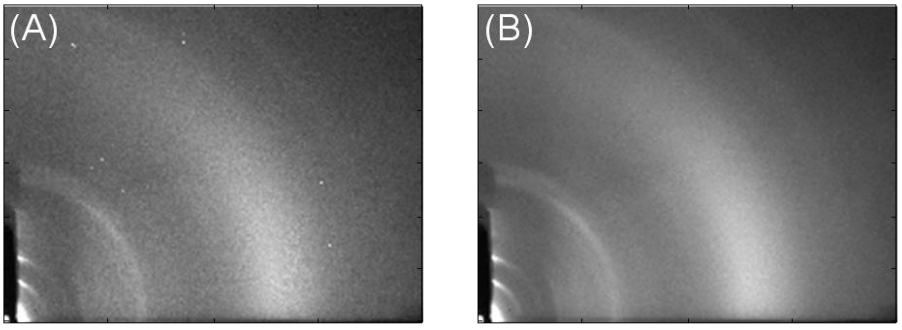


Figure 2.4: (A) An individual image with some zingers indicated by the bright spots. (B) Image after applying statistical dezingering.

Dark background: there is thermally generated charge in the CCD chip, which will give rise to counts even when there is no incoming radiation. For this reason, a dark

background image, which is taken with the incoming x-ray completely blocked and has the same exposure time, is subtracted out from each scattering image.

Distortion and intensity corrections: a geometrical distortion correction due to the fact that the CCD array is not a perfect grid and a sensitivity correction due to the different response of each pixel to the same count of the incoming x-ray are also needed. These corrections are performed aromatically by the Spec software (CHESS) and the Crystal Clear software (CMU).

## 2.6 Grazing incident scattering experiment

Although we used a small incident glancing angle ($\alpha=0.2^o$), our grazing incident scattering experiment is not the same as the surface sensitive grazing incident scattering experiment [36] because our glancing angle is larger than the critical angle of the Si substrate ($\alpha=0.17^o$). The main purpose of this experimental setup is to explore the scattering near $q_z=0$. Depending on the regime in the reciprocal space investigated, the setup is refined to two subcategories, low angle scattering (LAXS) and wide angle scattering (WAXS).

### 2.6.1 Grazing incident glancing angle

There are three main criteria for the choice of the grazing incident glancing angle α. (1) The first is that the angle should be as small as possible. When the angle is smaller, the scattered x-rays are blocked less by the sample and the silicon substrate. This is

shown by the height of the black horizontal strips in Fig. 2.5 where we looked at three different incident glancing angles from $0.05^o$ to $0.2^o$. (2) The second criteria is that the scattering pattern should be as simple as possible. As indicated by the red circle regions in Fig. 2.5, when $\alpha$ is smaller than the critical angle of the silicon substrate ($\alpha=0.17^o$) (http://www-cxro.lbl.gov/), each lamellar peak has a weaker "ghost" peak that occurs at slightly higher angle. Figure 2.6 illustrates the mechanism of the "ghost" peak which is due to the total external reflection by the silicon substrate. (3) The third criteria is that the scattering intensity should be as strong as possible for the same exposure. From Fig.2.5 we see that when $\alpha$ is the smallest, $0.05^o$, the scattering is also the weakest. This is mainly due to the increased absorption by the lipid sample. An interesting observation in Fig. 2.5C is that even when the glancing angle is smaller than the critical angle of the lipid bilayer ($0.11^o$), the lipid surface does not give total reflection due to the undulation of the sample surface. Based on the above criteria, we used $\alpha=0.2^o$ for all of the grazing incident glancing angle experiments except the wide angle x-ray scattering experiments taken at CMU where a slightly larger glancing angle ($0.5^o$) was used in order to increase the signal to noise ratio.

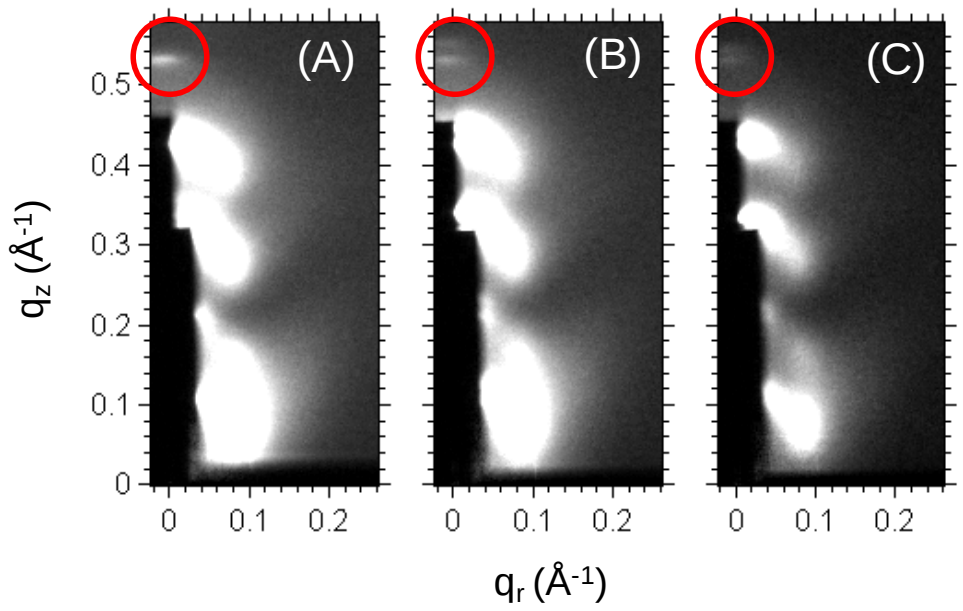


Figure 2.5: X-ray scattering images at three different incident glancing angle α (A) 0.2°, (B) 0.1°, (C) 0.05°. The color scale and the time of exposure are the same for all three. The red circles indicate the position of the 5th lamellar peak. The vertical strip is a piece of molybdenum used to attenuate the direct beam and the lower order lamellar peaks.

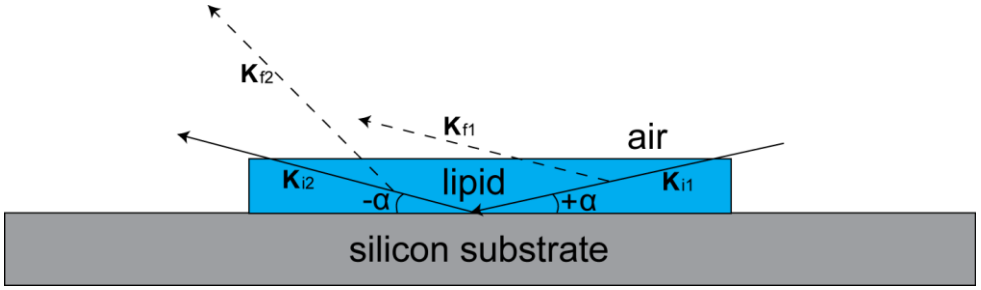


Figure 2.6: Illustration showing the splitting of lamellar peaks when the incident glancing angle α is less than the critical angle of the silicon substrate (drawing adapted from [89]). The pair of $\mathbf{K}_{i1}$ and $\mathbf{K}_{f1}$ are the normal wave vectors. The total internal reflection $\mathbf{K}_{i2}$ gives rise to a second scattered wave vector $\mathbf{K}_{f2}$.

## 2.6.2 Background subtraction

The CCD does not only record the scattering from our oriented samples, but also from other scattering sources, including the ~2mm air gap between the x-ray flightpath and the chamber, the mylar windows of the chamber, and gas molecules in the chamber are all capable of scattering the incoming x-ray. The idea of subtracting out the scattering other than from the sample is to set up a pair of identical paths for the incoming x-ray except that one has sample and the other does not. Figure 2.7 shows how this goal was achieved [89, 91]. By comparing Fig. 2.7A and Fig. 2.7C we see that the only difference of the two paths for the data collection and the background collection setup is the path along the silicon substrate, which is negligible as the chamber is filled with helium which has small scattering compared to air. For the rest of the paths, both downstream and upstream relative to the sample are the same. In this way the extra scattering can be almost completely subtracted.

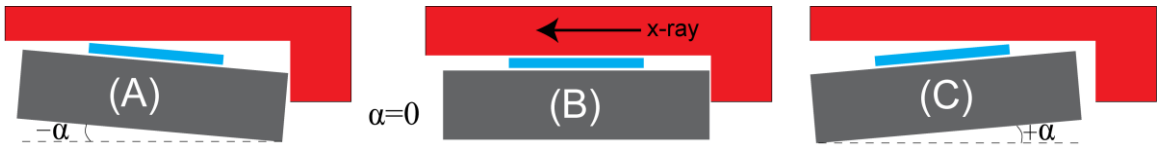


Figure 2.7: Schematic for grazing incident x-ray scattering experiment. (A) Sample data collection and (C) Background data collection. The red region represents the incident x-ray; the blue region represents the sample; the gray region represents the sample holder.

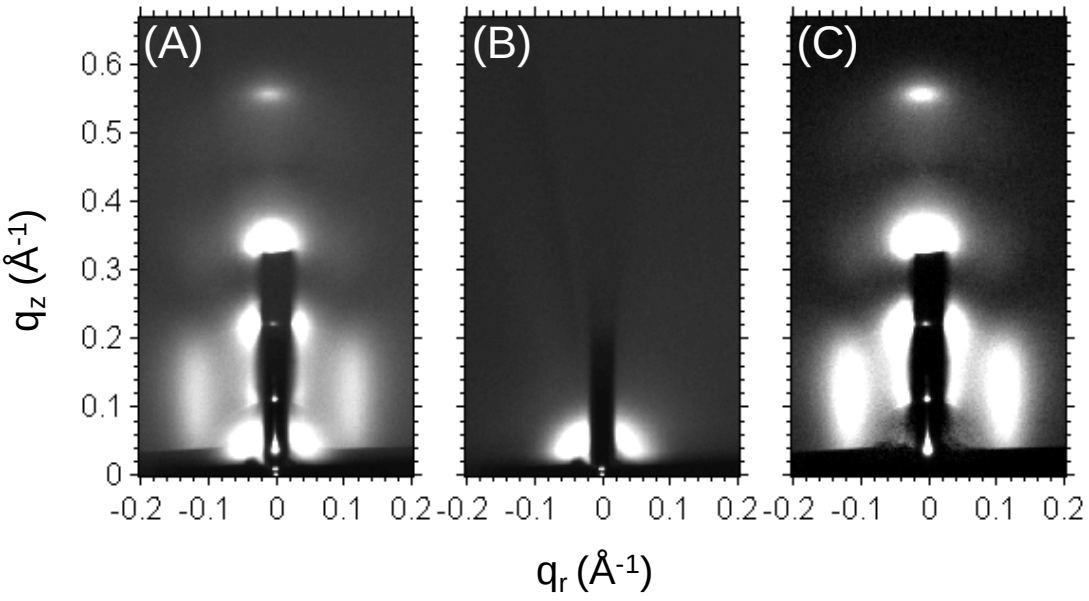


Figure 2.8: Background subtraction for low angle scattering image ($\alpha$=0.2$^o$). (A) Sample scattering, (B) Background scattering, (C) Sample scattering with background scattering subtracted (different color scale).

An example of the background subtraction in the low angle regime is shown in Fig. 2.8. In Fig. 2.7A, the bright spot at $q_z$=0 is the direct beam after attenuation by a 220μm molybdenum (Mo) beam attenuator. The finger shaped black strip is a 100 μm Mo attenuator used to attenuate the first two lamellar peaks shown as bright spots located at $q_z$~0.11 and 0.22 Å$^{-1}$. The thickness of the attenuators was chosen so that there is enough transmitted scattering for position determination of the direct beam and the lamellar peaks which are used for lamellar repeat spacing D measurement. Figure 2.8B shows the background image from which we see that the majority of the background is the splash located near the direct beam. The subtracted image is shown in Fig. 2.8C which shows that the direct beam and the splash are almost completely subtracted out. The remaining

are the lamellar peaks behind the attenuator and the diffuse scattering around the lamellar peaks due to thermal fluctuations and disorder in addition to the two rod like peaks which will be discussed in the later chapters. The small spot directly above the beam that is present in both the sample and the background images is caused by the tail of the beam or by the splash that hits the 100μm Mo. The streak located at $0.03<q_z<0.05$ $Å^{-1}$ (Fig. 2.8A) has been observed in all of our sample images. The source of this streak is not obvious. It might be due to the tail region of the total reflection by the sample or the silicon surface.

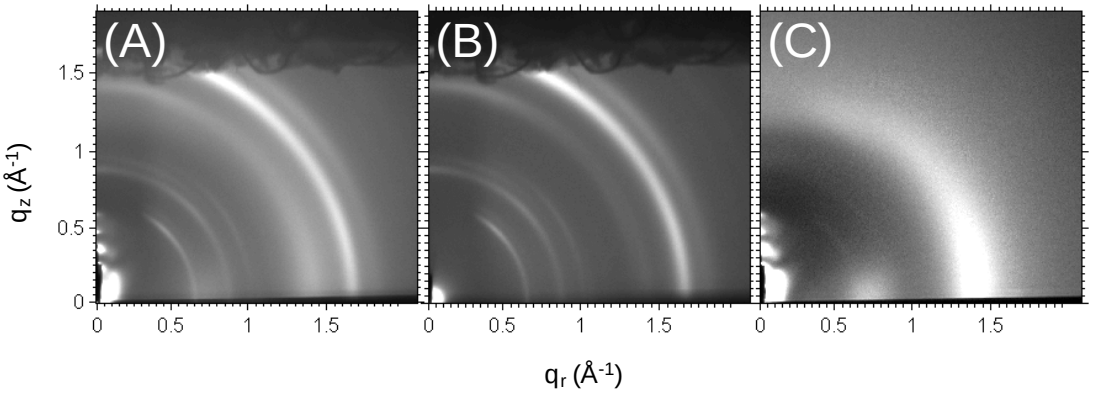


Figure 2.9: Background subtraction for wide angle scattering image. (A) Sample scattering, (B) Background scattering, (C) Sample scattering with background scattering subtracted (different color scale).

A similar background subtraction is carried out for the scattering in the wide angle regime shown in Fig. 2.9. From the figure we see that the main background consists of arcs from the mylar windows and the dark fuzzy region at $q_z>1.5$ $Å^{-1}$ due to insulation the exit window. After subtraction, these vanish and the resulting image in (C) was then

analyzed.

### 2.6.3 D spacing measurement

For ideal oriented multilayer samples, the nth lamellar peak can only be observed when the x-ray incident angle θ satisfies the Bragg equation $2D\sin(\theta) = n\lambda$ [92], where D is the lamellar repeat spacing and λ is the x-ray wave length. For this reason we need to rotate the sample in order to see all of the lamellar peaks. In practice the sample rotation is achieved by controlling the motor attached to the sample holder in Fig. 2.1. The rotation angle range was typically from -3 to $7^o$ with frequency about 20 Hz. The reason for the negative angle is to compensate for the possibility that there is some dead time between each period during which the motor is static. The dead time will make the exposure duration for each lamellar peak not uniform. This will cause trouble if the peak intensity is used such as the classical Fourier transform of the lamellar peaks to obtain the electron density distribution of the lipid bilayer.

There is one parameter we need to know, θ, before we can do any calculation of the D spacing based on the Bragg equation. The scattering angle θ is related to the sample to CCD distance S and the peak position relative to the beam position in the CCD frame. The two positions are known directly from the CCD image. For the S, we need to rely on external calibration. This is done by using a standard, silver behenate, which has a fixed repeat spacing D (Ag Behenate)=56.38Å [93]. The standard is prepared in the same way, cut into the same shape, and placed at the same position as the sample. In this way, the

calibrated S is also the S for the sample. Figure 2.10 shows a scattering image from the partially oriented standard. The ring shaped scattering is typical for powder samples. From the image, the peak positions of the Bragg peaks relative to the beam position are obtained, $h_n$ (n=4, 5, 6, 7). Then $\sin(\theta_n)=\sin(1/2\text{atan}(h_nP/S))$, where P is the pixel size of the CCD. Because all of the peaks follow the Bragg equation, we have:

$$\begin{cases} 2D\sin[\frac{1}{2}\text{atan}(h_4P/S)] = 4\lambda \\ \bullet \\ \bullet \\ 2D\sin[\frac{1}{2}\text{atan}(h_7P/S)] = 7\lambda \end{cases} \tag{2.1}$$

where P is the pixel size of the CCD. There are 4 equations and only one unknown parameter S. By solving equation (2.1) in a non-linear least square fashion, the best estimated sample to CCD distance S was obtained.

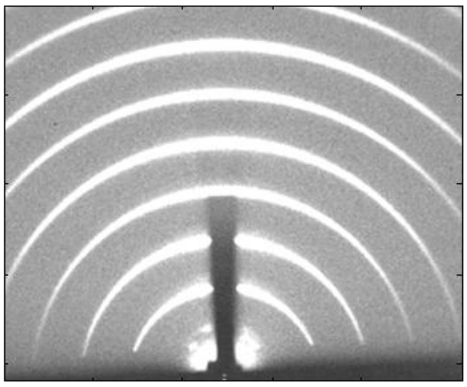

Figure 2.10: Scattering image for a partially oriented sample of silver behenate.

By placing the sample in the same position as the standard, Fig. 2.11 shows a typical scattering image for D spacing measurement. Because the first few lamellar peaks are

usually very strong, a finger shaped Mo attenuator is used to prevent the CCD from saturation. When the sample hydration level is low, there are usually more than three lamellar peaks which make the D spacing determination relatively easy. When the sample gets more hydrated, the higher order lamellar peaks become overwhelmed by the diffuse scattering due to the increased fluctuations. In this case, only the first two lamellar peaks and the beam position are available for the D spacing measurement.

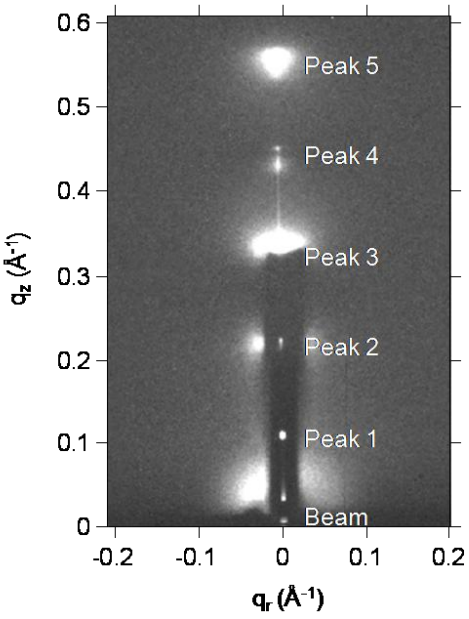


Figure 2.11: Image for D spacing measurement. The sample is DOPC at D~56.0Å.

Once the lamellar peak positions are obtained, the $\sin(\theta_n)$ term in the Bragg equation is calculated for each peak n with the known sample to CCD distance S from the standard measurement. The same set of equations as in equation (2.1) is then used to estimate the D spacing except that this time it can be done in a least square fashion.

### 2.6.4 Hydration level Control

It is important for us to be able to control the sample hydration level of the oriented multilayer samples. The first reason is that we want to study how the in-plane scattering from embedded peptides changes as a function of the amount of water molecules between the neighboring bilayers. The second reason is that when the sample is near full hydration, the correlation between the embedded peptides in the neighboring bilayers is negligible which simplifies the modeling process needed for the data fitting as will be shown later.

Hydration through the vapor was facilitated with the help of a Peltier cooler under the sample (Fig. 2.2) to lower temperature of the sample relative to the water vapor ($<0.1^{o}$C), thereby condensing water onto the sample. In practice, we found that a piece of filter paper with one end attached to the top of the chamber cover and the other end immersed into water pool in the chamber helps greatly to hydrate the sample as in [88]. The filter paper increases the evaporation rate of the water molecules into the inner-chamber and consequently condensed onto the sample.

## 2.7 Transmission scattering experiment

One drawback of the grazing incident scattering experiment is that the scattering near the equator ($q_z$=0) is blocked by the silicon substrate. A closely related issue is that the absorption of the scattering by the sample for $q_z$ near 0 is stronger than for larger $q_z$. One solution to these two problems is to apply a transmission scattering setup as

illustrated in Fig. 2.12 similar to [85, 94]. In this setup, the sample is maintained at a fairly large fixed angle α (30 and 45$^{o}$ were used). As the substrate is at the upstream position relative to the sample, no scattering was blocked by the substrate, although the substrate obviously attenuates the beam. For the absorption problem, the absorption length of the sample is around 1.0mm (http://www-cxro.lbl.gov/) for the wave length we used (Cu $K_{\alpha}$) is much larger than the path of the x-ray, ~10μm, so we can neglect the absorption effect for all of the q values we are interested in. In the experiment two aluminum holders constructed by Antony Vydrin and myself were used. The holders were placed on top of a rotation motor so different incident angles of the sample relative to the incoming beam can be achieved by adjusting the angle of the rotation motor.

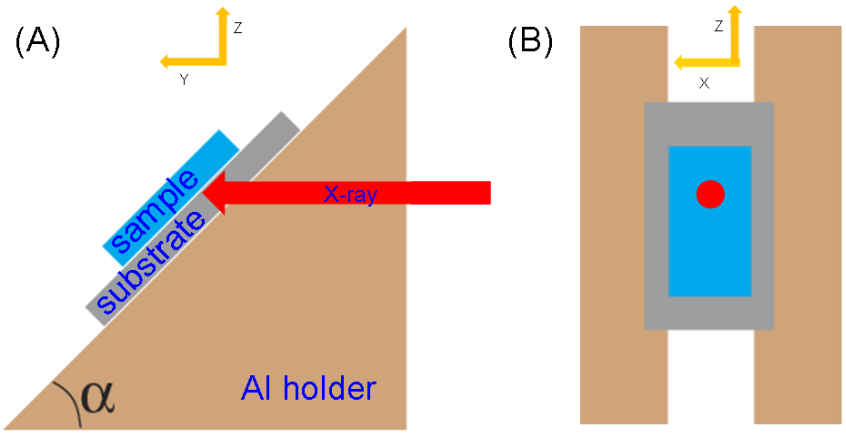


Figure 2.12: Schematic of transmission scattering experiment. (A) Side view. (B) Front view.

Even though the transmission scattering setup has some advantages over the grazing incident scattering setup as discussed in the previous paragraph, one challenge is how to prepare the sample without breaking a fragile 35μm thick silicon substrate which is used

for the transmission geometry. What we did is to deposit the peptide/lipid mixture with proper ratio dissolved in chloroform on to the thin silicon substrate and let the solvent evaporate without much rock and roll. For this reason, the obtained sample has poorer mosaicity.

### 2.7.1 Background subtraction

For the background subtraction, the plus and minus rotating angle method for the grazing incident scattering experiment can not be applied anymore because the rotating angle in this case is too large. What we did is to utilize the fact we mentioned earlier that the absorption of the incoming x-ray by the sample is negligible. Then we can take a separate scan with a pure substrate instead of the sample/substrate and subtract it from the sample image. An example of the subtraction is shown in Fig.2.13.

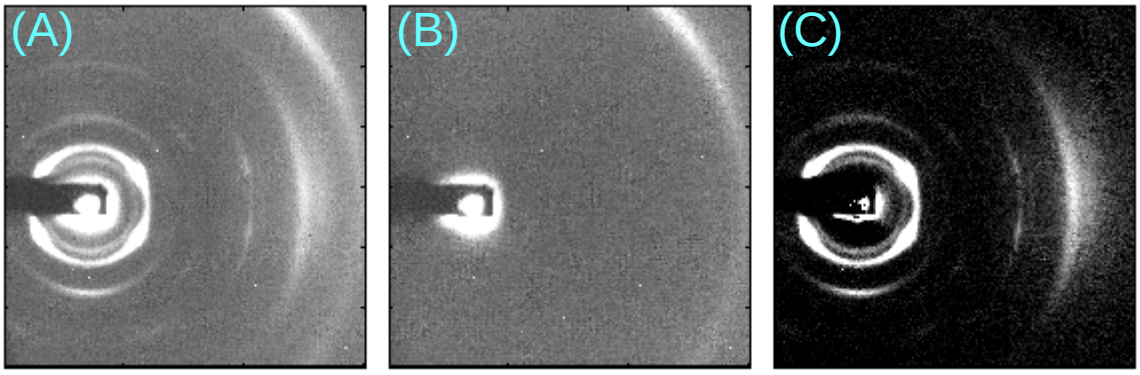


Figure 2.13: Transmission scattering images for (A) Scattering from sample, (B) Scattering from background, (C) Background subtracted sample image.

## 2.7.2 D spacing measurement

In order to track the sample hydration level, we need to measure the lamellar repeating spacing D. Following the same procedure as in the grazing incident scattering experiment, we first position the sample horizontally followed by a continuous rotation from -3 to 7$^{o}$. An example of the scattering image for D spacing measurement is shown in Fig. 2.14. Three lamellar peaks above the direct beam are observable. The weak peak below the beam position is the mirror image of peak 1. It is observable due to the semitransparent substrate. Because the rotating anode was used for the transmission scattering experiment, no attenuator is necessary for the first two lamellar peaks.

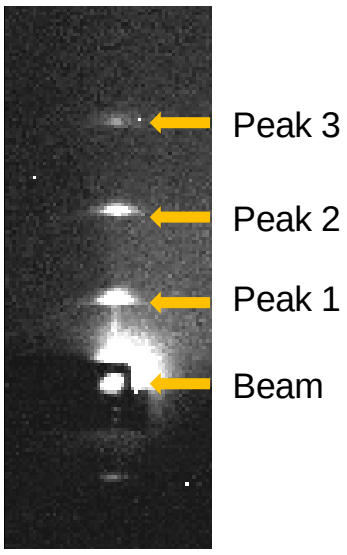


Figure 2.14: An example of the lamellar repeat spacing D measurement for transmission scattering experiment. The sample is Alm:DOPC 1:10 with D= 48Å.

## 2.7.3 Hydration level control

Even though the NIH chamber is quite good at hydrating oriented multilayer samples,

the problem here is how to substantially dehydrate the Alm/lipid sample because the crystalline scattering from Alm peptides that we are interested in is only observable at extremely dehydrated condition [39, 94]. To achieve this, we lower the temperature of the chamber suddenly from $25^{o}$ to $18^{o}$ and run helium constantly through the inner chamber (very slow rate). Because there is a time delay during the cooling process between the air (cools faster) in the chamber and the sample (cools more slowly), the humidity in the sample is reduced. This process is very similar to the one where we heat the sample a little bit relative to the air in order to dehydrate the sample a little bit. The difference is that the heating process can only dehydrate the sample by a small amount because the peltier heater/cooler has limited temperature adjustability.

## 2.8 Monte Carlo simulations

Monte Carlo (MC) simulations are a class of computational algorithms that rely on repeated random sampling. It can be used when it is not feasible or impossible to compute an exact result with a deterministic algorithm. To begin with, let us first show how to approximate $\pi$ by using MC simulations. The steps are as following:

1. Draw a square with length a for each side on the ground and then inscribe a circle centered at the center of the square with diameter a.
2. Uniformly scatter points throughout the square.
3. Count the number of points in the circle and the total number of points in the square. The ratio will approximate $\pi/4$ when there is enough sampling.

In later chapters, we calculate the positional correlation between disks in a 2-D space. For simplicity we assume that the disks follow the hard disk condition where no pairs of disks can get closer than 2R [25]. Aside from that, there can exist other types of interaction potential V(r) between each pair of disks (soft disk). The MC simulation follows the Metropolis algorithm [95].

1. Generate a random point $(x_1, y_1)$ within a square with side length a.
2. Generate a second point $(x_2,y_2)$ within the square. If the distances from the second point $(x_2, y_2)$ and its mirror images $((x_2 \pm a, y_2), (x_2, y_2 \pm a))$, $((x_2 \pm a, y_2 \pm a), (x_2 \pm a, y_2 \pm a))$ are all further away from the first point than 2R, the second point is accepted, otherwise regenerate the second point until the conditions are satisfied.
3. Generate a third point $(x_3, y_3)$ within the square. Calculate the distances from the third point and its mirror images to the first and the second points. If all of the distances are larger than 2R, the third point is accepted, otherwise regenerate the third point until the conditions are satisfied.
4. Apply the same procedure to generate the $(x_4, y_4)$, $(x_5, y_5)$, ..., $(x_{N-1}, y_{N-1})$ points.
5. Generate an Nth point $(x_N, y_N)$ within the square. Calculate the distances from the Nth point and its mirror images to the rest of the points (the first to the (N-1)th points). If all of the distances are larger than 2R, the Nth point is accepted, otherwise regenerate the Nth point until the conditions are satisfied.
6. Keep a record of the N points generated from step 1 to 5. It is the first state of the N disks satisfying the hard disk condition.
7. Calculate the interaction potential V(r) between each pair of the disks and sum them

as E1 (a cut off range can also be set beyond which there is no interaction).

8. The first disk was allowed to move by a step s in a random direction. If it moves out of the box from one side, it will move in from the opposite side to satisfy the periodic boundary condition. If any pair distance between the first disk and the rest of the N-1 disks becomes smaller than 2R, the disk moves back to its original position.
9. Calculate the new interaction potential between each pair and sum them as E2.
10. Generate a uniformly distributed random number r between 0 and 1.
11. Compare the Boltzmann factor $p=\exp[-(E2-E1)/k_BT]$ with r. If p>r, the new position of the first disk is accepted, otherwise the disk moves back to its original position.
12. Repeat the steps from 7-11 for the rest of the N-1 disks (it is called one iteration).
13. Calculate the ratio of the successful moves in the preceding iteration from step 7-12. If the ratio is too large (>80%), increase the step distance s, otherwise if the ratio is too small (<50%), decrease s.
14. Record the new position of the N disks as a new state.
15. Repeat the steps from 7-13 for M times ($>10^5$).

The consideration of the mirror images in steps 3-5 is for the periodic boundary condition. The number of disks N is decided through the area packing fraction (the area occupied by the disks divided by the total area) $\eta = N\pi R^2 / a^2$ which is a known physical parameter. To check the equilibrium of the simulation, the radial pair distribution function n(r) was calculated. After n(r) becomes stable, the averaged state of the

simulation approximates the distribution of the N disks which follow the hard disk condition in addition to the pair interaction potential V(r).

## 2.9 Conclusions

In this chapter we have shown some of the experimental details including the design of the NIH chamber which is capable of hydrating oriented samples to near full hydration, the optical setup for the x-ray scattering experiment, the CCD image processing, the background subtraction, the sample to CCD distance calibration, the D spacing measurement, and the sample hydration level control. We also described how to model the distribution of the disks in a 2-D space that follow the hard disk condition in addition to some pair interaction potential V(r) by using MC simulations.

# Chapter 3

# Hydration effect on peptide induced scattering

## 3.1 Introduction

In our oriented multilayer samples, the peptide inclusions are distributed in each lipid bilayer which is separated from the neighboring bilayer by a water layer with thickness $D_W$. The interactions between the peptide inclusions in different bilayers, including the van der Waals and the electrostatic interactions are dependent on the water layer thickness $D_W$. When $D_W$ is large enough, these interactions are negligible due to their rapidly decreasing nature as a function of the distance between the inclusions. The large fluctuations of each lipid bilayer also helps to wipe out correlations between the inclusions in different bilayers. When the sample is partially dehydrated, $D_W$ becomes smaller and the interactions become larger. The overall effect of the dehydration will therefore result in enhanced correlation between the peptide inclusions in different bilayers and these correlations can be observed through the shape and the position of the x-ray scattering peaks. In this chapter, first we will show some experimental data of the in-plane scattering by Alm bundles as a function of hydration level. Then we will present a mathematical model following [96] that can demonstrate the observed trend.

## 3.2 Scattering feature due to Alm incorporation

Figure 3.1 shows the grazing incident low angle x-ray scattering images for pure DOPC (panel A) and Alm:DOPC 1:10 (panel B) oriented multilayer samples at similar hydration levels. By comparing the two sets of data we see that the addition of the peptide causes the appearance of the two side peaks located at $q_r \sim \pm 0.11$ Å$^{-1}$. Similar side peaks have been observed by neutron scattering with $D_2O$ [22]. The authors attributed their peaks to water columns formed in the middle of Alm bundles. This is consistent with our observation of the side peaks at similar position since the scattering source in our experiment is the peptide itself which is known to aggregate and form ion channels. Alm peptide induced side peaks have also been observed by another group using x-ray scattering [25]. However, because their sample was at a much lower hydration level, their obtained side peaks were more like crystal peaks. Our observed side peaks are Bragg rod shaped, which are related to the 2-D distribution of the scattering entities [36]. The Bragg rod shaped peaks have been observed for another channel forming peptide, gramicidin using x-ray scattering [96].

Aside form the side peaks, we also notice that the addition of the Alm peptide weakens the diffuse scattering in lobe 2 and lobe 3. The analysis of the diffuse scattering reveals the perturbation of the mechanical and structural properties of the lipid bilayers under the influence of the peptide incorporation and this has been published recently [97]. In this thesis we are only going to focus on the two side peaks caused by the Alm bundle itself.

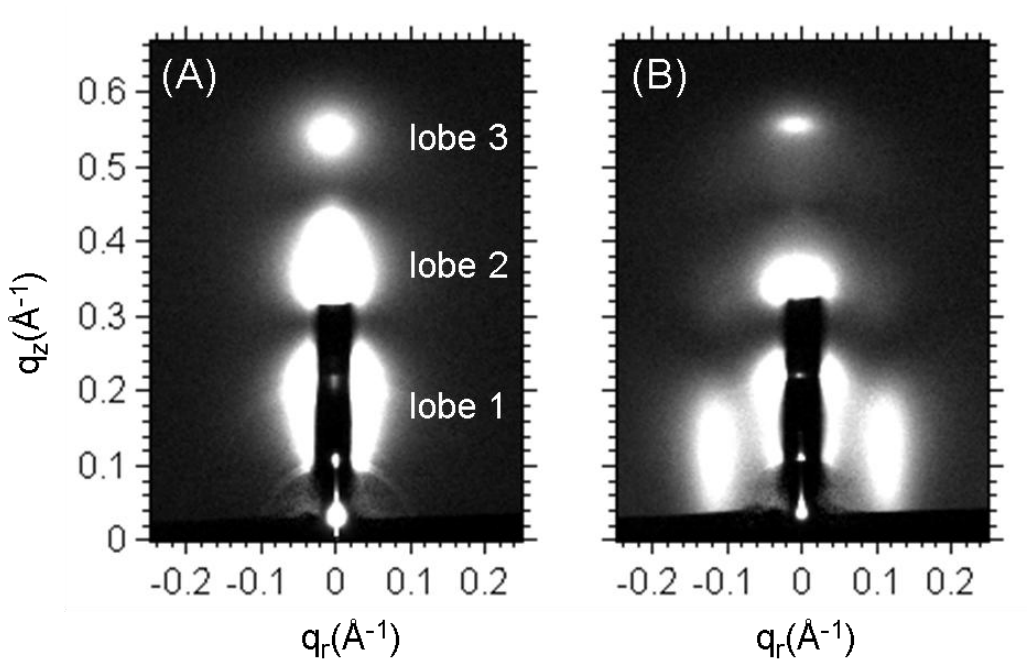


Figure 3.1: Background subtracted grazing incident x-ray scattering ($\alpha$=0.2$^o$) images for (A) DOPC and (B) Alm:DOPC 1:10 at similar hydration levels. (A) The three lobes are due to thermal fluctuations of the lipid bilayers. (B) There are two extra side peaks at $q_r \sim \pm 0.11$Å$^{-1}$ which are not present in (A). The black strip at the bottom and the finger shaped strip in the middle of each panel are where a molybdenum beam attenuator is used to attenuate the direct beam and the first and the second order Bragg peaks which are shown as white spots in the finger shaped region.

## 3.3 Hydration effect on Alm:DOPC 1:10

Figure 3.2 shows the scattering images for Alm:DOPC 1:10 at three different lamellar repeat spacing D values. From the figure we see that when D is 53.3Å (Fig. 3.2A), each side peak is composed of two peaks located at approximately $q_z \sim 0.07$ Å$^{-1}$ (peak 1) and 0.17 Å$^{-1}$ (peak 2) and there is some diffuse scattering between them. When

D increases to 54.4 Å (Fig. 3.2B), peak 2 becomes stronger, as does the diffuse scattering between them. When D increases to 56.3 Å (Fig. 3.2C), there is no discernible peak 1 or peak 2 and the overall side peaks become continuous along the $q_z$ direction.

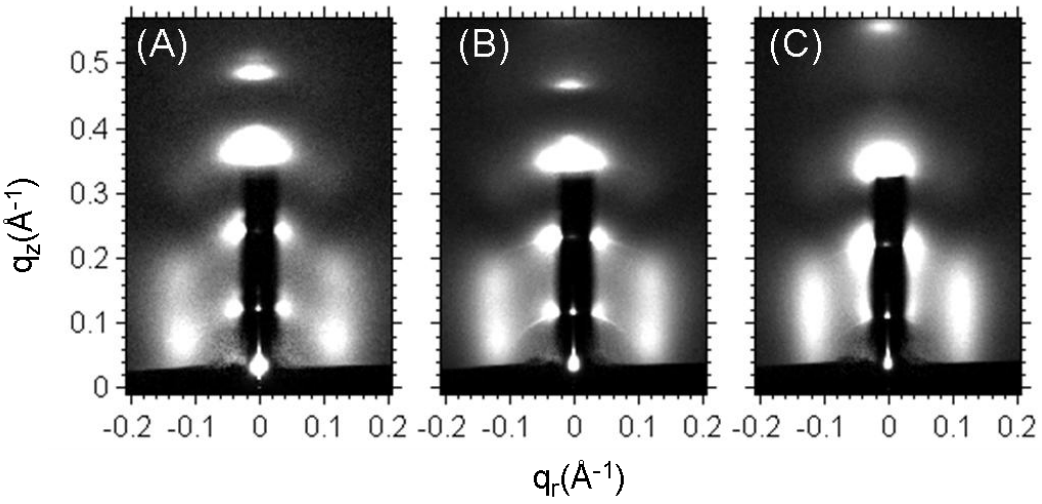


Figure 3.2: Background subtracted grazing incident x-ray scattering ($\alpha$=0.2$^o$) images for Alm:DOPC 1:10 at three different hydration levels. (A) D=53.3 Å, (B) D=54.4 Å, and (C) D=56.3 Å.

Sometimes the color scale can be misleading, so we plotted the $q_z$ dependence of the intensity along the center of the side peak in Fig. 3.3. When D=53.3 Å, there are two broad peaks (peak 1 and peak 2 in Fig. 3.2A) along the $q_z$ direction indicated by the two arrows. As D increases to 56.3 Å, the broad peaks coalesce and the curve at $q_z$ <0.2 $Å^{-1}$ becomes very smooth.

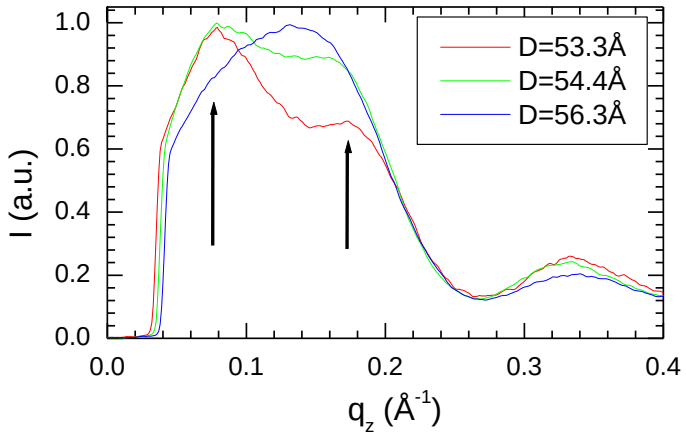


Figure 3.3: Side peak intensity along the $q_z$ direction centered at $q_r$ = 0.11 Å$^{-1}$ for the three images in Fig. 3.2. The intensity is averaged over 0.03 Å$^{-1}$ in the $q_r$ direction. The two arrows indicate the positions of peak 1 and peak 2 for the curve with D=53.3 Å.

## 3.4 Hydration effect on Alm:diC22:1PC 1:10

Another lipid we looked at concerning the hydration effect on Alm bundle structure is diC22:1PC, which has a bilayer about 7.6 Å thicker than the DOPC lipid bilayer [98]. The grazing incident low angle x-ray scattering images at six different D values for Alm:diC22:1PC 1:10 are shown in Fig. 3.4. When D is 58.5 Å (Fig. 3.4A), there is a broad peak similar to peak 1 in Fig. 3.2A in addition to three satellite peaks at larger $q_z$ values as identified by the intensity versus $q_z$ plot in Fig. 3.5. By comparing them with the lamellar diffraction peaks, the satellite peaks can be indexed approximately as 1/2, 3/2, 5/2 and 7/2 except that they are off the specular axis. These peaks are due to the correlated 3-D distribution of the scattering entities in lipid bilayers. As the hydration level increases, the satellite peaks become elongated along the $q_z$ direction.

The trend with hydration level of the side peaks is very similar to that of Alm:DOPC 1:10 in Fig. 3.3. Meanwhile there is an additional feature due to the hydration effect shown in Fig. 3.5. As the D spacing increases from 63.4 to 70.3 Å, the normalized intensity within the $q_z$ range of 0.12-0.22 $Å^{-1}$ does not change at all while the intensity at $q_z$<0.11 $Å^{-1}$ decreases continuously. The latter is mainly due to the absorption by the increased water layer thickness between lipid bilayers. This means once the D spacing reaches 63.4 Å for Alm:diC22:1PC 1:10 where the satellite peaks in the intensity versus $q_z$ plot disappear, the 3-D correlation of the scattering entities is no longer obvious. Following the same rule, we can conclude that there is little or no 3-D correlation between the scattering entities in Alm:DOPC 1:10 when D is 56.3 Å based on Fig. 3.3. The absence of the correlation along the bilayer normal simplifies the model we need to construct when we are trying to fit the side peaks as will be shown in the later chapters. One noticeable difference between the two lipids based on Fig. 3.2 and Fig. 3.4 is that even though the trend of the side peaks as a function of the hydration level is similar, the $q_r$ position of the side peaks is different. This is indicative of a different characteristic distance between the scattering entities in these two lipids.

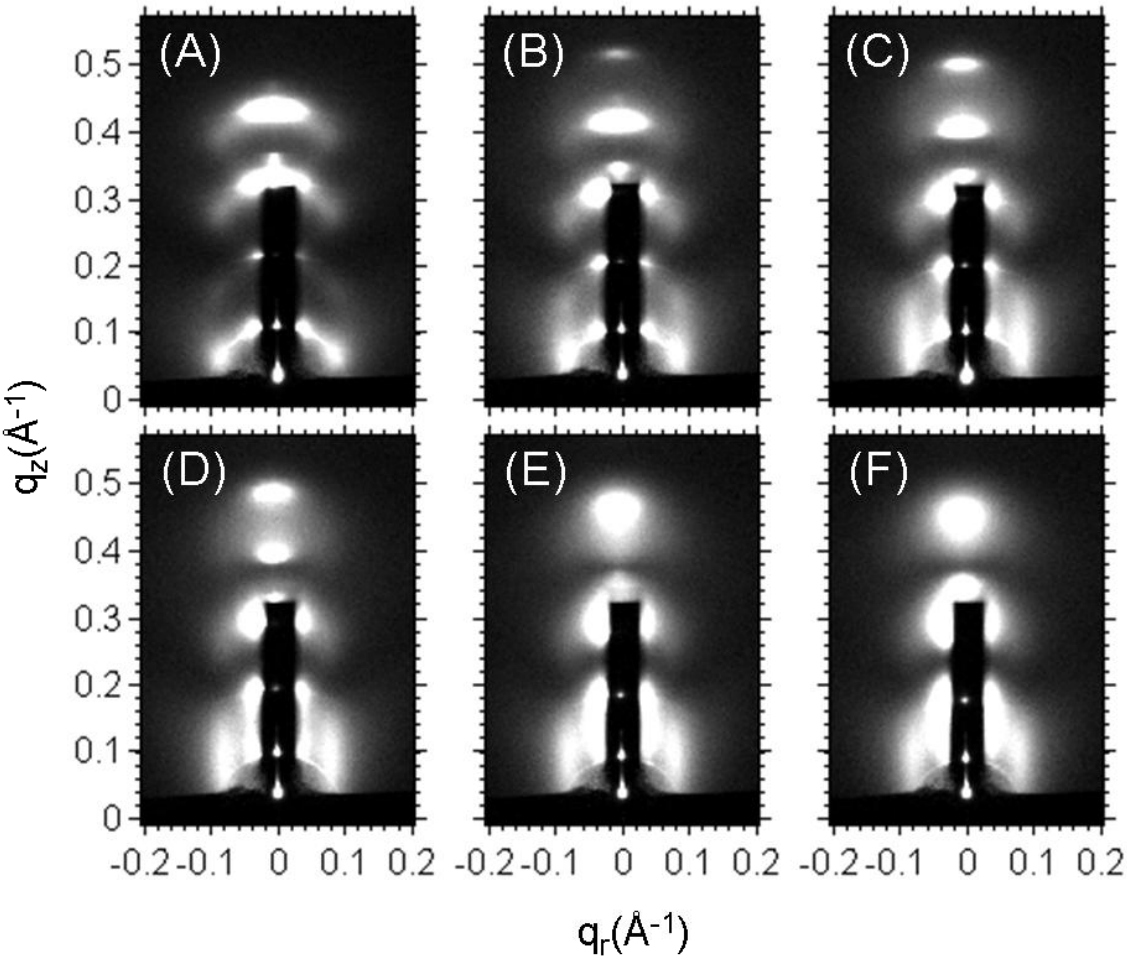


Figure 3.4: Background subtracted grazing incident low angle x-ray scattering ($\alpha=0.2^o$) images for Alm:diC22:1PC 1:10 at six different hydration levels. (A) D=58.5 Å, (B) D=61.3 Å, (C) D=63.4 Å, (D) D=64.1 Å, (E) D=68.3 Å, and (F) D=70.3 Å. The trend of the side peaks as a function of hydration level is very similar to Alm:DOPC 1:10 except that the $q_r$ position of the side peaks is smaller, ~0.08$Å^{-1}$.

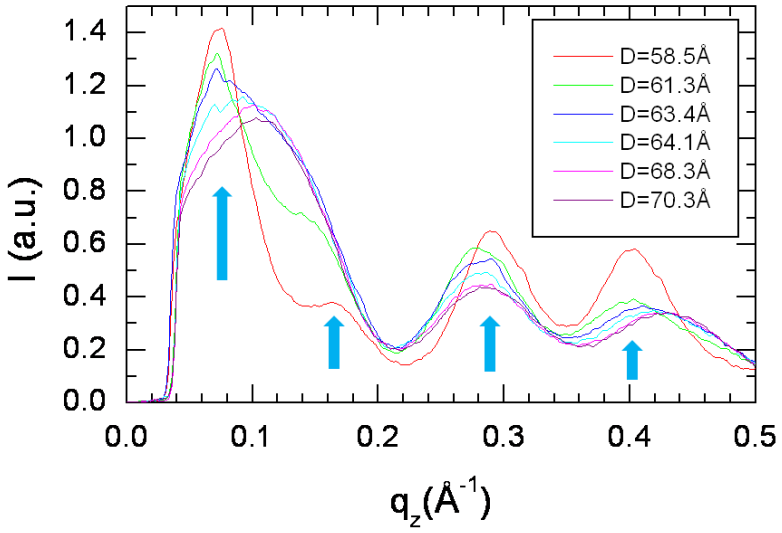


Figure 3.5: Side peak intensity along the $q_z$ direction centered at $q_r \sim 0.08$ Å$^{-1}$ (averaged over a range of qr~0.02 Å$^{-1}$) for the six images in Fig. 3.4. The arrows indicate the positions of the satellite peaks for the curve with D=58.5Å.

## 3.5 Mathematical description of the correlation between scattering entities

Following the traditional wave vector description of x-ray scattering, the scattering amplitude is given by

$$A(\mathbf{q}) = \sum_j F_j(\mathbf{q}) \exp(-i\mathbf{q} \bullet \mathbf{R}_j) \quad , \tag{3.1}$$

where $F_j(\mathbf{q})$ is the form factor and $\mathbf{R}_j$ is the position of the jth scattering entity. For simplicity, we assume the scattering entities are all the same, then we can use $F(\mathbf{q})$ for all of the $F_j(\mathbf{q})$. Assuming the number of the scattering entities is N, the scattering intensity $I(\mathbf{q})$ is

$$
\begin{aligned}
I(\mathbf{q}) &= A(\mathbf{q}) \times A^*(\mathbf{q}) = \sum_m \sum_n F(\mathbf{q}) F^*(\mathbf{q}) \exp(-i\mathbf{q} \bullet (\mathbf{R}_m - \mathbf{R}_n)) \\
&= \sum_{m=n} F(\mathbf{q}) F^*(\mathbf{q}) + \sum_{m \neq n} F(\mathbf{q}) \sum_n F^*(\mathbf{q}) \exp(-i\mathbf{q} \bullet (\mathbf{R}_m - \mathbf{R}_n)) \\
&= N |F(\mathbf{q})|^2 + |F(\mathbf{q})|^2 \sum_{m \neq n} \exp(-i\mathbf{q} \bullet (\mathbf{R}_m - \mathbf{R}_n)) \\
&= N |F(\mathbf{q})|^2 \left(1 + \frac{1}{N} \sum_{m \neq n} \exp(-i\mathbf{q} \bullet (\mathbf{R}_m - \mathbf{R}_n))\right) \\
&= N |F(\mathbf{q})|^2 S(\mathbf{q})
\end{aligned}
\tag{3.2}
$$

$$
S(\mathbf{q}) = 1 + \frac{1}{N} \sum_{m \neq n} \exp(-i\mathbf{q} \bullet (\mathbf{R}_m - \mathbf{R}_n)) \tag{3.3}
$$

$S(\mathbf{q})$ is the structure factor reflecting the positional correlation between the scattering entities and it satisfies $S(\mathbf{q}) \geq 0$ at any $\mathbf{q}$ value because $I(\mathbf{q})$, $|F(\mathbf{q})|^2$,and N in equation (3.2) are all nonnegative.

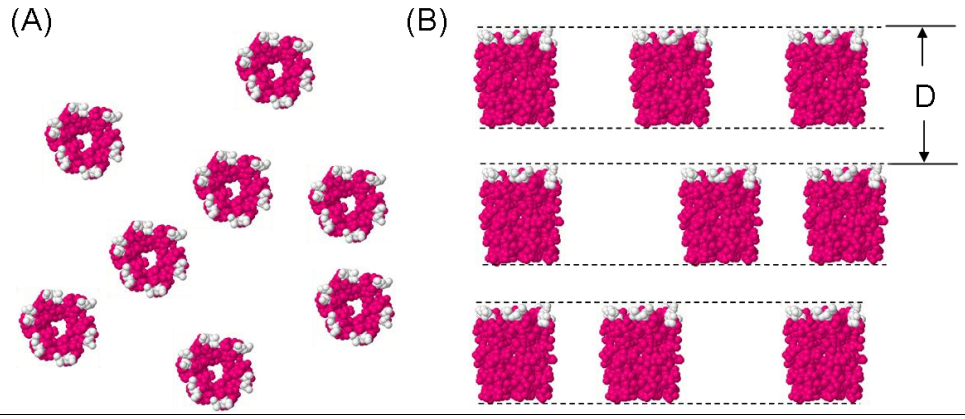


Figure 3.6: (A) Top view of the scattering entities distributed like a 2-D fluid. (B) Side view of the multilayer system with repeat distance D.

Figure 3.6 illustrates the system we are going to describe in the later sections. It is composed of M layers parallel to each other with repeat distance D. In each layer the scattering entities are distributed like a 2-D fluid. This means that the pair distribution

function n(**r**), which describes how the density of the surrounding entities varies as a function of the distance from a typical one, only depends on the magnitude of **r**, not the direction of **r**. For the correlation between different layers, jth and kth layers for example, we employ a second type of pair distribution function $n_{j,k}(\mathbf{r})$ following [96]. Similar to n(**r**), $n_{j,k}(\mathbf{r})$ only depends on the magnitude of **r** in the in plane direction (parallel to each layer). In the following sections, we are going to explore the structure factor in two cases.

### 3.5.1 Case 1: independent layers

When there is no correlation between different layers, the system can be simplified to a 2-D problem, which means we only need to consider one layer with N scattering entities. Then the 3-D vector **R** in equation (3.3) becomes a 2-D in plane vector **r**.

$$S(\mathbf{q}) = 1 + \frac{1}{N}\sum_{m\neq n}\exp(-i\,\mathbf{q}\bullet(\mathbf{R}_m - \mathbf{R}_n))$$

$$= 1 + \frac{1}{N}\sum_{m\neq n}\exp(-iq_r\bullet(\mathbf{r}_m - \mathbf{r}_n)) \qquad (3.4)$$

Using the concept of the pair distribution function n(**r**) introduced in the previous section we can convert the summation in equation (3.4) to integration.

$$S(\mathbf{q}) = 1 + \frac{1}{N}\int n(\mathbf{r})\exp(-iq_r\bullet\mathbf{r})\,d^2\,\mathbf{r}$$

$$= 1 + \frac{1}{N}\int\int_0^{\pi} n(r)\exp(-iq_r r\cos(\theta))r\,dr\,d\theta \qquad (3.5)$$

The integration over θ can be done by introducing a zeroth order Bessel function $J_0(x)$ [99].

$$S(\mathbf{q}) = 1 + \frac{1}{N}\int n(r)J_0(q_r r)2\pi\, r\,dr$$

$$= 1 + \frac{1}{N}\int (n(r) - \bar{n})\, J_0(q_r r) 2\pi\, r dr + \frac{\bar{n}}{N}\int J_0(q_r r) 2\pi\, r dr \qquad (3.6)$$

From equation (3.6) we see that the structure factor does not depend on $q_z$, which means that the scattering intensity along the $q_z$ direction is only dependent on the form factor of a single scattering entity based on equation (3.2). The integral of the third term in equation (3.6) is confined to a small $q_r < 2\pi/L$ region, where L is the length scale of the sample, typically a few millimeters, which makes the third term negligible for our experimental condition. We can then simplify the structure factor to

$$S(\mathbf{q}) \approx 1 + \frac{1}{N}\int (n(r) - \bar{n})\, J_0(q_r r) 2\pi\, r dr \quad . \qquad (3.7)$$

Substituting equation (3.7) to (3.2) we have

$$I(q_r) = N\,|F(q_r)|^2 \left(1 + \frac{1}{N}\int (n(r) - \bar{n})\, J_0(q_r r) 2\pi\, r dr\right) \quad . \qquad (3.8)$$

By using Hankel transform [100], the radial pair distribution function can be expressed as

$$n(r) = \bar{n} + \frac{N}{2\pi}\int \left(\frac{I(q_r)}{N\,|F(q_r)|^2} - 1\right) J_0(q_r r)\, q_r dq_r \quad . \qquad (3.9)$$

The radial pair distribution function n(r) is a particularly useful tool to describe the structure of a system [101]. In a solid, the radial pair distribution function has an infinite number of sharp peaks whose separations and heights are characteristic of the lattice structure. While in liquid systems, it has a small number of peaks at short distances, superimposed on a steady decay to a constant value at longer distances [102].

### 3.5.2 Case 2: correlated layers

When there is correlation between different layers, we need to consider the interference of the scattering entities both within one layer and between different layers. In order to describe the in plane position and in which layer the entity is, we introduce a second index as $\mathbf{R}_{m,j}$ for the position of the mth entity in layer j. Then $S(\mathbf{q})$ becomes

$$S(\mathbf{q}) = 1 + \frac{1}{N}\sum_{m\neq n}\exp(-i\,\mathbf{q}\bullet(\mathbf{R}_m - \mathbf{R}_n))$$

$$= 1 + \frac{1}{N}\sum_{m\neq n}\sum_{j}\exp(-i\,\mathbf{q}\bullet(\mathbf{R}_{m,j} - \mathbf{R}_{n,j})) + \frac{1}{N}\sum_{m,n}\sum_{j\neq k}\exp(-i\,\mathbf{q}\bullet(\mathbf{R}_{m,j} - \mathbf{R}_{n,k})) \quad . \quad (3.10)$$

Next we convert the 3-D vector $\mathbf{R}_{m,j}$ into a 2-D in plane vector $\mathbf{r}_{m,j}$ and $z_j$ which describes the jth layer position along the layer normal.

$$S(\mathbf{q}) = 1 + \frac{1}{N}\sum_{m\neq n}\sum_{j}\exp(-iq_r\bullet(\mathbf{r}_{m,j} - \mathbf{r}_{n,j}))$$

$$+ \frac{1}{N}\sum_{m,n}\sum_{j\neq k}\exp(-iq_r\bullet(\mathbf{r}_{m,j} - \mathbf{r}_{n,k}))\times\exp(-iq_z(z_j - z_k)) \quad (3.11)$$

Using the concept of the pair distribution function in one layer $n_{j,j}(\mathbf{r})$ and the pair distribution function in two different layers $n_{j,k}(\mathbf{r})$ introduced previously we can convert the summation in equation (3.11) to integration.

$$S(\mathbf{q}) = 1 + \frac{1}{N}\sum_{j}\int n_{j,j}(\mathbf{r})\exp(-iq_r\bullet\mathbf{r})\,d^2\mathbf{r}$$

$$+ \frac{1}{N}\sum_{j\neq k}\exp(-iq_z(z_j - z_k))\times\int n_{j,k}(r)\exp(-iq_r\bullet\mathbf{r})\,d^2\mathbf{r}$$

$$= 1 + \frac{1}{N}\sum_{j,k}\exp(-iq_z(z_j - z_k))\times\int n_{j,k}(\mathbf{r})\exp(-iq_r\bullet\mathbf{r})\,d^2\mathbf{r}$$

$$= S_{0,0}(q_r) + 2\cos(q_z D)S_{1,0}(q_r) + 2\cos(2Dq_z)S_{2,0}(q_r) + \ldots\ldots \quad (3.12)$$

The definition of $S_{j,k}(q_r)$ is

$$S_{j,k}(q_r) = \delta_{j,k} + \frac{1}{N}\int (n_{j,k}(r) - \bar{n}) \exp(-iq_r \bullet \mathbf{r})\, d^2\mathbf{r} + \frac{\bar{n}}{N}\int \exp(-iq_r \bullet \mathbf{r})\, d^2\mathbf{r}$$
$$\approx \delta_{j,k} + \frac{1}{N}\int (n_{j,k}(\mathbf{r}) - \bar{n}) \exp(-iq_r \bullet \mathbf{r})\, d^2\mathbf{r}$$
$$= \delta_{j,k} + \frac{1}{N}\int (n_{j,k}(r) - \bar{n}) J_0(q_r r) 2\pi\, r dr \qquad (3.13)$$

To derive equation (3.12), which is the same as in [96], we assumed that the system is symmetrical around layer 0. The difference between equation (3.7) and equation (3.12) is reflected by the second and third terms in equation (3.12). These additional terms describe the correlation between different layers which is absent in the independent layer model.

## 3.6 Qualitative explanation of the experimental data

When the correlation between different layers decays fast enough with the distance between different layers, we only need to focus on the nearest neighbor contribution and ignore the terms beyond the second one in equation (3.12). The structure factor of the system can be simplified to

$$S(q_r, q_z) = S_{0,0}(q_r) + 2\cos(q_z D) S_{1,0}(q_r) \quad . \qquad (3.14)$$

Because $S_{0,0}(q_r) \geq 0$ as shown previously, the maximum of the structure factor is reached when $\cos(q_z d)$ either equals 1 ($q_z$=0, $\pm 2\pi/D$, $\pm 4\pi/D$,...) or -1 ($q_z = \pm\pi/D$, $\pm 3\pi/D$,...), depending on the sign of $S_{1,0}(q_r)$ at the side peak position. For the case of Alm:diC22:1PC 1:10, the four maxima in Fig. 3.5 at D=58.5 Å are listed in Table 3.1. In the same table we listed the calculated $\pi/D$, $3\pi/D$, $5\pi/D$, and $7\pi/D$. By comparison we see that the experimental maxima correspond well to $(2n-1)\pi/D$, where n=1, 2, 3, 4. In

chapter 5 we are going to present extra data showing that the maximum indeed does not occur at $q_z=0$ when there is correlation between different layers. This leads to the conclusion that the sign of $S_{1,0}(q_r)$ is negative at the side peak position, so when $\cos(q_z d)$ equals -1, the structure factor has maxima at $q_z=\pm\pi/D, \pm 3\pi/D$,..., and so on.

Table 3.1: Peak positions in Fig. 3.5 for D=58.5 Å and $(2n-1)\pi/D$ with D=58.5 Å.

| peak 1 ($Å^{-1}$) | peak 2 ($Å^{-1}$) | peak 3 ($Å^{-1}$) | peak 4 ($Å^{-1}$) |
|---|---|---|---|
| 0.07 | 0.17 | 0.29 | 0.40 |
| $\pi/D$ ($Å^{-1}$) | $3\pi/D$ ($Å^{-1}$) | $5\pi/D$ ($Å^{-1}$) | $7\pi/D$ ($Å^{-1}$) |
| 0.05 | 0.16 | 0.27 | 0.38 |

### 3.6.1 Hard disk correlation

To illustrate the shape of $S_{1,0}(q_r)$, we used MC simulations in combination with a 2-D hard disk interaction model [103] to calculate $S_{1,0}(q_r)$ for the model established in section 3.5.2 (correlated layers) with each layer having N solid disks. In each layer, no pair of disks can move closer than $2\times$R. For the correlation between the neighboring layers, we introduce a second hard disk radius r, which means no two disks in the neighboring layers can get closer than $2\times$r. The simulation procedure is to generate enough states ($>10^5$) satisfying the above conditions. For each state the disks in the neighboring layers around each disk are sorted into distance bins. The number of neighbors in each bin is then averaged over the entire ensemble. Once the averaged radial pair distribution function $n_{1,0}(r)$ is obtained, we can then calculate the structure factor $S_{1,0}(q_r)$ by using equation (3.13). An example of N=120, R=20Å, r=5Å and area packing fraction (the area

occupied by the disks divided by the total area) η=0.42 is shown in Fig. 3.7. From the figure we see that for hard disk type correlation between neighboring layers, the structure factor $S_{1,0}(q_r)$ is negative at the side peak position, which explains why the maximum occurs off the equator. In the same figure we also plotted the radial pair distribution function $n_{0,0}(r)$ and the structure factor $S_{0,0}(q_r)$ from the same simulations. Unlike $S_{1,0}(q_r)$, $S_{0,0}(q_r)$ is positive at all $q_r$ values. It first increases rapidly to $q_r \sim \pi/R$ and then oscillates around one.

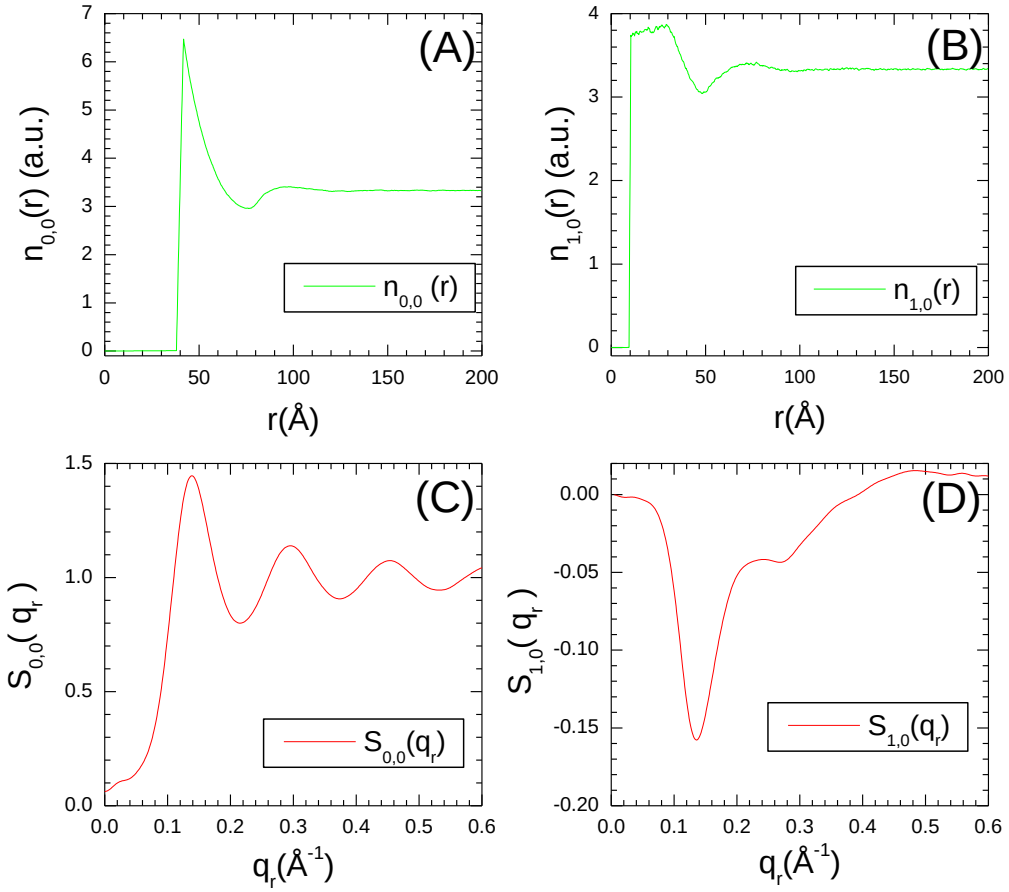


Figure 3.7: Radial pair distribution function (A) $n_{0,0}(r)$ within one layer and (B) $n_{1,0}(r)$ between neighboring layers. Structure factors (C) $S_{0,0}(q_r)$ and (D) $S_{1,0}(q_r)$ are obtained based on equation (3.13).

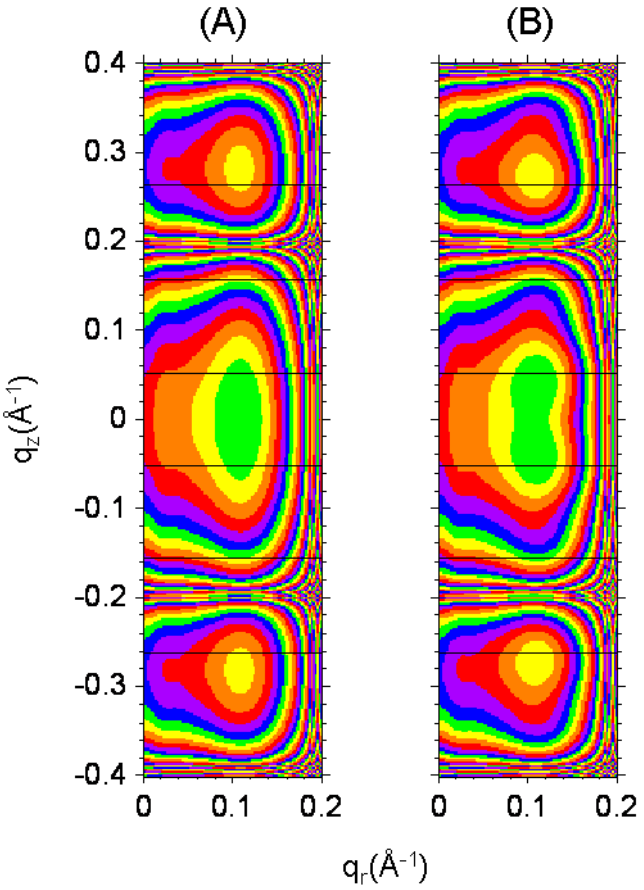


Figure 3.8: Scattering intensity (log scale) of the hard disk model for (A) independent layers and (B) correlated layers using equation (3.14). The solid lines indicate the position of $q_z=(2n-1)\pi/D$ with D=60 Å.

Figure 3.8 shows the log scale of the theoretical scattering intensity in the reciprocal space using equation (3.2) and Fig. 3.7. The form factor was calculated by assuming a cylindrical shaped scattering entity with height h=30 Å and radius R=20 Å.

$$
\begin{aligned}
|F(\mathbf{q})|^2 &= \left|\int \exp(i\mathbf{q}\bullet\mathbf{R})\, d^3\mathbf{R}\right|^2 \\
&= \left|\iint \exp(iq_r \bullet \mathbf{r} + iq_z z)\, d^2\mathbf{r}dz\right|^2 \\
&= \left|\frac{RJ_1(q_r R)}{q_r}\right|^2 \times \left|\frac{2\sin(q_z h/2)}{q_z}\right|^2
\end{aligned}
\tag{3.15}
$$

where $J_1(x)$ is the first order Bessel function. For the no correlation case $S_{0,0}(q_r)$ in Fig. 3.7C was used as the structure factor and for the correlated case $S_{0,0}(q_r)$ and $S_{1,0}(q_r)$ in Fig 3.7C and D were used based on equation (3.14) with the layer repeat distance D=60Å. From Fig. 3.8 we see that when there is no correlation between different layers, the maximum of the scattering peak is at the equator. When there are correlations between different layers, the saddle point centered at the equator gives peanut shaped contours in Fig. 3.8 and the position of the maximum intensity shifts away from the equator towards $q_z \sim \pm\pi/D$. Satellite peaks at larger $q_z$ around $\pm 5\pi/D$ similar to Fig. 3.5 can also be seen in Fig. 3.8A and B. However they are more likely due to the form factor of the cylindrically shaped scattering entities (Alm bundles) since they are present both with and without correlations between neighboring layers, although the position is a little different.

### 3.6.2 Lennard-Jones type correlation

Although the hard disk type correlation between the disks in neighboring layers shows the right trend of the side peaks as a function of the hydration level in section 3.3 and 3.4, the interaction formula is certainly non-physical and oversimplified. A better description of the interaction should include similar repulsive interactions as the hard

disk type correlation at short distance and long range attractive interaction at large distance (van der Waals interaction). Lennard-Jones (L-J) potential [104] serves a good model for this type of interaction.

$$V(r) = \varepsilon\left(\left(\frac{\sigma}{r}\right)^{12} - \left(\frac{\sigma}{r}\right)^{6}\right) \quad , \tag{3.17}$$

In order to illustrate how the structure factor arising from the L-J type interaction between neighboring layers looks, MC simulations are carried out similar to the previous section. However, the situation is little bit more complicated this time as we need to calculate the potential energy of all of the pairs during each simulation step. The general method applied in this thesis is the Metropolis algorithm [95] as has been introduced in chapter 2. First we generate two layers of randomly distributed disks satisfying the hard disk condition within each layer. The disks at the first layer are moved one by one by a random distance $s=s_{max}\times ran$ (ran is a random number between 0 and 1) in a random direction from their original positions. After each movement, the new position is first tested by the hard disk condition. If it fails, the disk is moved back to its original position. Otherwise the difference of the L-J interaction energy $\Delta E$ is calculated and the Boltzmann factor $p=\exp[-\Delta E / k_B T]$ is compared with a randomly generated number r (uniformly distributed between 0 and 1). The new position of the disk is only accepted if $p>r$. After all of the attempts of the disks in the first layer, the disks in the second layer are subjected to the same procedure. One iteration is finished when all of the disks have attempted a movement. The rate of successful attempts is calculated during each iteration and the magnitude of the movement distance $s_{max}$ is adjusted accordingly (decrease $s_{max}$ if

the rate is two low, <50%, and increase $s_{max}$ if the rate is too large, >80%). Periodic boundary conditions are applied: disks which exit at one side will reenter at the opposite side.

Figure 3.9 shows an example of N=120, R=20 Å, $\varepsilon=1k_BT$, $\sigma=10$ Å and the area packing fraction $\eta=0.42$ (N is the number of disks in each layer, R is the disk radius as well as the hard disk condition in each layer, $\varepsilon$ and $\sigma$ are the parameters for the L-J potential in equation (3.17)). By comparing it with Fig. 3.7 we see that the L-J type interaction between the neighboring layers with the above parameters has only a minor effect on the radial pair distribution function $n_{0,0}(r)$ within one layer. This is not surprising since the same hard disk condition was applied for the disks within one layer and the correlation between neighboring layers is not very strong. As a result the structure factor $S_{0,0}(q)$ is almost not changed at all. The radial pair distribution function $n_{1,0}(r)$ due to the L-J interaction is slightly different, especially at the range near $\sigma$, where a small peak can be seen which is absent in the hard disk type correlation. However, the transformed structure factor $S_{1,0}(q)$ has similar negative values at $q\sim0.15$ $Å^{-1}$ which is consistent with the experimental observation.

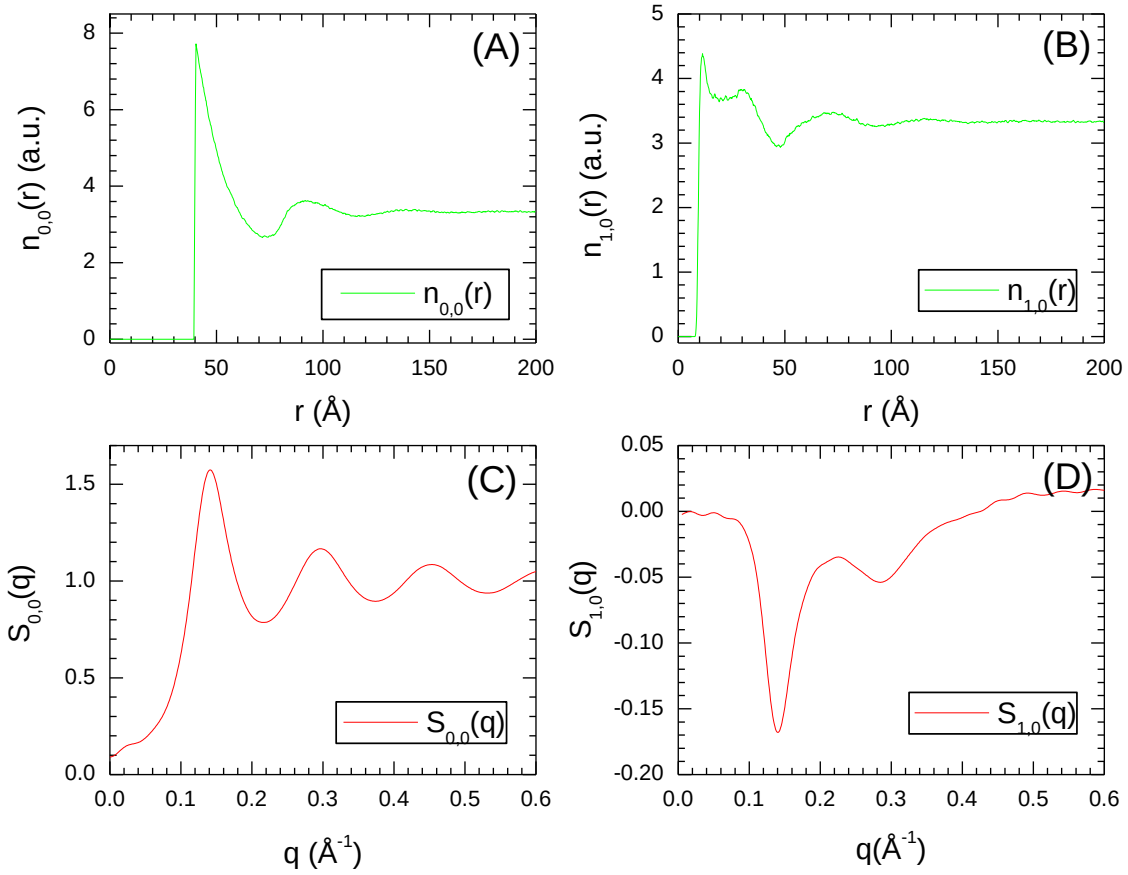


Figure 3.9: Lennard-Jones type interaction between the disks in neighboring layers. Radial pair distribution functions for (A) within one layer and (B) between neighboring layers. Structure factors for (C) within one layer and (D) between neighboring layers. ($\varepsilon$=1$k_B$T, $\sigma$=10 Å, R=20 Å, N=120, $\eta$=0.42)

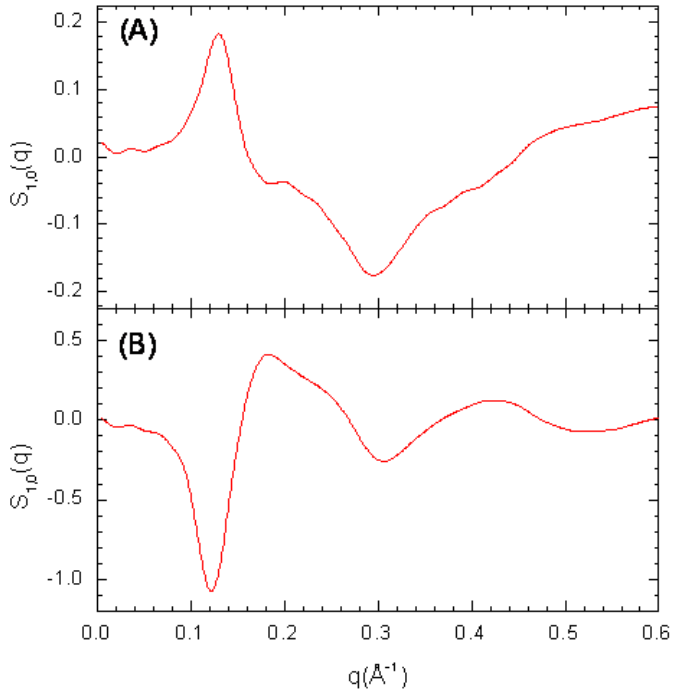


Figure 3.10: Structure factors for (A) large ε ($8k_BT$) and (B) large σ (30 Å) of the L-J type interaction between disks in neighboring layers.

The parameters chosen in the last paragraph are not random. In fact, when the magnitude of the L-J potential ε increases to $8k_BT$, $S_{1,0}(q)$ becomes positive at q~0.15 Å$^{-1}$ as shown in Fig. 3.10A. This will make the satellite peaks appear at $q_z$=0, ±2π/D, ±4π/D which contradicts the experimental result and hence is forbidden. Another variable for the L-J type interaction is σ which indicates the distance at which the sign of interaction (repulsive or attractive) switches. As shown in Fig. 3.10B, large σ (30 Å) results in the appearance of the strong positive peak at q~0.2 Å$^{-1}$ in addition to the distortion of the disk distribution in a single layer. This again is not allowed.

Other types of correlations between disks in neighboring layers are also tried out applying MC simulations, including Gaussian type repulsive interaction and Gaussian type attractive interaction. None of them was able to generate negative values of the structure factor $S_{1,0}(q_r)$ at $q_r$~0.15 $Å^{-1}$. The success of the hard disk type correlation and the L-J type correlation in demonstrating the off equator side peak as shown in Fig. 3.8 implies that the interaction between the Alm bundles is repulsive at short range distances and neutral [96]or weakly attractive at large distances.

## 3.7 Conclusions

The induced correlation along the sample normal between inclusions in different layers due to sample dehydration can be studied by investigating the shape of the scattering peaks in reciprocal space. For the oriented multilayer samples containing Alm peptides, when the correlation is negligible, the in-plane scattering from Alm bundles is a Bragg rod shaped peak centered at $q_z$=0. As the sample gets dehydrated, the lateral correlation between Alm bundles in different layers causes the position of the scattering peak, which is related to the layer repeat distance, shift away from the equator. The fact that the first order scattering peak is off the equator is indicative of a repulsive interaction at short distances between Alm bundles in different layers, consistent with the interpretation by another group [96].

# Chapter 4

# Analysis of alamethicin bundle structure

## 4.1 Introduction

In chapter 3 we have shown that when the oriented multilayer sample is sufficiently hydrated, the correlations between Alm bundles in different layers are negligible. This simplifies the calculation of the structure factor which describes the positional correlations between the peptide bundles to a 2-D in-plane case. In this chapter, first we will present the theoretical derivation of the scattering from peptide bundles in a lipid sea. Then we will apply several models to analyze the in-plane scattering by peptide bundles at the condition where there are negligible correlations between different layers by using the derived mathematical expression. For the scattering in the $q_z$ direction, the length scale of the peptide bundle along the bilayer normal is estimated based on a cylindrical bundle model. For the scattering in the $q_r$ direction, the situation is more complicated. First we need to evaluate the correlation between the peptide bundles in the in-plane direction. This is done by applying a hard disk model [103]. We also need to calculate the form factor of the peptide bundle in the in-plane direction. This is done by two approaches. One is to model the peptide bundle as a cylinder. The other one is to use MD simulation results of Alm bundles in a lipid bilayer. The main result is that the number N of peptides per bundle is greater in diC22:1PC and this has a good physical explanation.

## 4.2 Scattering by peptide bundles in a lipid sea

Here we present the theoretical derivation of the scattering by peptide bundles in a lipid sea following [105].

$$\mathrm{I}(\mathbf{q}) = \int\int \rho(\mathbf{R})\rho(\mathbf{R}')\exp[\,i\mathbf{q}\bullet(\mathbf{R}'-\mathbf{R})]\mathrm{dV}(\mathbf{R})\mathrm{dV}(\mathbf{R}') \tag{4.1}$$

where **q**, **R** and **R**' are 3-D vectors. The integration can be divided into lipid occupied space $\int_L$ where the electron density is $\rho_L$, and peptide bundle occupied space $\int_P$ where the electron density is $\rho_P$.

$$\mathrm{I}(\mathbf{q}) = \left\{\int_P \rho_P(\mathbf{R})\int \rho(\mathbf{R}') + \int_L \rho_L(\mathbf{R})\int \rho(\mathbf{R}')\right\}\times\exp[i\mathbf{q}\bullet(\mathbf{R}'-\mathbf{R})]dV(\mathbf{R})dV(\mathbf{R}'),$$

$$= \left\{\begin{array}{l}\int_P \rho_P(\mathbf{R})\int_L \rho_L(\mathbf{R}') + \int_P \rho_P(\mathbf{R})\int_P \rho_P(\mathbf{R}') \\ + \int_L \rho_L(\mathbf{R})\int_L \rho_L(\mathbf{R}') + \int_L \rho_L(\mathbf{R})\int_P \rho_P(\mathbf{R}')\end{array}\right\}\times\exp[i\mathbf{q}\bullet(bR'-\mathbf{R})]dV(\mathbf{R})dV(\mathbf{r}')$$

$$= \left\{\begin{array}{l}\int_P \rho_P(\mathbf{R})\int \rho_L(\mathbf{R}') - \int_P \rho_P(\mathbf{R})\int_P \rho_L(\mathbf{R}') + \int_P \rho_P(\mathbf{R})\int_P \rho_P(\mathbf{R}') \\ + \int \rho_L(\mathbf{R})\int \rho_L(\mathbf{R}') - \int \rho_L(\mathbf{R})\int_P \rho_L(\mathbf{R}') \\ - \int_P \rho_L(\mathbf{R})\int \rho_L(\mathbf{R}') + \int_P \rho_L(\mathbf{R})\int_P \rho_L(\mathbf{R}') \\ + \int \rho_L(\mathbf{R})\int_P \rho_P(\mathbf{R}') - \int_P \rho_L(\mathbf{R})\int_P \rho_P(\mathbf{R}')\end{array}\right\}\times\exp[i\mathbf{q}\bullet(\mathbf{R}'-\mathbf{R})]dV(\mathbf{R})dV(\mathbf{R}')$$

$$= \left\{ \begin{array}{l} \int \int \rho_L(\mathbf{R})\rho_L(\mathbf{R}') + \int_P \int [\rho_P(\mathbf{R}) - \rho_L(\mathbf{R})]\rho_L(\mathbf{R}') \\ + \int_P \int \rho_L(\mathbf{R})[\rho_P(\mathbf{R}') - \rho_L(\mathbf{R}')] \\ + \int_P \int_P [\rho_P(\mathbf{R}) - \rho_L(\mathbf{R})][\rho_P(\mathbf{R}') - \rho_L(\mathbf{R}')] \end{array} \right\} \times \exp[i\mathbf{q} \bullet (\mathbf{R}' - \mathbf{R}) dV(\mathbf{R}) dV(\mathbf{R}') \quad (4.2)$$

The first term in equation (4.2) represents the scattering by a pure lipid background including Bragg peaks in addition to diffuse scattering for liquid crystalline samples [106-108]. Because this term applies to both samples with and without peptide bundles, this explains the presence of similar diffuse scattering in Fig. 3.1A and B. The second and the third terms are the scattering by a single peptide bundle embedded in a pure lipid background with electron density contrast $\rho_P(\mathbf{R})$- $\rho_L(\mathbf{R})$. They are usually confined to a very small $q_r$ range (if the electron density of the lipid bilayer is uniform in the in-plane direction, these two terms are $\delta(q_r)$ functions) and will be ignored. The fourth term is the excess scattering due to the correlation between peptide bundles in a lipid sea. This peptide bundle induced scattering is

$$I_P(\mathbf{q}) = \int_P \int_P [\rho_P(\mathbf{R}) - \rho_L(\mathbf{R})][\rho_P(\mathbf{R}') - \rho_L(\mathbf{R}')]\} \times \exp[i\mathbf{q} \bullet (\mathbf{R}' - \mathbf{R})] dV(\mathbf{R}) dV(\mathbf{R}') . \quad (4.3)$$

Next, define the form factor as

$$F_P(\mathbf{q}) = \int_P [\rho_P(\mathbf{R}) - \rho_L(\mathbf{R})] \exp[i\mathbf{q} \bullet (\mathbf{R} - \mathbf{R}_a)] dV(\mathbf{R}) \quad (4.4)$$

where $\mathbf{R}_a$ is the coordinate of the molecular axis of bundle a. Equation (4.3) becomes

$$\begin{aligned} I_P(\mathbf{q}) &= \sum_a |F_P(\mathbf{q})|^2 + \sum_a |F_P(\mathbf{q})|^2 \sum_{b \neq a} \exp[i\mathbf{q} \bullet (\mathbf{R}_b - \mathbf{R}_a)] \\ &= N |F_P(\mathbf{q})|^2 S(\mathbf{q}) \end{aligned} \quad (4.5)$$

$$S(\mathbf{q}) = 1 + \sum_{b \neq a} \exp[\, i\mathbf{q} \bullet (\mathbf{R}_b - \mathbf{R}_a)] \tag{4.6}$$

$S(\mathbf{q})$ is the structure factor describing the correlation between peptide bundles. $\mathbf{R}_a$ and $\mathbf{R}_b$ are the coordinates of the molecular axis of bundles a and b.

## 4.3 Model fit in the $q_z$ direction

The problem of the scattering by the peptide bundles can be simplified to a 2-D in-plane case when the correlation between the peptide bundles in different layers is negligible. From equation (4.6) we see that the structure factor $S(\mathbf{q})$ of the peptide bundles in the 2-D case does not depend on $q_z$, because for any pair of $\mathbf{R}_b$ and $\mathbf{R}_a$ the z value along the bilayer normal is the same. Then the scattering intensity by the peptide bundles along the $q_z$ direction only depends on the form factor based on equation (4.5). In other words the structural information of the peptide bundles that are related to the $q_z$ component of the form factor can be obtained by analyzing the scattering in the $q_z$ direction regardless of the correlation between them.

For simplicity, we assume that the peptide bundle has the shape of a cylinder with height h and outside radius b and its electron density is only r (in-plane) dependent. As the lipid bilayer background is in-plane isotropic, we assume that its electron density is only z (bilayer normal) dependent. Then from equation (4.4) we have

$$F_P(\mathbf{q}) = \int_P [\rho_P(\mathbf{R}) - \rho_L(\mathbf{R})] \exp[i\mathbf{q} \bullet (\mathbf{R} - \mathbf{R}_a)] dV(\mathbf{R})$$

$$= \int_P [\rho_P(r) - \rho_L(z)] \exp[iq_z z + iq_r r\cos(\theta)] r\, dr\, d\theta$$

$$= A_1(q_r) \times \frac{\sin(q_z h/2)}{q_z h/2} - A_2 \frac{bJ_1(q_r b)}{q_r} \times F_L(q_z) \quad (4.7)$$

where $A_1(q_r)$ only depends on $q_r$ and $A_2$ is a constant; $F_L(q_z)$ is the form factor of a pure lipid bilayer in the $q_z$ direction.

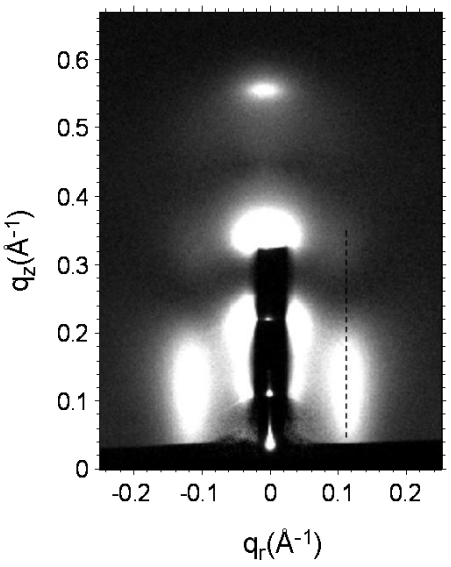


Figure 4.1: Scattering image ($\alpha$=0.2$^o$) for Alm:DOPC 1:10 at D=56.3Å. The scattering intensity along the dashed line is used for the analysis in the $q_z$ direction.

By using equation (4.7) and the known $q_z$ dependence of the scattering intensity from the peptide bundles in Fig. 4.1 in addition to the known form factor of a pure DOPC lipid bilayer [37] which is shown in Fig.4.2, we can estimate the height h of the peptide bundle. First we need to obtain the side peak intensity along the $q_z$ direction as indicated by the dashed line in Fig. 4.1. This is done by taking a thin slice along the $q_z$ direction centered at $q_r$ =0.11Å$^{-1}$. An absorption correction was applied to the obtained intensity [109].

$$Abs(q_z)=[1-\exp(-y)]/y \quad (4.8)$$

where $y=8\pi t/\lambda\mu q_z$; t is the sample thickness (~10μm); λ (~1.18Å) is the x-ray wavelength; μ (~2.5mm) is the x-ray absorption length by lipid samples. We also considered the Lorentz correction for a flat sample. The final formula for the scattering intensity in the $q_z$ direction is

$$I(q_z) = Abs(q_z)\,|F_P(q_z)|^2 / |\mathbf{q}| \quad . \tag{4.9}$$

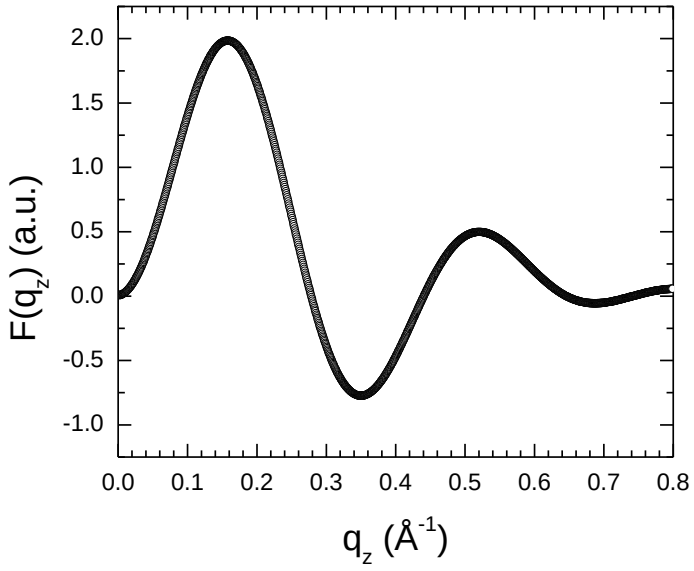


Figure 4.2: Form factor of DOPC along bilayer normal.

Because the absorption correction increases the intensity much faster than the sinc function in equation (4.7) at low $q_z$, we limit the lower bound of the data to $q_z=0.1Å^{-1}$. Lower bounds at $q_z<0.1Å^{-1}$ are also tried. However, the fit becomes worse especially at small $q_z$ region. For the diffuse scattering background due to the first term in equation (4.2) where the side peak sits, it can be approximated by taking the same slice at the same **q** position from a pure DOPC sample at similar hydration level. On the other hand,

the side peak at $q_z$ <0.2Å$^{-1}$, which is the main feature to fit, is much stronger than the background. For simplicity, we can assume the background to be a constant, which will be adjusted during the fitting process. Both methods were applied and they gave similar results. The fitting result of the experimental data to equation (4.9) with a constant background is shown in Fig. 4.3. The height of the cylinder model obtained from the fit is h=33Å, which is very close to the height of an Alm peptide, 32Å, from a crystallography study [32].

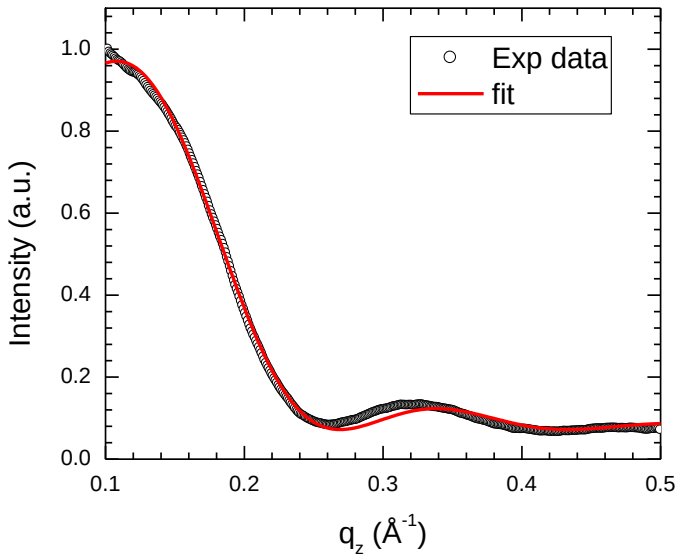


Figure 4.3: Model fit of the side peak intensity along the $q_z$ direction in Fig. 4.1 to equation (4.9).

## 4.4 Model fit in the $q_r$ direction

We have confirmed from the previous section that the source of the side peak at $q_r$ ~0.11Å$^{-1}$ in Fig. 4.1 is consistent with an Alm bundle. In this section we are going to use the scattering intensity along the $q_r$ direction to estimate the lateral size of the peptide bundle in two lipids at two peptide concentrations when there is no correlation between Alm bundles in different layers.

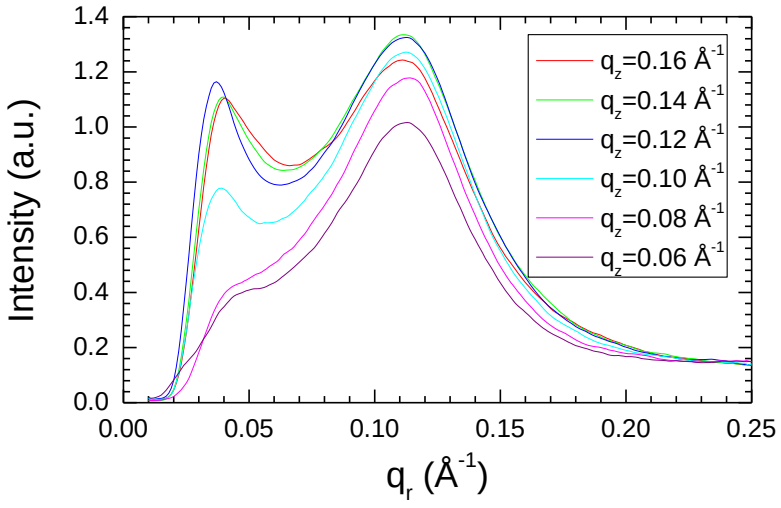


Figure 4.4: Scattering intensity along the $q_r$ direction at different $q_z$ values for Alm:DOPC 1:10 in Fig. 4.1. As $q_z$ varies, the shape of the side peak at $q_r$ ~ 0.11 Å$^{-1}$ does not change much.

Figure 4.4 shows the $q_r$ dependence of the scattering intensity in Fig. 4.1 at six $q_z$ positions. Even though the diffuse scattering background changes significantly, the shape of the side peak centered at $q_r$ ~0.11 Å$^{-1}$ is well preserved, which means the form factor, equation (4.7), can be approximated by $F_P(q_r,q_z)=F(q_r)\times F(q_z)$.

Before peak fitting, the diffuse scattering background where the side peak sits needs to be subtracted out first. This is achieved by fitting the experimental data to two Lorentz distribution functions, $f(q,q_0,\gamma)=\frac{1}{\pi}\frac{\gamma}{(q-q_0)^2+\gamma^2}$, one for the background centered at $q_r$=0 and the other for the side peak whose center is a fitting parameter. This procedure is the same as in Constantin et al. [25]. An example of the decomposition for the side peak and the background for Alm:DOPC 1:10 in Fig. 4.1 at $q_z$~0.14 Å$^{-1}$ is shown in Fig. 4.5. Similar decomposition was performed for other $q_z$ values in Fig. 4.4. All of them result in very similar $q_0$ (the center of the side peak) and $\gamma$ (related to the full width half maximum of the side peak), which confirms our previous statement that the shape of the side peak is almost independent of $q_z$.

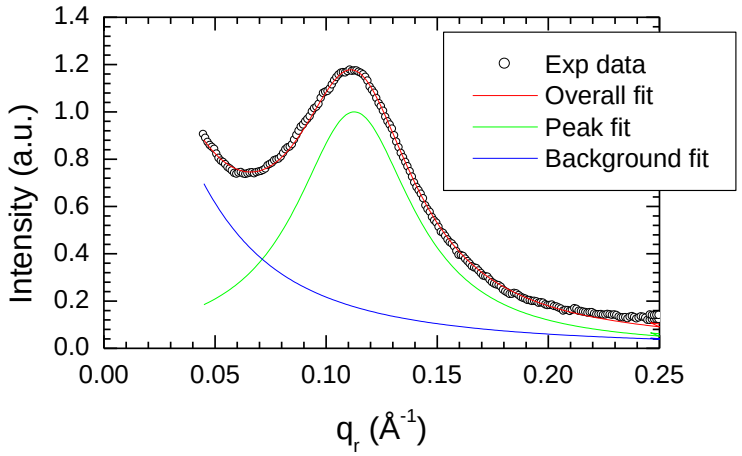


Figure 4.5: Peak decomposition for the side peak and the background in Fig. 4.1 at $q_z$ ~0.14Å$^{-1}$.

### 4.4.1 Form factor of a cylindrical model

Figure 4.6 illustrates an Alm bundle model in a lipid background. The bundle is approximated by a hollow cylinder [22] with outside radius b and inside radius a. In the figure we assumed that the lipid chain region is longer than the half height of the peptide bundle. For chains shorter than the peptide bundle, a similar procedure can be applied.

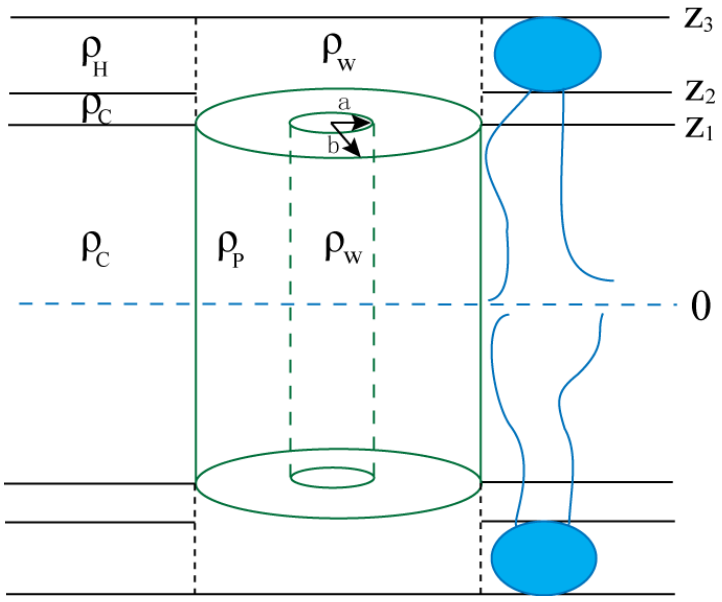


Figure 4.6: Hollow cylinder model of an Alm bundle with inside radius a and outside radius b respectively. $\rho_p$, $\rho_w$, $\rho_c$ and $\rho_H$, are the averaged electron densities of the peptide bundle, water molecules, lipid chain and lipid headgroup region, respectively. The horizontal dashed line in the center indicates the center of the bilayer; $z_1$ indicates the half thickness of the peptide bundle; $z_2$-$z_1$ indicates the remaining lipid chain region above the peptide bundle; $z_3$-$z_2$ indicates the lipid headgroup region.

The form factor of the hollow cylinder model can be calculated as following:

$$F_P(q_r,q_z)=\left\{\begin{array}{l}2\int_0^{z_1}\int_a^b(\rho_P-\rho_C)\exp[iq_r\bullet\mathbf{r}]\cos(q_z z)+\\2\int_0^{z_1}\int_0^a(\rho_W-\rho_C)\exp[iq_r\bullet\mathbf{r}]\cos(q_z z)+\\2\int_{z_1}^{z_2}\int_0^b(\rho_W-\rho_C)\exp[iq_r\bullet\mathbf{r}]\cos(q_z z)+\\2\int_{z_2}^{z_3}\int_0^b(\rho_W-\rho_H)\exp[iq_r\bullet\mathbf{r}]\cos(q_z z)\end{array}\right\}d^2\mathbf{r}dz$$

$$=\left\{\begin{array}{l}\frac{bJ_1(q_r b)-aJ_1(q_r a)}{q_r}\times\frac{2(\rho_P-\rho_C)\sin(q_z z_1)}{q_z}+\\\frac{aJ_1(q_r a)}{q_r}\times\frac{2(\rho_W-\rho_C)\sin(q_z z_1)}{q_z}+\\\frac{bJ_1(q_r b)}{q_r}\times\begin{pmatrix}2(\rho_W-\rho_C)\times(\sin(q_z z_2)-\sin(q_z z_1))+\\2(\rho_W-\rho_H)\times(\sin(q_z z_3)-\sin(q_z z_2))\end{pmatrix}/q_z\end{array}\right\} \quad (4.10)$$

The electron density is $\rho_p\approx0.4$ e/Å$^3$ for Alm peptide, $\rho_C\approx0.3$ e/Å$^3$ for hydrocarbon chains, $\rho_W=0.33$ e/Å$^3$ for water molecules. Because the headgroup region is composed of both lipid headgroup ($\rho\approx0.5$ e/Å$^3$) and water molecules with v:v≈1:1, the averaged electron density of the headgroup region is $\rho_H\approx0.4$ e/Å$^3$.

For a hexamer bundle, b=r/sin(π/6)+ r =15 Å and a= r/sin(π/6)-r =5 Å based on the barrel-stave structure [35]; r=5 Å is the radius of the helical peptide. Figure 4.7 shows the behavior of $bJ_1(q_rb)/q_r$ and $aJ_1(q_ra)/q_r$ at the $q_r$ range of 0-0.2 Å$^{-1}$ which is the fitting range of the side peaks as will be shown later. From the figure we see that $bJ_1(q_rb)/q_r$ changes significantly while $aJ_1(q_ra)/q_r$ acts almost as a constant as a function of $q_r$ and it is small compared to $bJ_1(q_rb)/q_r$. We also notice that the two terms containing $aJ_1(q_ra)/q_r$ in equation (4.10) have opposite signs based on the numerical values of the electron densities which makes their contribution to the overall form factor even smaller. For

these two reasons, the two terms containing $aJ_1(q_ra)/q_r$ are ignored, then equation (4.10) can be approximated by

$$F_P(q_r,q_z) \approx \left\{ \begin{array}{l} \frac{bJ_1(q_rb)}{q_r} \times \frac{2(\rho_P-\rho_C)\sin(q_zz_1)}{q_z} + \\ \frac{bJ_1(q_rb)}{q_r} \times \left( \begin{array}{l} 2(\rho_W-\rho_C)\times(\sin(q_zz_2)-\sin(q_zz_1))+ \\ 2(\rho_W-\rho_H)\times(\sin(q_zz_3)-\sin(q_zz_2)) \end{array} \right)/q_z \end{array} \right\}$$

$$= \frac{bJ_1(q_rb)}{q_r} \times F_1(q_z) \qquad (4.11)$$

where $F_1(q_z)$ only depends on $q_z$. Equation (4.11) shows that once the form factor can be separated into $q_r$ and $q_z$ components, the $q_z$ value will only affect the amplitude of the scattering intensity along the $q_r$ direction, not the shape of it, which is consistent with Fig. 4.4. This means even though we do not have the scattering intensity at $q_z$=0, we are still able to estimate the lateral size scale of the peptide bundle by using the scattering intensity a little off the equator.

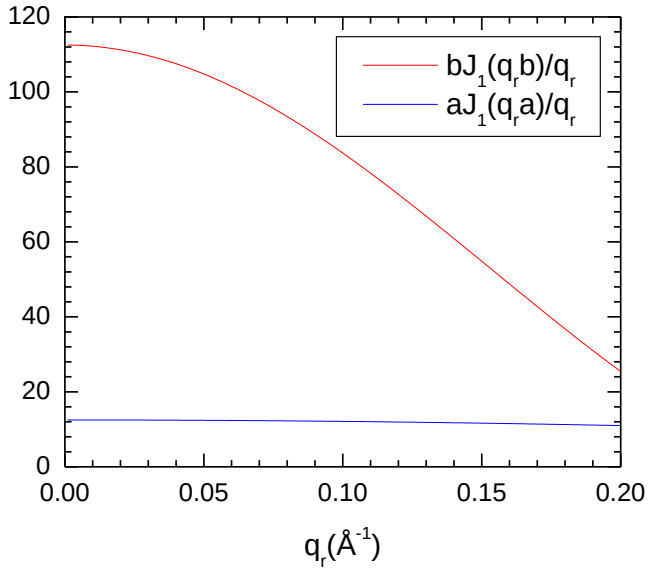


Figure 4.7: Bessel functions of $bJ_1(q_rb)/q_r$ with b=15 Å and $aJ_1(q_ra)/q_r$ with a=5 Å.

Figure 4.8 shows an example of the form factors of the peptide bundles with two different outside radii b. When the outside radius increases from 15 to 20 Å (blue line to red line), the form factor decreases more rapidly with increasing $q_r$.

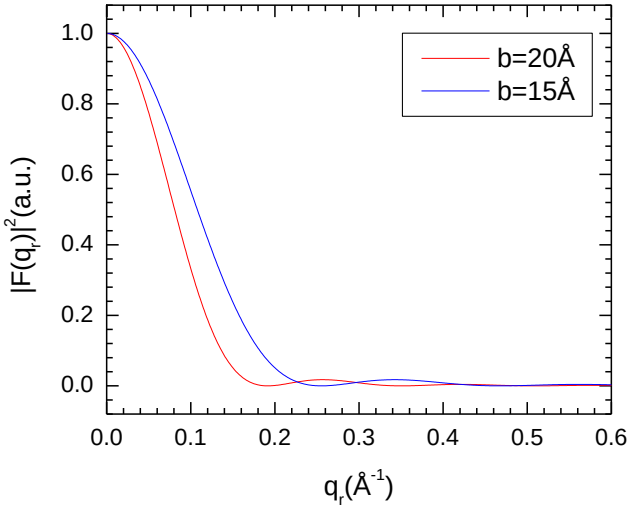


Figure 4.8: Form factor of a cylindrical bundle model based on equation (4.11).

### 4.4.2 Structure factor of the hard disk model

In order to account for the correlation between the peptide bundles in a single bilayer (the structure factor), the 2-D hard disk model was applied as in chapter 3. However, instead of using MC simulations this time we will use the analytical expression of the structure factor $S(q_r)$ which has been derived by Rosenfeld [103].

$$S_{hd}^{-1}(q_r) = 1 + 4\eta\left[ A\left(\frac{J_1(q_r R)}{q_r R}\right)^2 + B\frac{J_0(q_r R)J_1(q_r R)}{q_r R} + G\frac{J_1(2q_r R)}{q_r R}\right] \quad (4.12)$$

$$G = (1-\eta)^{-3/2}$$

$$\chi = \frac{1+\eta}{(1-\eta)^3}$$

$$A = \eta^{-1}[1 + (2\eta - 1)\chi + 2\eta G]$$

$$B = \eta^{-1}[(1-\eta)\chi - 1 - 3\eta G]$$

where $\eta$ is the area packing fraction of the disks and R is the disk radius. Figure 4.9 shows an example of the structure factor S(q) of the hard disk model at three different conditions. The structure factors behave similarly in that S(q) first increases rapidly at low q value and oscillates around one at larger q values. This similarity is based on the fact that the correlation between the disks only exists at small distances (~2R) and disappears at much larger distances. On the other hand, the detailed shape of S(q) is dependent on both R and $\eta$. For the same R, S(q) increases more rapidly at $q<0.16$ Å$^{-1}$ and the width of the first peak at $q\sim0.16$ Å$^{-1}$ becomes narrower when the area packing fraction $\eta$ increases from 0.1 to 0.2 (red line to green line). For the same $\eta$, the first peak position moves to a larger q value and the width of the first peak becomes larger when the disk radius R decreases from 15 to 10 Å (green line to blue line) simply due to the scaling effect for the same packing fraction $\eta$ based on equation (4.12).

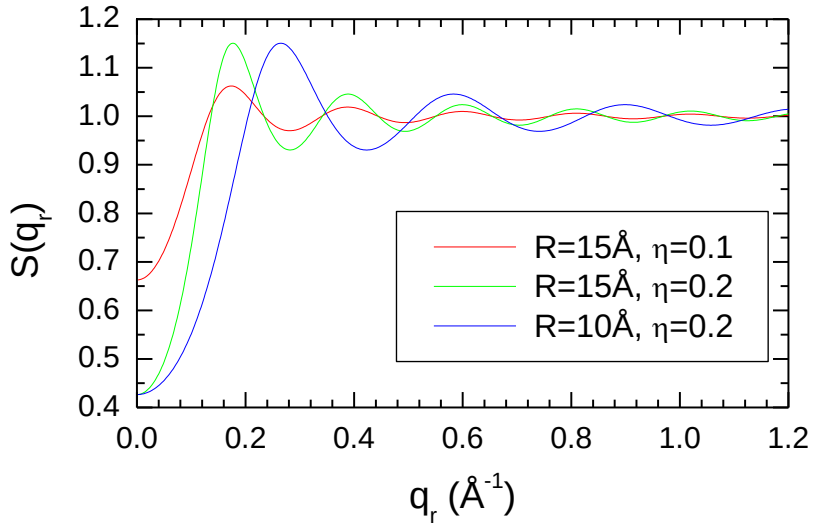


Figure 4.9: An example of the structure factors for the 2-D hard disk model with varying hard disk radius and area packing fraction.

### 4.4.3 Model fit of a cylindrical bundle model

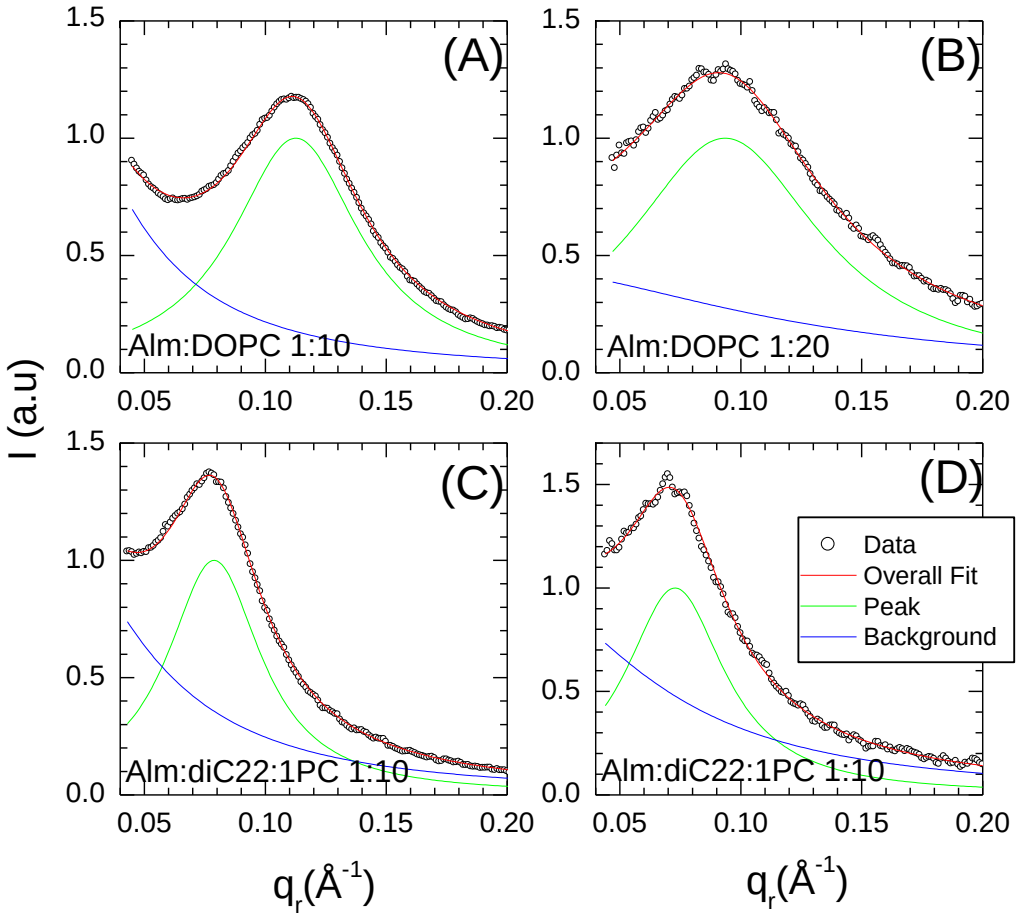


Figure4.10: Side peak decomposition for DOPC and diC22:1PC at two different peptide to lipid ratios, 1:10 and 1:20. The intensity for each sample was obtained by taking a thin slice centered at $q_z$~0.1Å$^{-1}$. The data are noisier at lower peptide concentration due to the weaker side peak.

Figure 4.10 shows the decomposition of the side peaks from the diffuse scattering background for DOPC and diC22:1PC at two peptide concentrations that have observable in-plane scattering by Alm bundles. For both lipids, when the concentration of Alm to lipid ratio decreases from 1:10 to 1:20, the side peak shifts to smaller $q_r$ value,

indicating a larger characteristic length scale between the scattering entities. This trend is similar to Alm in DMPC [25]. Another interesting feature due to the variation of the peptide concentration is that the side peak is wider when the peptide concentration is smaller, consistent with Fig. 4.9. As has been noticed in Fig. 3.2 and 3.4, the center of the side peak is at smaller $q_r$ value for diC22:1PC than for DOPC which also has a wider side peak.

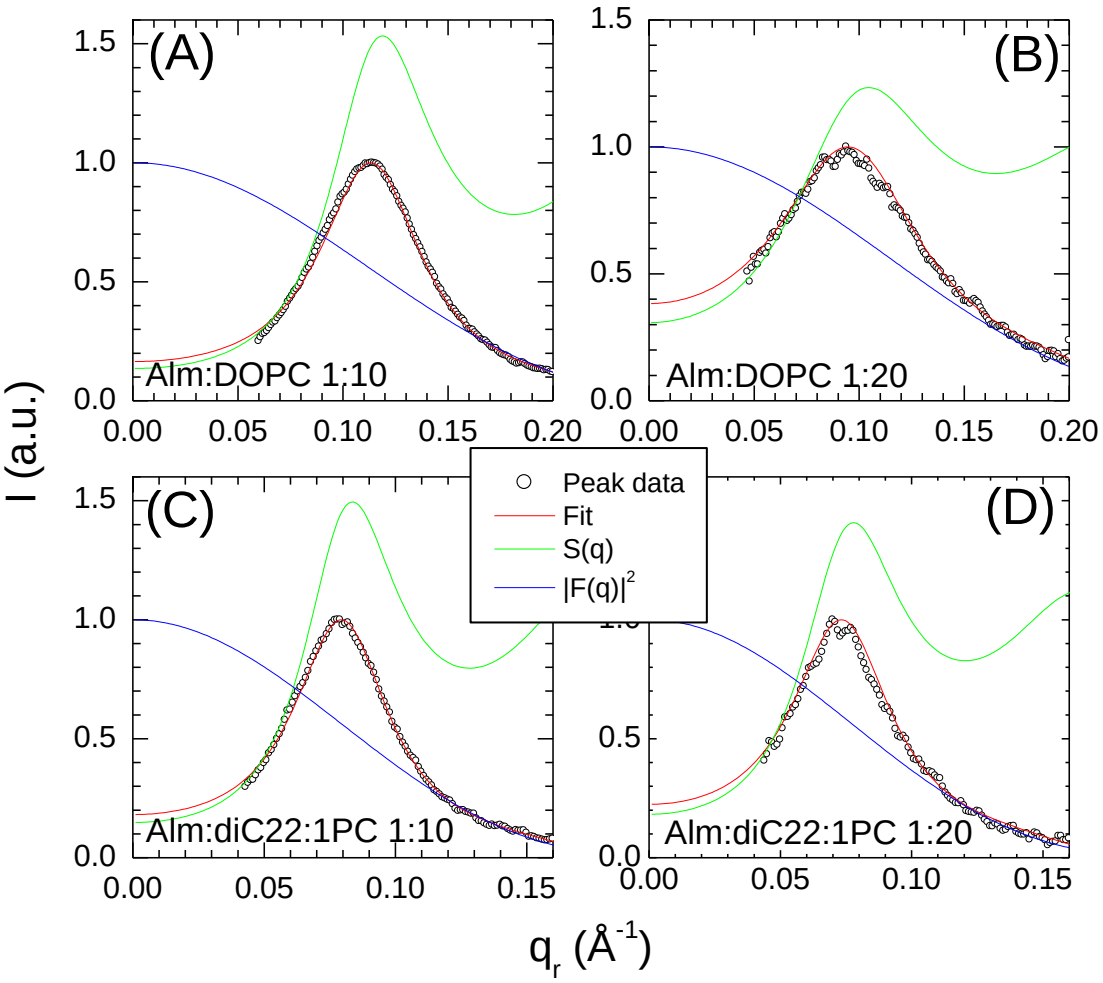


Figure 4.11: Fits of the cylindrical bundle model to the background subtracted side peaks in Fig. 4.10 with structure factors calculated from the hard disk model.

Table 4.1: Fitting parameters for the cylindrical bundle model with hard disk type interaction.

| | R (Å) | b(Å) | N | η | RSS |
|---|---|---|---|---|---|
| Alm:DOPC 1:10 | 23.5 | 13.2 | 4.8 | 0.42 | 0.29 |
| Alm:DOPC 1:20 | 25.7 | 12.9 | 4.6 | 0.27 | 0.49 |
| Alm:diC22:1PC 1:10 | 33.3 | 18.6 | 8.4 | 0.41 | 0.21 |
| Alm:diC22:1PC 1:20 | 35.4 | 19.2 | 8.7 | 0.37 | 0.50 |

Figure 4.11 shows the fits of the background subtracted side peaks along the $q_r$ direction in Fig. 4.10 by using equation (4.12) for the structure factor and equation (4.11) for the form factor. The fitting parameters include the area packing fraction η, the outside radius b of the peptide bundle (the number N of peptides per bundle is related to b by b=r+r/sin(π/N) where r=5 Å is the peptide radius), the hard disk radius R (the hard disk type interaction between peptide bundles is lipid mediated, which means the hard disk radius R can be larger than the outside radius b of the bundle itself). The quality of the model fit to the side peak is indicated by the residual sum of squares (RSS)

$$\mathrm{RSS} = \sum_{i=1}^{N_{points}} \left(I_i(\mathrm{peak}) - I_i(\mathrm{model})\right)^2 \quad . \tag{4.13}$$

The minimum reduced $\chi^2$ criteria was also considered by assuming a Poisson distribution of the scattering intensity at each data point, $\sigma_i^2=I_i$. However, the resulting reduced $\chi^2$ is smaller than 1, which indicates the Poisson distribution overestimates the standard deviation σ. Since we do not have a good knowledge of σ, RSS was used for the best fitting criteria.

The final fitting parameters are listed in Table 4.1. By comparing the results of the two lipids, we see that the hard disk radius R is larger for diC22:1PC than for DOPC. According to Fig. 4.9, the first peak of the structure factor occurs at smaller $q_r$ value for larger hard disk radius R with similar area packing fraction. Then the larger hard disk radius for diC22:1PC is consistent with the smaller $q_r$ value of its side peak position. The fitting results of the size of the peptide bundle, both the number N of peptides per bundle and the outside radius b of the bundle, indicate that the bundle in diC22:1PC is larger than in DOPC. This is consistent with the side peak of diC22:1PC at smaller $q_r$ value than that of DOPC based on the shape of the form factor in Fig. 4.8, although the structure factor is also involved in the prediction of the side peak position.

The fitting results for the same lipid show that the bundle size barely changes when the peptide to lipid ratio decreases from 1:10 to 1:20. However, the disk radius R increases consistently for both lipids when the peptide to lipid ratio decreases. This is consistent with the shift of the side peak position as shown in Fig. 4.11. Constantin et al. [25] also observed this trend and they attributed it to a "soft" repulsive interaction between the bundles. Table 4.1 shows that the outside radius b of the bundle is much smaller than the disk radius R in each case. This confirms our previous suspicion that the disk not only includes the bundle but also some lipid molecules. Then the idea that there are more surrounding lipid molecules attached to each bundle to form larger disks in samples with lower peptide concentration is also consistent with the larger disk radius R for the smaller peptide concentration. Another perspective to explain the decreased disk

radius as the peptide concentration increases is the overlapping effect. Assuming the size of the disk associated with each bundle does not change as a function of the peptide concentration, the possibility of finding disks overlapped increases as the peptide concentration increases [110]. This is equivalent to saying that the apparent size of the disk (the area occupied by all disks divided by the disk number) decreases as the peptide concentration increases.

As pointed out by [25], aside from the short range hard core repulsive interaction between disks, additional long range interactions can also exist. These long interactions can be described by perturbations to the structure factor of the hard disk interactions. Based on random phase approximation (RPA) [102], the perturbed structure factor can be expressed as

$$S(q) = \frac{S_0(q)}{1 + n\beta \tilde{G}(q) \times S_0(q)} \quad , \tag{4.14}$$

where $S_0(q)$ is the structure factor of the unperturbed state, n is the number density of the disks ($n=\eta/\pi R^2$), $\beta=1/k_BT$, and $\tilde{G}(q)$ is the Fourier transform of the perturbation. To illustrate how the modified hard disk interaction (soft disk) affects the fitting results, we introduce a Gaussian type repulsion $G(r)=U_0\exp(-r^2/2\sigma^2)$ as the perturbation to the hard disk interaction [25]. The overall shape of the interaction potential is shown in Fig. 4.12. The Fourier transform of the Gaussian repulsion is

$$\begin{aligned} \tilde{G}(q_r) &= U_0 \int_0^{\infty}\int_0^{2\pi} \exp\left(-\frac{r^2}{2\sigma^2}\right)\exp(-iq_r r\cos(\theta))\, r\, dr\, d\theta \\ &= 2U_0\pi\sigma^2 \exp\left(-\frac{q_r^2\sigma^2}{2}\right) \end{aligned} \tag{4.15}$$

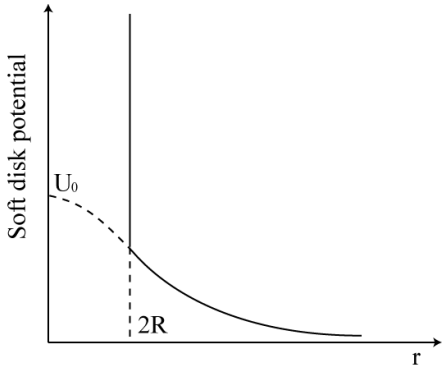


Figure 4.12 The shape of the soft disk interaction potential [25].

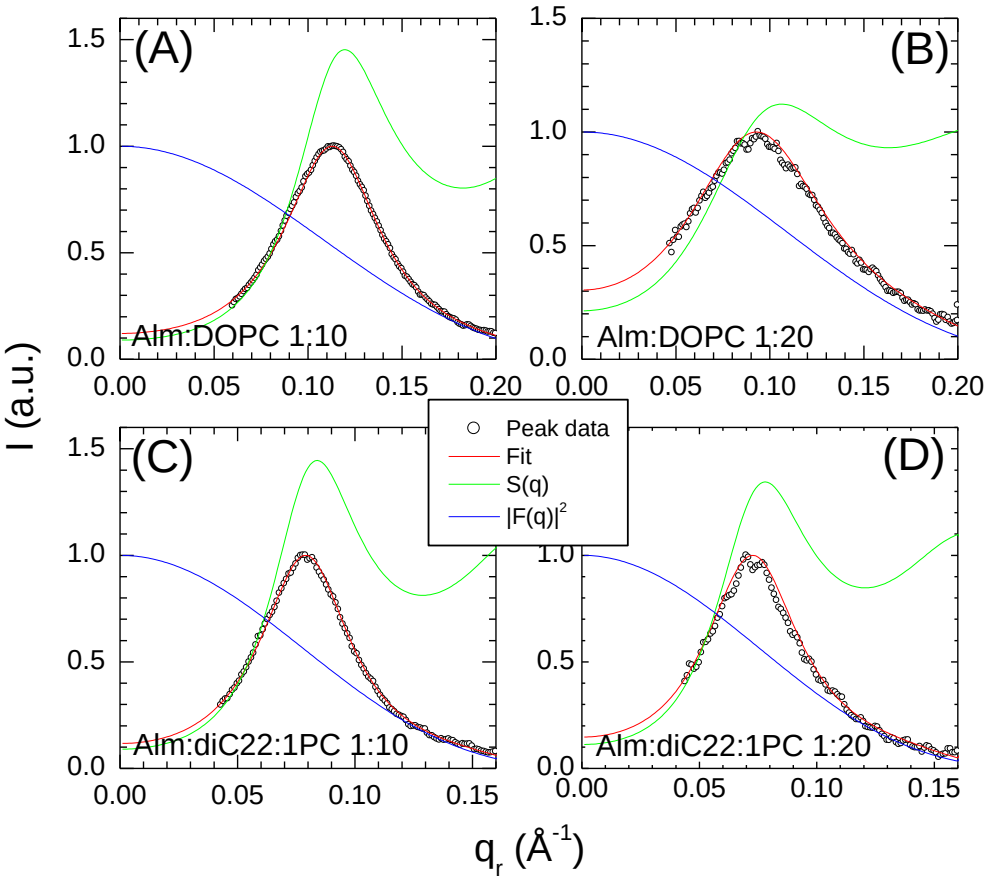


Figure 4.13: Fits of the cylindrical bundle model to the background subtracted side peaks in Fig. 4.10 with structure factors calculated from hard disk interactions perturbed by Gaussian repulsions based on equation (4.14).

Figure 4.13 shows the fits of the modified hard disk interactions with long range Gaussian repulsions to the side peaks in Fig. 4.10. By comparing Fig 4.13 to Fig. 4.11 we see that the fits are improved especially at the small $q_r$ region. The improvement is confirmed by the smaller RSS listed in the last column of Table 4.2. Other fitting parameters for both the hard disk and the soft disk (for the same lipid, the parameters of the Gaussian repulsion was fixed to be the same) are also listed in Table 4.2. The fitting results of the soft disk indicate that the magnitude $U_0$ of the Gaussian repulsion is close to the thermal fluctuation energy $k_BT$ and it is similar for the two lipids. However the decay length $\sigma$ is larger for diC22:1PC than for DOPC. This is consistent with the larger hard disk radius R for diC22:1PC so the magnitude of the perturbation at the soft disk perimeter is similar for both lipids. The magnitude and the decay length of the repulsive interaction of our soft disk are in qualitative agreement with both experimental [25] and theoretical predictions [111, 112]. By comparing the other fitting parameters of the hard disk and the soft disk model we see that the additional Gaussian repulsion has negligible effect on the hard disk radius, area packing fraction, and peptide bundle size. Based on this observation we are only going to consider the hard disk interaction for the model fits with form factors calculated by a different method in the following section.

Table 4.2 Fitting parameters for the cylindrical bundle model with hard disk type interaction perturbed by Gaussian repulsion.

| | R (Å) | b(Å) | N | η | $U_o(k_BT)$ | σ(Å) | RSS |
|---|---|---|---|---|---|---|---|
| Alm:DOPC 1:10 | 23.5 | 13.3 | 4.9 | 0.42 | -- | -- | 0.29 |
| Alm:DOPC 1:10 | 23.4 | 13.7 | 5.1 | 0.40 | 1.3 | 29.5 | 0.10 |
| Alm:DOPC 1:20 | 25.4 | 12.9 | 4.6 | 0.26 | -- | -- | 0.49 |
| Alm:DOPC 1:20 | 25.9 | 13.6 | 5.1 | 0.20 | 1.3 | 29.5 | 0.38 |
| Alm:diC22:1PC 1:10 | 33.2 | 18.6 | 8.4 | 0.40 | -- | -- | 0.21 |
| Alm:diC22:1PC 1:10 | 33.1 | 19.0 | 8.6 | 0.39 | 1.1 | 46.4 | 0.11 |
| Alm:diC22:1PC 1:20 | 34.7 | 18.7 | 8.4 | 0.33 | -- | -- | 0.50 |
| Alm:diC22:1PC 1:20 | 35.3 | 19.6 | 9.0 | 0.34 | 1.1 | 46.4 | 0.45 |

Note: the bundle radius b and the number N of peptides per bundle are related and there is a scaling factor between the experimental data and the product of the form factor and the structure factor.

### 4.4.4 Form factors calculated from MD simulations

A more realistic model of the Alm bundle can be obtained from MD simulations (MD bundle). Tieleman et al.[113] simulated Alm bundles with the number N of peptides per bundle (N-bundle) varying from 4 to 8 in a POPC lipid bilayer as illustrated in Fig. 4.14. The final results are available at their website http://moose.bio.ucalgary.ca/index.php in pdb file format. We are going to use those files to calculate the form factors of Alm N-bundles assuming that the POPC lipid bilayer has

little effect on the N-bundles compared to DOPC and diC22:1PC, although, as we shall see, there can be a lipid effect on the averaged number N.

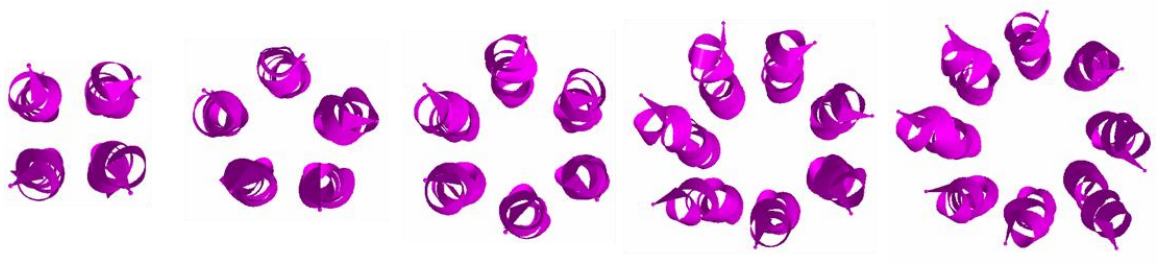

Figure 4.14: Alm bundles constructed from MD simulations.

In the solid cylindrical bundle model (solid bundle) only the average electron density contrast between the bundle and the lipid background is considered. As a result only one parameter that is related to the bundle size is involved in the form factor as shown in equation (4.11). For the MD bundles the form factor calculation is a little trickier because the atom positions from the simulations are discrete. The main idea of calculating the electron density contrast between the bundle and the lipid background based on equation (4.4) is to select two patches with the same size from a simulation snapshot. One contains every atom belonging to the bundle, including water molecules located in the central region of the bundle, and the other only contains lipid molecules. The form factor can then be calculated by the following equation

$$\begin{aligned} \mathrm{F_P}(\mathbf{q}) &= \int_P [\rho_P(\mathbf{r}) - \rho_L(\mathbf{r})] \exp[i\mathbf{q} \bullet (\mathbf{r} - \mathbf{r}_a)] dV(\mathbf{r}) \\ &= \sum_{\mathrm{m}} \mathrm{Q_m} \exp[\mathrm{i}\mathbf{q} \bullet \mathbf{r}_{\mathrm{m}}] - \sum_{\mathrm{n}} \mathrm{Q_n} \exp[\mathrm{i}\mathbf{q} \bullet \mathbf{r}_{\mathrm{n}}] \end{aligned} \quad , \qquad (4.16)$$

where $\mathbf{r}_{\mathrm{m}}$ denotes the position of the mth atom within the bundle patch with electron

number $Q_m$ and $\mathbf{r}_n$ denotes the position of the nth atom within the lipid patch with electron number $Q_n$. In practice, we chose two circular patches illustrated in Fig. 4.15, one for the bundle and the other for the lipid. The radius of the circular patch varies from 16 to 19 Å in order to include all atoms belonging to the bundle within the patch as N varies from 4 to 8. As the size of the simulation box parallel to the bilayer surface is only $62 \times 55$ Å, for large N (7 and 8), the simulation snapshot needed to be tiled to a $2 \times 2$ grid in order to obtain large enough patches. This is valid because the MD simulation itself applied periodic boundary conditions. The other issue concerning the MD bundles is the fixed orientation of the bundle in one snapshot; for our 2-D fluid like samples, the orientation of the bundle is in-plane isotropic. In order to account for this difference, a rotational average around the bilayer normal was carried out when calculating the form factor based on equation (4.16). The following equation shows how the rotational average was done.

$$F(q_r) = \left\langle \sum_k \left\{ \sum_m Q_m \exp[iq_r \times r_m \cos(\theta_m + \varphi_k)] - \sum_n Q_n \exp[iq_r \times r_n \cos(\theta_n + \varphi_k)] \right\} \right\rangle \qquad (4.17)$$

where $\theta_i$ and $r_i$ are the polar angle and the distance from the origin for the ith atom; $\varphi_k$ is a series of angles from 0 to $2\pi$ for rotational average.

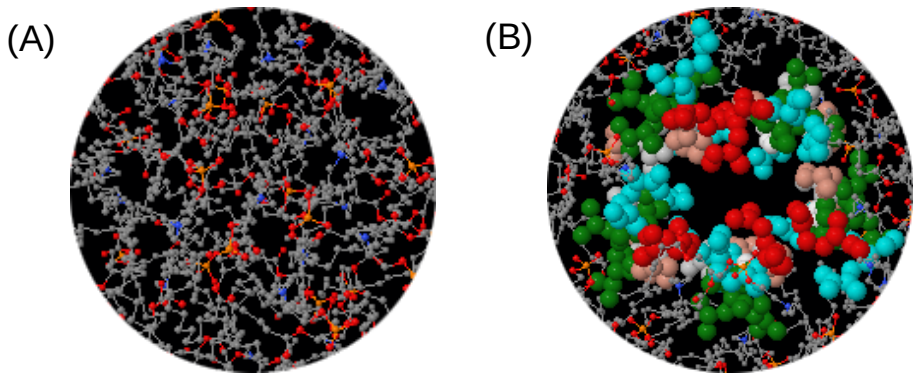


Figure 4.15: Top view of two circular patches selected for form factor calculation for the MD bundle with N=5. (A) Lipid patch, (B) Bundle patch. The hollow region in the middle of the bundle is filled with water molecules which are not shown for clarity.

The form factors along the $q_r$ direction for the MD bundles with N varying from 4 to 8 with rotational average based on equation (4.17) are shown in Fig. 4.16. From the figure we see that the main feature (nonzero value) of the form factors for the MD bundles decreases with $q_r$. When it is multiplied by the structure factor, illustrated in Fig. 4.7, whose first peak increases rapidly up to $q_r$ ~0.2Å$^{-1}$, a prominent peak is obtained at $q_r$ ~0.1Å$^{-1}$ which is about the side peak position in our experiment. If the scattering entity has a smaller size scale, a peptide monomer for example, the form factor will decay more slowly with $q_r$ and the first peak position of the structure factor will be at a much larger $q_r$ value. This results in scattering peaks at larger $q_r$ positions compared to experiment. In other words, the side peak is consistent with the current bundle model. Figure 4.16 also shows that as the number N of peptides per bundle increases, the main feature of the form factor decreases more rapidly at $q_r$ <0.2Å$^{-1}$. This trend is the same as in Fig. 4.8. It

is mainly related to the shape of the Bessel function $J_1(q_r b)/q_r$, where b is the lateral size scale of the bundle.

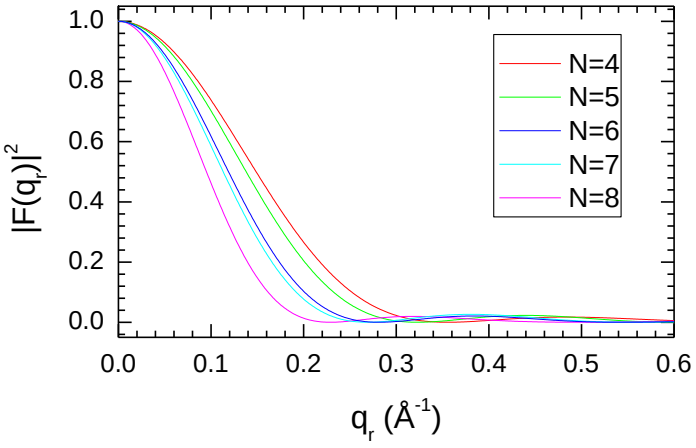


Figure 4.16: Form factors of Alm N-bundles obtained from MD simulations [113].

## 4.4.5 Model fit with form factors calculated from MD simulations

The fitting procedure of the MD bundles to the background subtracted side peaks is similar to section 4.4.3 except that this time the form factors calculated from MD simulations shown in Fig. 4.16 were used instead of approximating it with a simple cylindrical bundle. There are two fitting parameters for each model that has N peptides, the hard disk radius R and the area packing fraction η, both of which are involved in the structure factor calculation. The other fitting parameter is a scaling factor between the experimental and the theoretical scattering intensity which is the product of the structure factor and the form factor based on equation (4.5). The main fitting results are listed in Table 4.3 and the fitting curves are shown in Fig. 4.17-4.20.

Table 4.3 shows that for DOPC at both peptide concentrations, the RSS first decreases as N increases from 4 to 6 and then increases as N increases from 6 to 8, indicating that the MD bundle with N=6 fits our data best. The good fitting quality by the hexamer bundle is further confirmed by the numerical values of RSS (0.36 and 0.97 for 1:10 and 1:20 respectively) which are close to the solid bundle model fit (0.29 and 0.49) in Table 4.1. The RSS for the pentamer and the heptamer are more than two times larger.

For diC22:1PC at both peptide concentrations, the RSS decreases monotonically as N increases from 4 to 8. Because there are no MD bundles available for N>8, it is possible that N>8. Indeed the RSS for the octamer (1.39 and 2.82 for 1:10 and 1:20 respectively) are still at the large side compared to the solid bundle model (0.21 and 0.50). As the difference of the RSS between the pentamer (1.60) and the hexamer (0.36) for Alm:DOPC 1:10 is very similar to the difference between the octamer (1.39) and the best fit of the solid bundle model (0.21) for Alm:diC22:1PC 1:10 (this similarity also applies to Alm:lipid 1:20), we suggest that the nonamer fits the side peak best for diC22:1PC. Another reason for the preference of the nonamer is based on the finding that the bundle size increases by one peptide for DOPC when the MD bundle model (N=6) is applied compared to the solid bundle model (N=5). Since the solid bundle model shows that N~8 for diC22:1PC, it is reasonable to suggest that the MD bundle model will give N~9. The smaller bundle size obtained from the solid bundle model fit is related to the fact that the first peak of the form factor centered at $q_r$=0 of the solid bundle model decreases faster than the fluffy MD bundle model with the same size. In order to achieve

the same decreasing rate, which affects the position and the width of the theoretical side peak, the solid bundle model needs to shrink its outside radius and hence obtain similar decreasing rate based on Fig. 4.8 to the MD bundle model.

Table 4.3: Fitting parameters and RSS for MD bundles.

| | N=4 | N=5 | N=6 | N=7 | N=8 |
|---|---|---|---|---|---|
| Alm:DOPC 1:10 | | | | | |
| R (Å) | 24.4 | 24.1 | 23.4 | 23.1 | 22.1 |
| η | 0.43 | 0.42 | 0.42 | 0.42 | 0.44 |
| RSS | 3.61 | 1.60 | 0.36 | 0.85 | 7.08 |
| Alm:DOPC 1:20 | | | | | |
| R (Å) | 27.0 | 26.6 | 25.0 | 24.3 | 21.0 |
| η | 0.27 | 0.27 | 0.27 | 0.27 | 0.30 |
| RSS | 6.20 | 2.33 | 0.97 | 2.24 | 12.02 |
| Alm:diC22:1PC 1:10 | | | | | |
| R (Å) | 34.8 | 34.8 | 34.7 | 34.6 | 34.0 |
| η | 0.41 | 0.41 | 0.41 | 0.41 | 0.41 |
| RSS | 26.37 | 21.29 | 11.48 | 8.64 | 1.39 |
| Alm:diC22:1PC 1:20 | | | | | |
| R (Å) | 37.0 | 37.1 | 37.0 | 37.0 | 36.3 |
| η | 0.38 | 0.38 | 0.38 | 0.38 | 0.37 |
| RSS | 34.36 | 28.32 | 16.30 | 12.68 | 2.82 |

Yellow grids indicate the best fits for each data set.

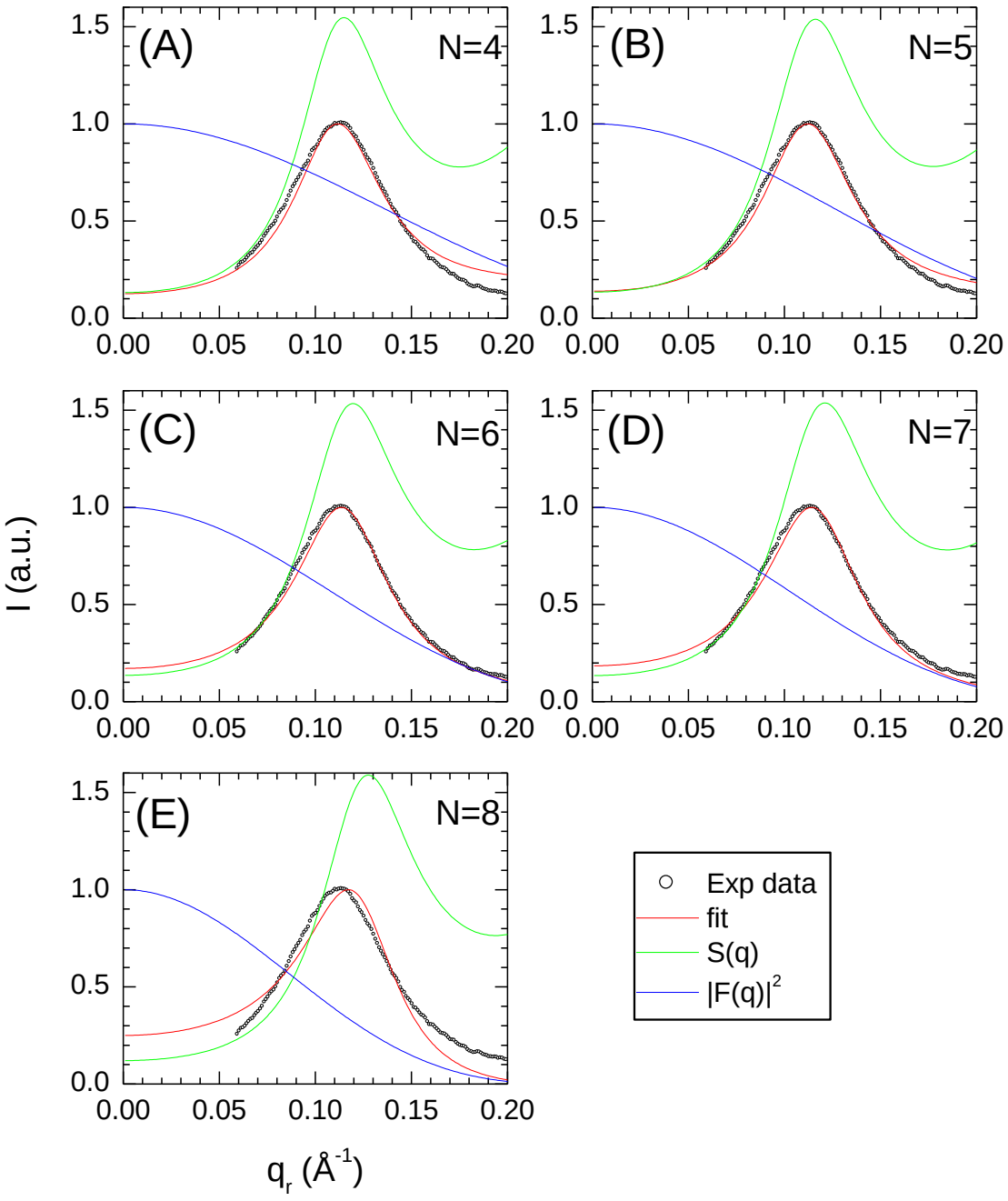


Figure 4.17: Model fits for Alm:DOPC 1:10 using form factors in Fig.4.16 calculated from MD simulations.

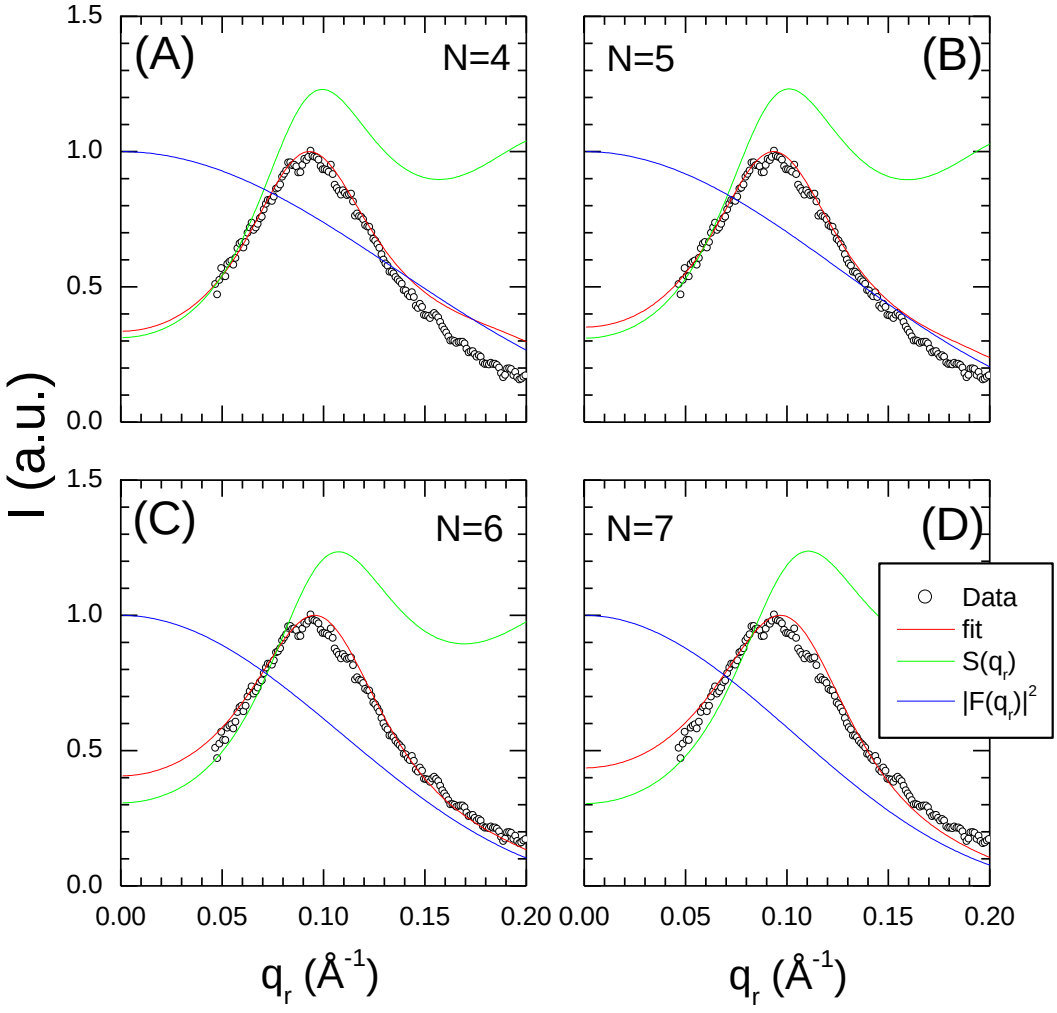


Figure 4.18: Model fits for Alm:DOPC 1:20 using form factors in Fig.4.16 calculated from MD simulations.

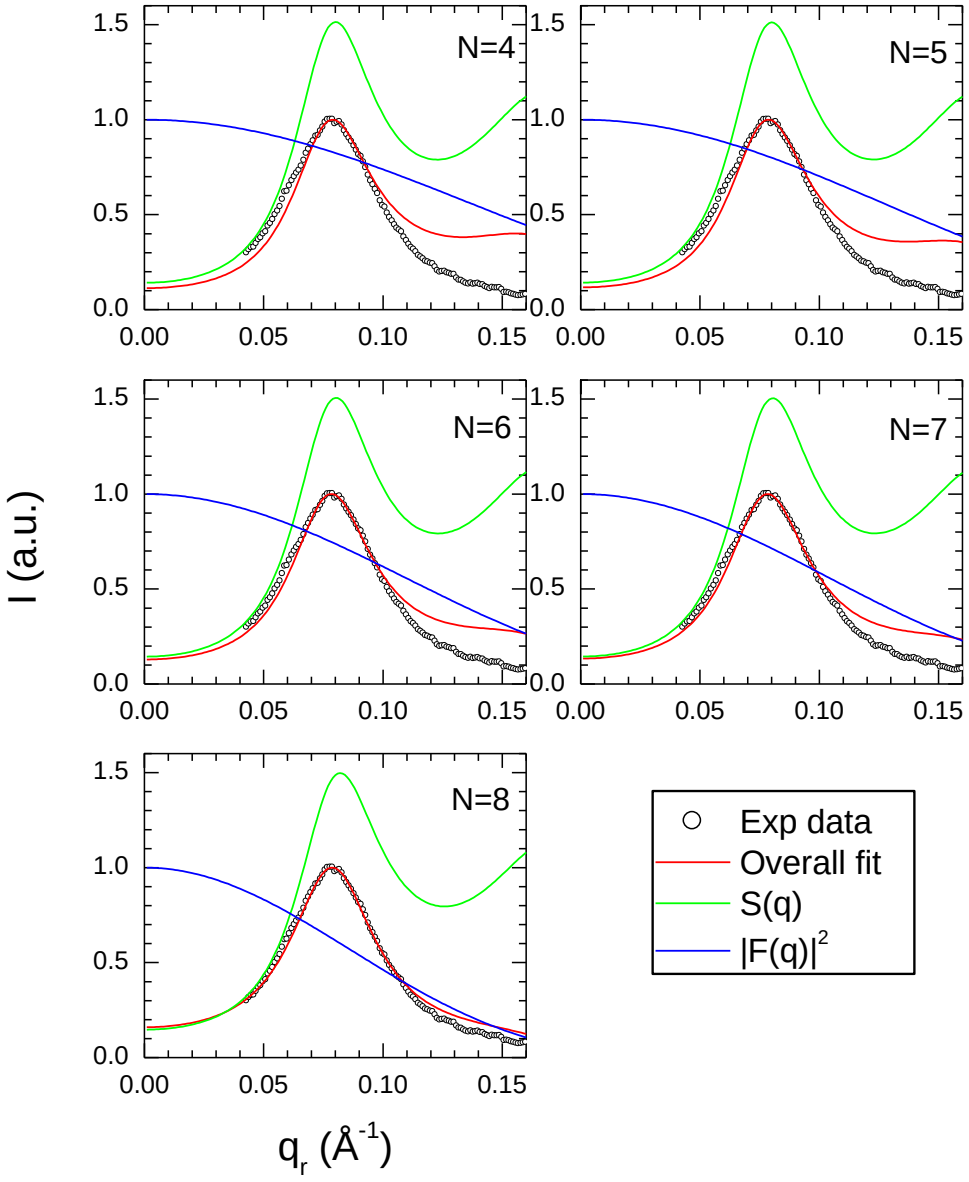


Figure 4.19: Model fits for Alm:diC22:1PC 1:10 using form factors in Fig.4.16 calculated from MD simulations.

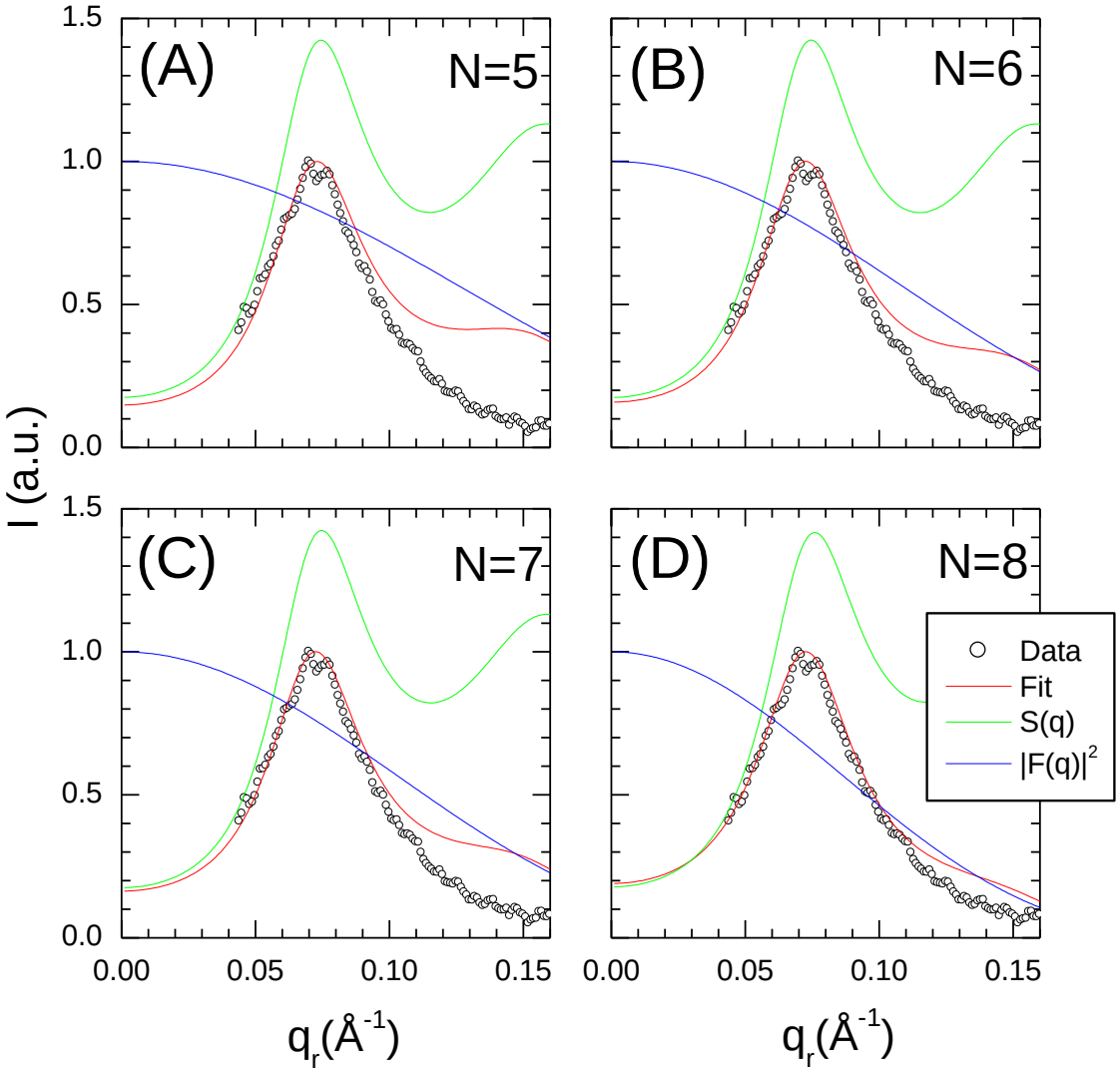


Figure 4.20: Model fits for Alm:diC22:1PC 1:20 using form factors in Fig.4.16 calculated from MD simulations.

### 4.4.6 Area packing fraction η

The area packing fraction η has been chosen to be a free parameter during the model fit in previous sections. However, it can also be estimated by using the information of the bundle size, the hard disk radius, and the peptide concentration. The lateral bundle size with different N can be estimated from the same MD simulations [113]. The detailed procedure is as following. First the coordinates of each atom belonging to the bundle are obtained from the pdb files. The 3-D (X, Y, Z) coordinates are then projected into 2-D (X, Y) (in-plane) coordinates. Next the mass center ($X_C$, $Y_C$) for all of the atoms belonging to the bundle in the (X, Y) plane is estimated. After that, the (X, Y) Cartesian coordinate is converted into a (ρ, θ) polar coordinate centered at ($X_C$, $Y_C$). The polar coordinate plane is then divided into circular sections each separated by a small degree such as $5^o$. Each atom is located in one of the circular sections. Once this is done, the atoms with the largest distance from the origin in each section are selected as the vertices outlining the perimeter of the bundle. The lateral area of the bundle $A_{bundle}$ can be approximated by the Surveyor's Formula,

$$A_{bundle} = \sum_{i=1}^{M} (X_i Y_{i+1} - X_{i+1} Y_i) \qquad (4.18)$$

where M+1 is total amount of the vertices; $X_i$ and $Y_i$ are the Cartesian coordinates of the ith vertices. The obtained lateral bundle sizes for N changing from 4 to 8 are listed in Table 4.4.

Table 4.4: Area per bundle with different number N of peptides.

| N | 4 | 5 | 6 | 7 | 8 |
|---|---|---|---|---|---|
| $A_{bundle}$ (Å$^2$) | 270 | 487 | 603 | 823 | 1052 |

The area packing fraction of the bundle can be estimated by the following equation

$$\eta = \frac{\pi R^2}{A_{bundle} + \frac{N}{2} \times \frac{L}{P} A_L} \quad , \tag{4.19}$$

where R is the hard disk radius; N is the number of peptides per bundle; L/P is lipid to peptide ratio; $A_L$ is the lateral area per lipid molecule which is 72Å$^2$ for DOPC [37, 98, 114] and 69 Å$^2$ for diC22:1PC [98]. The number 2 in the denominator is due to the fact that the bundle is transmembrane and each bilayer is formed by two lipid monolayers. The calculated area packing fractions based on equation (4.19) are listed in Table 4.5. The values are almost two times as large they are in Table 4.1 and Table 4.3. This means there is at least one incorrect assumption in equation (4.19). It can not be the hard disk radius R or the number of peptides per bundle N as they are related to the structure factor and the form factor which basically determine the position and width of the side peak. It can not be the bundle size either, because it contributes less than 35% to the denominator. The bilayer thickness measurement indicates that with the addition of 10% Alm peptide, the area per lipid changes around 10% for diC22:1PC and no change at all for DOPC [97]. This change can not be the reason for the overestimate of the area packing fraction either. The only questionable parameter is then the peptide to lipid ratio. Table 4.6 lists the required peptide to lipid ratio in order to achieve the area packing fraction in Table

4.1 and Table 4.3. As we can see all of them are smaller than the experimental ratio, which indicates that there are some peptides that are not involved in the bundle formation. This is a very interesting finding which will be discussed further in chapter 6.

Table 4.5: Area packing fraction for hard disks based on equation (4.19) using N=6 for DOPC and N=8 for diC22:1PC.

| | η |
|---|---|
| Alm:DOPC 1:10 | 0.62 |
| Alm:DOPC 1:20 | 0.40 |
| Alm:diC22:1PC 1:10 | 0.95 |
| Alm:diC22:1PC 1:20 | 0.63 |

Table 4.6: Peptide to lipid ratio calculated from equation (4.19) using the area packing fraction in Table 4.1 and Table 4.3.

| | Calculated peptide to lipid ratio |
|---|---|
| Alm:DOPC 1:10 | 1:16 |
| Alm:DOPC 1:20 | 1:31 |
| Alm:diC22:1PC 1:10 | 1:28 |
| Alm:diC22:1PC 1:20 | 1:37 |

### 4.4.7 Number of peptides per bundle N

Our best fit in Table 4.3 shows that the number of peptides per bundle N is 6 for DOPC whose hydrophobic thickness $2D_C$ is 26.8Å. For the thicker lipid bilayer, diC22:1PC, whose hydrophobic thickness $2D_C$ is 34.4Å, the best fit in Table 4.3 shows that the number of peptides per bundle $N \geq 8$. An effective hydrophobic thickness of 27-28Å for an Alm bundle was suggested by Pan et al. [97]. According to the hydrophobic matching mechanism [115, 116], when the hydrophobic thickness of the lipid molecules and the TM peptides are different, the lipid bilayer needs to deform its molecular shape in order to avoid exposure of lipid hydrocarbon chains to water solvent as illustrated in Fig. 4.21. The membrane deformation free energy per unit area [4, 5] is

$$F=(K_A/2)(\delta h/h)^2+(K_C/8)(\nabla^2 h)^2 \quad , \qquad (4.20)$$

where h is the hydrophobic thickness of the lipid bilayer, $K_C$ and $K_A$ are the bending and the area stretch modulus respectively.

When peptide molecules are distributed separately in the lipid bilayer, each peptide will perturb n surrounding lipid molecules by δh. The total number of perturbed lipid molecules decreases if the peptides aggregate together to form bundles and hence decrease the free energy of the system. This mechanism was assumed to be one of the driving forces promoting bundle formation. As the free energy is proportional to δh, the mismatch driving force is larger in the thicker bilayer diC22:1PC than in DOPC. The number of perturbed lipids keeps decreasing as the number of peptides per bundle increases until other mechanisms terminate this process such as the overexposure of

hydrophobic residues of the peptide to the inner-bundle water solvent and the decreased entropic energy of each peptide within the bundle. The final bundle size or the number N of peptides per bundle is determined by a delicate balance between the bundle formation energy and the bundle disassembling entropy. The larger bundle size in diC22:1PC is consistent with the larger bundle formation energy due to the mismatch effect.

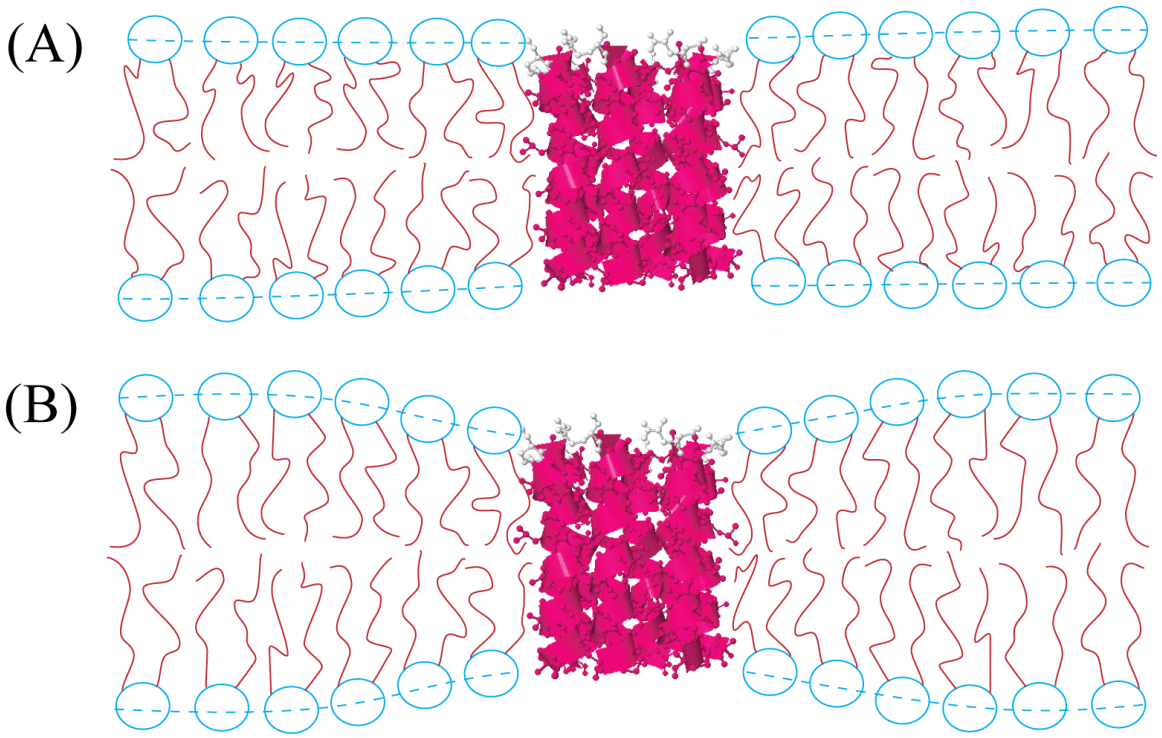


Figure 4.21: (A) Similar hydrophobic thickness between the lipid and the peptide bundle. (B) The hydrophobic thickness of the lipid is larger than the peptide bundle in which case the lipid molecules surrounding the perimeter of the peptide bundle deform their molecular shape in order to avoid exposure of hydrocarbon chains to water solvent.

To put the above argument of the bundle size as a function of the hydrophobic

mismatch δh into quantitative description, let us assume that the amount of the perturbed lipid molecules by peptide monomer or peptide bundle is proportional to their perimeter. The proportionality E(δh) depends on the mismatch based on equation (4.20). Then the mismatch energy difference per peptide between the N-bundle and the monomer state is

$$\frac{E_{bun}-E_{mon}}{N}=2\pi\, E(\delta h)\left([\,r+\frac{r}{\sin(\pi/N)}]-rN\right)/N \quad , \tag{4.21}$$

where r is the monomer radius. To derive the above equation a barrel-stave bundle structure was assumed. Another bundle promoting energy source is the interaction between the hydrophilic peptide residues with inner-bundle water solvent. Because this energy is the same for all lipids, it is ignored in the following calculation for simplicity. Based on the Sackur-Tetrode equation, the entropy of M monomers in an area A space is

$$S_{mon}=k_B\ln\left(\frac{A^M}{M!}c_0^M\right)\approx k_B\left(M-M\ln\left(\frac{M}{Ac_0}\right)\right) \tag{4.22}$$

where $c_0$ is a constant. Following the same procedure, when the M monomers form $N_B$=M/N bundles, the entropy of the $N_B$ bundles is

$$S_{bun}=k_B\left(\frac{M}{N}-\frac{M}{N}\ln\left(\frac{M}{ANc_0}\right)\right) \tag{4.23}$$

Define c=M/A, the entropy difference per peptide between the N-bundle and the monomer state is

$$\frac{S_{bun}-S_{mon}}{M}=k_B\left(\frac{N-1}{N}\left(\ln\left(\frac{c}{c_0}\right)-1\right)+\frac{1}{N}\ln(N)\right) \tag{4.24}$$

Based on equation (4.21) and (4.24), the free energy difference per peptide between the N-bundle and the monomer state is

$$\frac{F_{bun}-F_{mon}}{N\times k_B T}=\left\{\begin{array}{l}\frac{2\pi rE(\delta\ h)}{k_B T}\left([1+\frac{1}{\sin(\pi/N)}]-N\right)/N- \\ \left(\frac{N-1}{N}\left(\ln\left(\frac{c}{c_0}\right)-1\right)+\frac{1}{N}\ln(N)\right)\end{array}\right\} \tag{4.25}$$

The first term in equation (4.25) corresponds to the bundle formation energy of the hydrophobic matching and the second term corresponds to the bundle disassembling entropic free energy. The stable bundle is formed when the free energy difference in equation (4.25) reaches a local minimum at certain N value (derivative with respect to N is zero). In general equation (4.25) also needs to satisfy that the local minimum is smaller than zero; otherwise the monomer state is preferred. However, because the neglected contribution from the bundle-water interaction is normally negative (the bundle state is preferred), this condition is not that crucial.

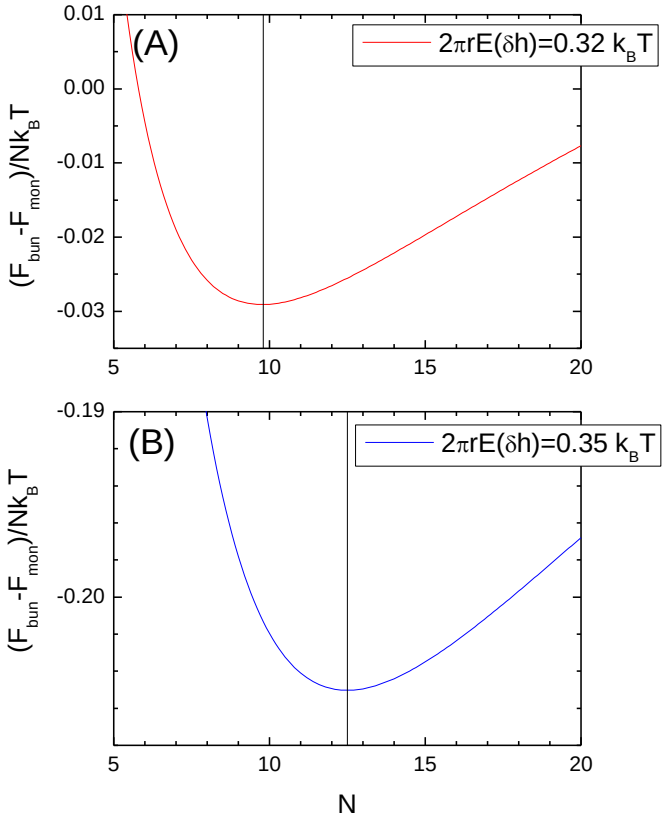


Figure 4.22: The free energy difference per peptide between the N-bundle and the monomer state as a function of N with $c/c_0$=0.28 based on equation (4.25).

Figure 4.22 illustrates an example of equation (4.25) as a function of N when the hydrophobic matching energy cost is different. As indicated by the black solid lines which indicate the position of the local minimum of equation (4.25), when the mismatch thickness increases from panel (A) to panel (B), the local minimum position shifts to larger N. This is consistent with the observed larger bundle size in diC22:1PC than in DOPC.

The current bundle formation picture is also consistent with the cholesterol effect on

the increased mean life time of the subconductance states and the single channel burst life time [117]. It has been well established that cholesterol increases the thickness and the stiffness of lipid bilayers [118, 119]. Based on equation (4.20) this increases the free energy of the monomer state and increases the driving force of bundle formation in cholesterol-rich membranes concomitant with increased mean life time of the channel state before it gets disassembled (assuming the activation energy of bundle formation does not change). Similar arguments can also be applied to the temperature induced channel stability variation [120-122].

The hydrophobic matching mechanism focuses on the lipid molecules in the vicinity of the peptide bundle. Another perspective to explain the effect of the lipid characteristic on Alm bundle size is the lateral pressure profile P(z) introduced in chapter 1, where z is the coordinate along the bilayer normal. Based on a mean-field thermodynamic theory [123], the first and the second moment of the lateral pressure profile $\int z^i P(z)dz$ along the bilayer normal decrease when the bilayer thickness increases. Simple thermodynamic calculations have shown that the probability of the largest aggregate size is inversely related to the moments of the lateral pressure profile [20]. Then the larger bundle size in diC22:1PC is also consistent with its smaller moments of the lateral pressure profile [123].

### 4.4.8 Hard disk radius R

The hard disk model was introduced for convenience in previous sections to account

for the positional correlation between the bundles embedded in a 2-D lipid bilayer. There is no rigorous physical object corresponding to the hard disk. On the other hand, it is well known that the interactions between peptide inclusions are lipid mediated [111, 112, 124-126]. Then it is reasonable to assume that the lipid molecules that are affected by a peptide/bundle inclusion, whether through hydrophobic matching [115, 127] or changes in lipid chain ordering [111, 128], buffers the interactions between the inclusions.

Following the same concept of the lipid bilayer deformation free energy, the extended lipid range $\xi$ that is affected by the peptide/bundle inclusions has been derived [5, 129]

$$\xi=(16h^2K_C/K_A)^{1/4} \quad , \tag{4.26}$$

where h, $K_A$ and $K_C$ have the same meaning as in equation (4.20). Rawicz et al. [130] showed that the area stretch modulus $K_A$ is almost the same for all of the phospholipids. The bending moduli $K_C$ for diC22:1PC and DOPC are 13 and $8\times10^{-20}$ J, respectively [37, 118, 130] and the hydrophobic thicknesses for diC22:1PC and DOPC are 34.4 and 26.8 Å, respectively [118]. The ratio of the affected lipid range by diC22:1PC and DOPC can then be calculated as $\xi(\text{diC22:1PC})/\xi(\text{DOPC})=(34.4^2\times13)^{1/4}/(26.8^2\times8)^{1/4}\approx1.3$. This value is very close to the hard disk radius ratio obtained from Table 4.1-4.3, R(diC22:1PC)/R(DOPC) ≈1.4. This similarity indicates that the larger hard disk radius in diC22:1PC is consistent with the larger range of lipid molecules that are perturbed by the embedded bundles.

## 4.5 Conclusions

By using a solid cylinder model we have shown that the height of the scattering entities which are the source of the side peaks at $q_r \sim 0.1 Å^{-1}$ is consistent with an Alm bundle. The lateral bundle size is estimated by two model fitting procedures. One approximates the bundle as a cylinder. The second model uses the form factors calculated from MD simulations. Both models applied the 2-D hard disk model in order to account for the positional correlation between the embedded bundles. The fitting results from both models indicate that the bundle size does not vary as the peptide concentration changes, and the bundle size is smaller in DOPC than in diC22:1PC. This difference is consistent with one of the bundle formation driving forces, the hydrophobic matching effect. A soft disk interaction model was also considered and similar results were obtained compared to the hard disk model.

# Chapter 5

# Crystal packing of alamethicin in lipid membranes

## 5.1 Introduction

As was shown in chapter 3, the correlation between different layers due to sample dehydration can induce 3-D structure of the scattering entities instead of 2-D in-plane structure in a single layer. The correlation can be observed by the shape of the x-ray or neutron in-plane scattering peaks. When the correlation is strong enough, a regular 3-D crystal structure of the scattering entities in the liquid crystalline samples is expected. Salditt et al. [39] reported a hexagonal packing with an AB stacking for Alm bundles in a DMPC multilayer sample by either dehydrating the stack or by lowering the temperature to the vicinity of the main phase transition. Yang et al. [38] reported a hexagonal ABC stacking for magainin and a 2-D monoclinic structure for protegrin in DMPC multilayer samples at low humidity or low temperature. A rhombohedral packing structure of Alm in brominated DSPC (di18:0PC) has also been reported recently [24]. However, all of the crystal structures mentioned above only showed a few orders in the in-plane direction. This limitation not only makes the packing structure determination ambiguous (several packing structures can fit the same set of data) but also causes the electron density construction in the in-plane direction difficult. The main effort of this chapter is to explore the transmission scattering setup similar to [85, 94] that enables us to obtain more scattering orders in the in-plane direction.

## 5.2 Structure factor of crystal packing models

A crystal is a periodic arrangement of entities in a particular pattern. Because of the periodic arrangement, the interference of waves scattered from different entities causes a distinct pattern of constructive and destructive interference to form. This is the diffraction pattern caused by crystal. In the kinematical approximation, the intensity of a diffracted beam by one type of scattering entities is given by

$$I(\mathbf{q}) = \left| \sum_j f_j \exp[i\mathbf{q} \bullet \mathbf{R}_j] \right|^2 = |F(\mathbf{q})|^2 \times S(\mathbf{q}) \quad , \tag{5.1}$$

where $\mathbf{R}_j$ is the position and $f_j$ is the scattering power of the jth scattering entity, $F(\mathbf{q})$ is the form factor related to the structure of a single scattering entity and $S(\mathbf{q})$ is the structure factor related to the positional interference between the entities which is a set of delta functions at locations that depend on the Bravais lattice. Extinction happens when the form factor is zero at locations of those delta functions.

For an infinite 3-D lattice, defined by its primitive vectors ($\mathbf{a}_1$, $\mathbf{a}_2$, $\mathbf{a}_3$), the reciprocal lattice is determined by the three reciprocal primitive vectors

$$\mathbf{b}_1 = \frac{\mathbf{a}_2 \times \mathbf{a}_3}{\mathbf{a}_1 \bullet (\mathbf{a}_2 \times \mathbf{a}_3)} \qquad \mathbf{b}_2 = \frac{\mathbf{a}_3 \times \mathbf{a}_1}{\mathbf{a}_2 \bullet (\mathbf{a}_3 \times \mathbf{a}_1)} \qquad \mathbf{b}_3 = \frac{\mathbf{a}_1 \times \mathbf{a}_2}{\mathbf{a}_3 \bullet (\mathbf{a}_1 \times \mathbf{a}_2)} \tag{5.2}$$

It can be shown that in the ideal situation, the diffraction only occurs if the scattering vector $\mathbf{q}$ is equal to a reciprocal lattice vector $\mathbf{q}$ that satisfies $\exp(i\mathbf{q}\,\mathbf{R})=1$ for all lattice

point positions **R**. This is equivalent to saying that the scattering only occurs at $\mathbf{q} = 2\pi(\mathrm{H}\mathbf{b}_1 + \mathrm{K}\mathbf{b}_2 + \mathrm{L}\mathbf{b}_3)$, also known as the Laue equation [131], where H, K, and L are the Miller indices (integer numbers). Then the structure factor S(**q**) can be expressed as

$$\mathrm{S}(\mathbf{q}) = \left| \sum_{\mathrm{k}=1}^{\mathrm{N}} \exp[-2\pi\, i(\mathrm{H}\mathbf{b}_1 + \mathrm{K}\mathbf{b}_2 + \mathrm{L}\mathbf{b}_3) \bullet \mathbf{R}_\mathrm{k}] \right|^2 \tag{5.3}$$

where N is the number of bases in one unit cell and $\mathbf{R}_\mathrm{k}$ is the position of the kth basis in the unit cell. In the following subsections we will show some examples of the structure factors for some of the most common crystal packing models that occur in oriented multilayer samples.

## 5.2.1 Hexagonal packing models

Figure 5.1 shows three models based on hexagonal packing. They have two length scales, a and c. This series of packing models can be described by the (reciprocal) primitive vectors

$$\mathbf{a}_1 = [\frac{a}{2}, \frac{a\sqrt{3}}{2}, 0] \quad \mathbf{a}_2 = [-\frac{a}{2}, \frac{a\sqrt{3}}{2}, 0] \quad \mathbf{a}_3 = [0, 0, c]$$

$$\mathbf{b}_1 = [\frac{1}{a}, \frac{1}{a\sqrt{3}}, 0] \quad \mathbf{b}_2 = [-\frac{1}{a}, \frac{1}{a\sqrt{3}}, 0] \quad \mathbf{b}_3 = [0, 0, \frac{1}{c}] \tag{5.4}$$

The only difference is the number and positions of the bases in one unit cell. For the simple hexagonal packing, the basis is $\mathbf{R}_1 = [0, 0, 0]$; for the AB stacking packing, the

bases are $\mathbf{R}_1 = [0, 0, 0]$ and $\mathbf{R}_2 = [0, \frac{a}{\sqrt{3}}, \frac{c}{2}]$; for the ABC stacking packing, the bases are $\mathbf{R}_1 = [0, 0, 0], \mathbf{R}_2 = [0, \frac{a}{\sqrt{3}}, \frac{c}{3}]$, and $\mathbf{R}_3 = [0, \frac{2a}{\sqrt{3}}, \frac{2c}{3}]$.

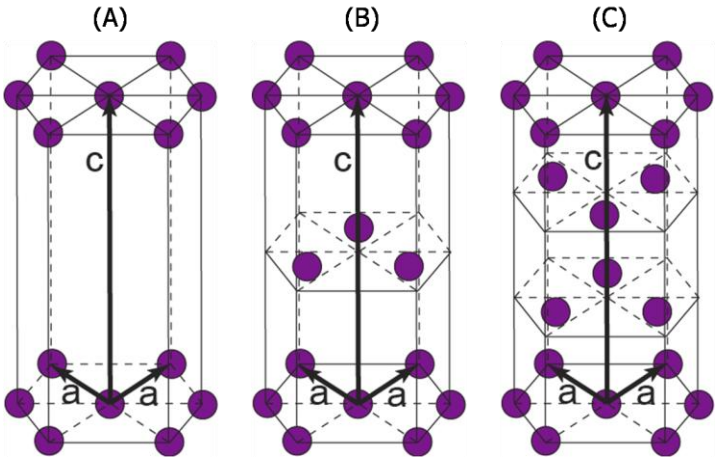


Figure 5.1: Illustrations of the packing models for (A) simple hexagonal, (B) hexagonal AB stacking, (C) hexagonal ABC stacking. The primitive vectors are indicated by the arrow lines.

Based on equation (5.3), for any set of Miller indices, the structure factor of the simple hexagonal packing is

$$S_{\text{simplehexagonal}}(\mathbf{q}) = \left| \sum_{k=1}^{1} \exp\left[-2\pi i\left(H\mathbf{b}_1 + K\mathbf{b}_2 + L\mathbf{b}_3\right) \bullet \mathbf{R}_k\right] \right|^2 = 1 \qquad (5.5)$$

This means the structure factor is nonzero at any set of [H,K,L]. For the hexagonal AB stacking, the structure factor is

$$S_{\text{AB hexagonal}}(\mathbf{q}) = \left| \sum_{k=1}^{2} \exp\left[-2\pi i\left(H\mathbf{b}_1 + K\mathbf{b}_2 + L\mathbf{b}_3\right) \bullet \mathbf{R}_k\right] \right|^2$$

$$= \left| 1 + \exp\left[ -2\pi i \left[ \frac{H-K}{a}, \frac{H+K}{a\sqrt{3}}, \frac{L}{c} \right] \bullet \left[ 0, \frac{a}{\sqrt{3}}, \frac{c}{2} \right] \right] \right|^2$$

$$= \left| 1 + \exp\left[ -2\pi i \left( \frac{H+K}{3} + \frac{L}{2} \right) \right] \right|^2 \qquad (5.6)$$

The structure factor is zero when 2(H+K)/3+L=(2n+1) where n is integer. Following the same procedure, the structure factor of the hexagonal ABC stacking is

$$S_{ABC\,hexagonal}(\mathbf{q}) = \left| \sum_{k=1}^{3} \exp\left[ -2\pi i \left( H\mathbf{b}_1 + K\mathbf{b}_2 + L\mathbf{b}_3 \right) \bullet \mathbf{R}_k \right] \right|^2$$

$$= \left| 1 + \exp\left[ -2\pi i \left( \frac{H+K+L}{3} \right) \right] + \exp\left[ -2\pi i \left( \frac{2H+2K+2L}{3} \right) \right] \right|^2 \qquad (5.7)$$

The structure factor is zero when H+K+L≠3n. Figure 5.2 shows the structure factors of the three models with a=43 Å and c=86 Å. One may notice that the abscissa is $q_r=(q_x+q_y)^{1/2}$, not $q_x$ or $q_y$. This is due to the fact that we considered a rotational average along the $\mathbf{a}_3$ axis for each case in order to relate these models to our 2-D fluid like powder averaged samples in each layer. An interesting feature in Fig. 5.2 is that the more layers along the $\mathbf{a}_3$ axis there are in one unit cell, the fewer peaks one gets in reciprocal space. This is consistent with the conditions at which the structure factor becomes zero.

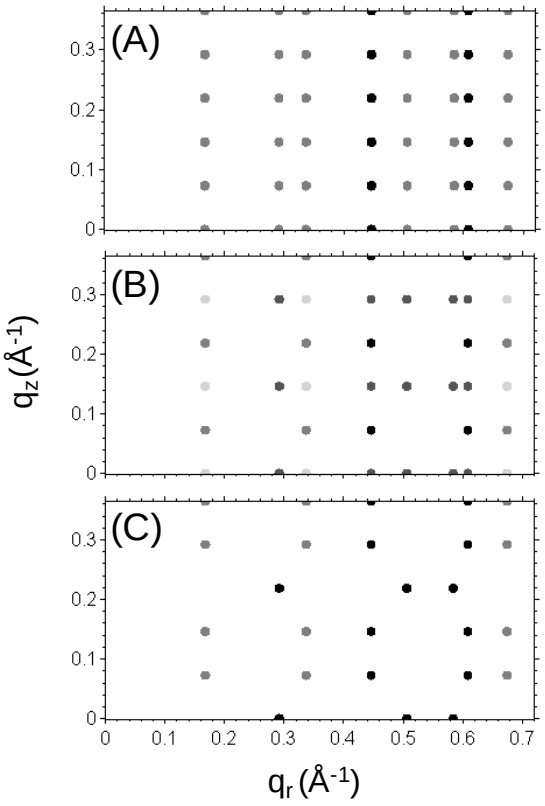


Figure 5.2: Structure factors for (A) simple hexagonal, (B) hexagonal AB stacking, and (C) hexagonal on ABC stacking models with a=43 Å and c=86 Å. The color scale indicates a larger structure factor for a darker point.

## 5.2.2 Tetragonal packing models

The tetragonal packing models are shown in Fig. 5.3. They also have two length scales, a and c. Similar to the hexagonal models, the two tetragonal models can be described by the following (reciprocal) primitive vectors

$\mathbf{a}_1 = [a, 0, 0]$ $\mathbf{a}_2 = [0, a, 0]$ $\mathbf{a}_3 = [0, 0, c]$

$$\mathbf{b}_1 = [\frac{1}{a}, 0, 0] \qquad \mathbf{b}_2 = [0, \frac{1}{a}, 0] \qquad \mathbf{b}_3 = [0, 0, \frac{1}{c}] \tag{5.8}$$

For the simple tetragonal packing, the basis is $\mathbf{r}_1 = [0, 0, 0]$ and for the body centered tetragonal (BCT) packing the bases are $\mathbf{R}_1 = [0, 0, 0]$ and $\mathbf{R}_2 = [a/2, a/2, c/2]$.

The structure factor of the simple tetragonal is S(**q**)=1 which means the structure factor is nonzero at any set of Miller indices and the structure factor of the body centered tetragonal is $S(\mathbf{q})=|1+\exp[-\pi i(H+K+L)]|^2$ which means the structure factor is zero when H+K+L=2n+1. Figure 5.4 shows the structure factors of the two tetragonal models with a=37 and c=86Å. From the figure we see that the body centered tetragonal packing has fewer peaks than the simple tetragonal packing.

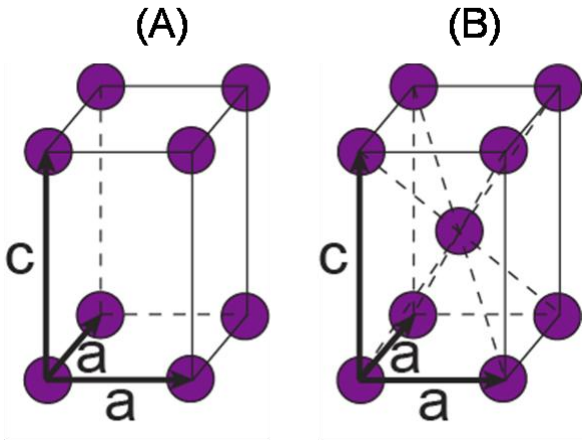


Figure 5.3: Illustrations of the crystal packing models for (A) simple tetragonal, (B) body centered tetragonal.

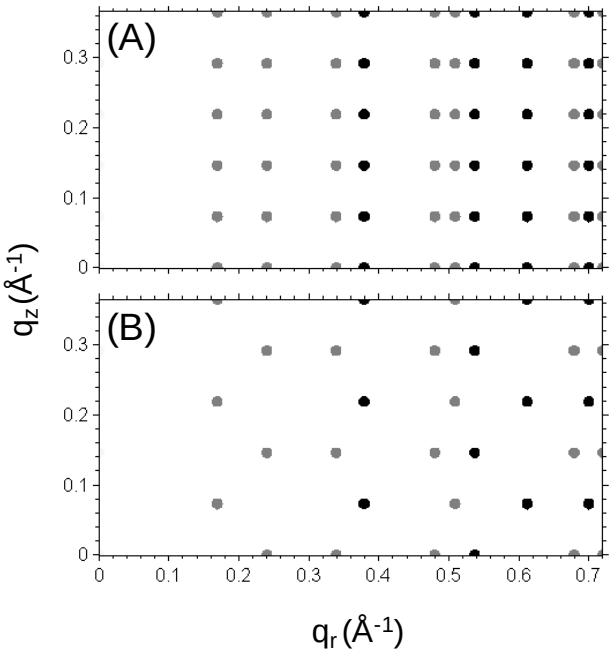


Figure 5.4: Structure factors for (A) simple tetragonal and (B) body centered tetragonal packing models with a=37Å and c=86Å. The color scale is the same as in Fig. 5.2.

## 5.3 Transmission scattering experiment

As has been shown in chapter 3, the grazing incident low angle x-ray scattering experiment has the limitation that the sample holder blocks part of the scattered beam at $q_z$ near zero in addition to the sample absorption effect. One solution is to place the substrate before (or after) the sample itself as shown in Fig. 5.5 [85]. Unlike the grazing incident experiment, where the scattered wave vector $\mathbf{q} = 4\pi\sin(\theta)/\lambda$ in the CCD frame is nearly the scattered wave vector in the sample frame (small angle approximation), there are extra works need to be done in order to convert the CCD frame to the sample frame. The following derivation was based on the equations obtained by

Gil Toombes and Thalia T. Mills.

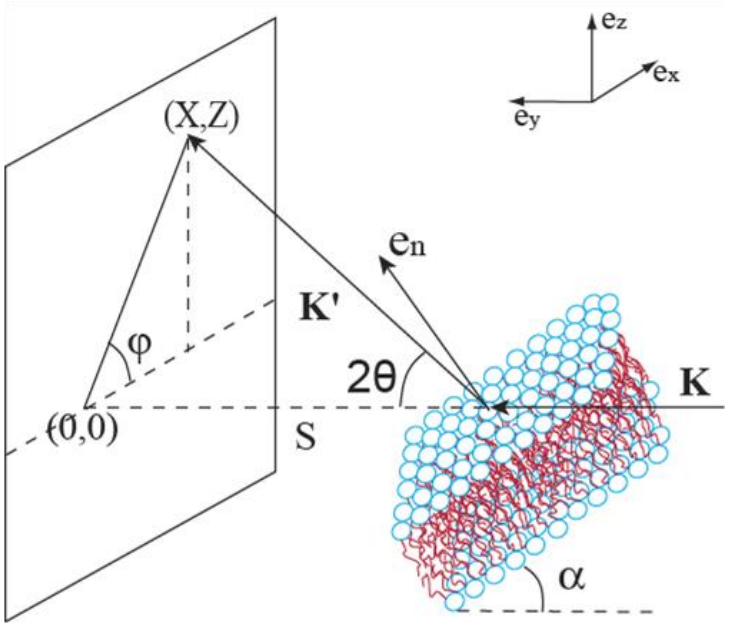


Figure 5.5: Transmission scattering experiment setup. **K** is the wave vector of the incident beam; **K'** is the wave vector of the scattered beam; 2θ is the angle between the scattered and incident beam commonly referred to as the Bragg scattering angle; α is the tilt angle of the sample about the x axis relative to the x-y plane; $\mathbf{e}_n$ is the unit vector along the sample normal; the beam position is taken to be the origin for simplicity in the CCD frame; (X,Z) is the position of the scattered beam on the CCD detector; φ is the angle between (X,Z) and the +X axis; S is the distance between the sample and the detector.

From the collected CCD image, we have the Cartesian coordinate of the scattered beam (X, Y). We also know the sample to detector distance S by using the standard, silver behenate. First we express θ and φ in Fig. 5.5 as

$$\tan(2\theta) = \frac{\sqrt{X^2 + Z^2}}{S} \quad , \qquad \tan(\varphi) = \frac{Z}{X} \tag{5.9}$$

The wave vector of the incident beam **K** and the scattered beam **K'** are

$$\mathbf{K} = \frac{2\pi}{\lambda}\mathbf{e}_y$$
$$\mathbf{K}' = \frac{2\pi}{\lambda}[\sin(2\theta)\cos(\varphi)\mathbf{e}_x + \cos(2\theta)\mathbf{e}_y + \sin(2\theta)\sin(\varphi)\mathbf{e}_z]$$

(5.10)

By definition we have the scattered wave vector **q** as:

$$\mathbf{q} = \mathbf{K}' - \mathbf{K} = \frac{2\pi}{\lambda}[\sin(2\theta)\cos(\varphi)\mathbf{e}_x + (\cos(2\theta) - 1)\mathbf{e}_y + \sin(2\theta)\sin(\varphi)\mathbf{e}_z] \tag{5.11}$$

Using $\sin(2\theta) = 2\sin(\theta)\cos(\theta)$ and $\cos(2\theta) = 1 - 2\sin^2(\theta)$ we get:

$$\mathbf{q} = \frac{4\pi\sin(\theta)}{\lambda}[\cos(\theta)\cos(\varphi)\mathbf{e}_x - \sin(\theta)\mathbf{e}_y + \cos(\theta)\sin(\varphi)\mathbf{e}_z] \tag{5.12}$$

From Fig.5.5, it is easy to see that the sample normal is $\mathbf{e}_n = \sin(\alpha)\mathbf{e}_y + \cos(\alpha)\mathbf{e}_z$. Then the projections of the scattered wave vector **q** into the $q_z$ along sample normal and the $q_r$ parallel to the sample surface are

$$\left\{\begin{aligned} q_z &= \mathbf{q} \bullet \mathbf{e}_n \\ &= \frac{4\pi\sin(\theta)}{\lambda}[\cos(\theta)\cos(\varphi)\mathbf{e}_x - \sin(\theta)\mathbf{e}_y + \cos(\theta)\sin(\varphi)\mathbf{e}_z] \bullet (\sin(\alpha)\mathbf{e}_y + \cos(\alpha)\mathbf{e}_z) \\ &= \frac{4\pi\sin(\theta)}{\lambda}[\cos(\theta)\sin(\varphi)\cos(\alpha) - \sin(\theta)\sin(\alpha)] \\ q_r &= \sqrt{|q|^2 - q_z^2} \\ &= \frac{4\pi\sin(\theta)}{\lambda}\sqrt{1 - (\cos(\theta)\sin(\varphi)\cos(\alpha) - \sin(\theta)\sin(\alpha))^2} \end{aligned}\right\} \tag{5.13}$$

In order to obtain the scattering intensity at any pair of ($q_r$, $q_z$) in reciprocal space, we need to reverse the process from equation (5.9) to (5.13). In another word, we need to represent every pair of ($q_r$, $q_z$) into some specific CCD Cartesian coordinate pair (X, Z)

which has a known intensity I(X, Z). By using equation (5.12) and equation (5.13), we have

$$\left\{\begin{array}{l}\sin(\theta)=\dfrac{\lambda\sqrt{q_r{}^2+q_z{}^2}}{4\pi}\\ \sin(\varphi)=\left[\dfrac{\lambda q_z}{4\pi\sin(\theta)}+\sin(\theta)\sin(\alpha)\right]\times\dfrac{1}{\cos(\theta)\cos(\alpha)}\end{array}\right\} \tag{5.14}$$

From equation (5.9) we have:

$$X=S\tan(2\theta)\cos(\varphi) \qquad Z=S\tan(2\theta)\sin(\varphi) \tag{5.15}$$

Equation (5.14) and (5.15) establish the correspondence between the pair of (X, Z) and the pair of ($q_r$, $q_z$). In this way we can calculate the reciprocal space image in the sample frame based on the known intensity distribution in the CCD frame.

Figure 5.6 shows how the reciprocal space images look in the sample frame at three different sample rotation angles α. In Fig. 5.6A, the sample normal is parallel to $\mathbf{e}_z$, α=0. According to equation (5.13), $q_z=|\mathbf{q}|\cos(\theta)\sin(\varphi)$ and $q_r=|\mathbf{q}|(1-\cos^2(\theta)\sin^2(\varphi))^{1/2}$. As cos(θ)sin(φ) can be any value between -1 and 1, each pair of ($q_r$, $q_z$) has a corresponding θ, φ and |**q**|. It is equivalent to say that each pair of ($q_r$, $q_z$) has a corresponding pair of (X, Z) in the CCD frame. In Fig. 5.6B, the sample normal is parallel to $\mathbf{e}_y$, $\alpha=90^o$. In this case $q_z=-|\mathbf{q}|\sin(\theta)$ and $q_r=|\mathbf{q}|\cos(\theta)$ according to equation (5.13). They define a curved line in the q space. Any other pair of ($q_r$, $q_z$) is not available. When α is some value between $0^o$ and $90^o$, the situation is somewhat between the above two extreme cases as shown in Fig. 5.6C. There are two triangular regions that are not available in reciprocal space in the sample frame as indicated by the white regions. One interesting feature is that the larger

the sample rotation angle α is, the larger the unavailable reciprocal space is in the sample frame.

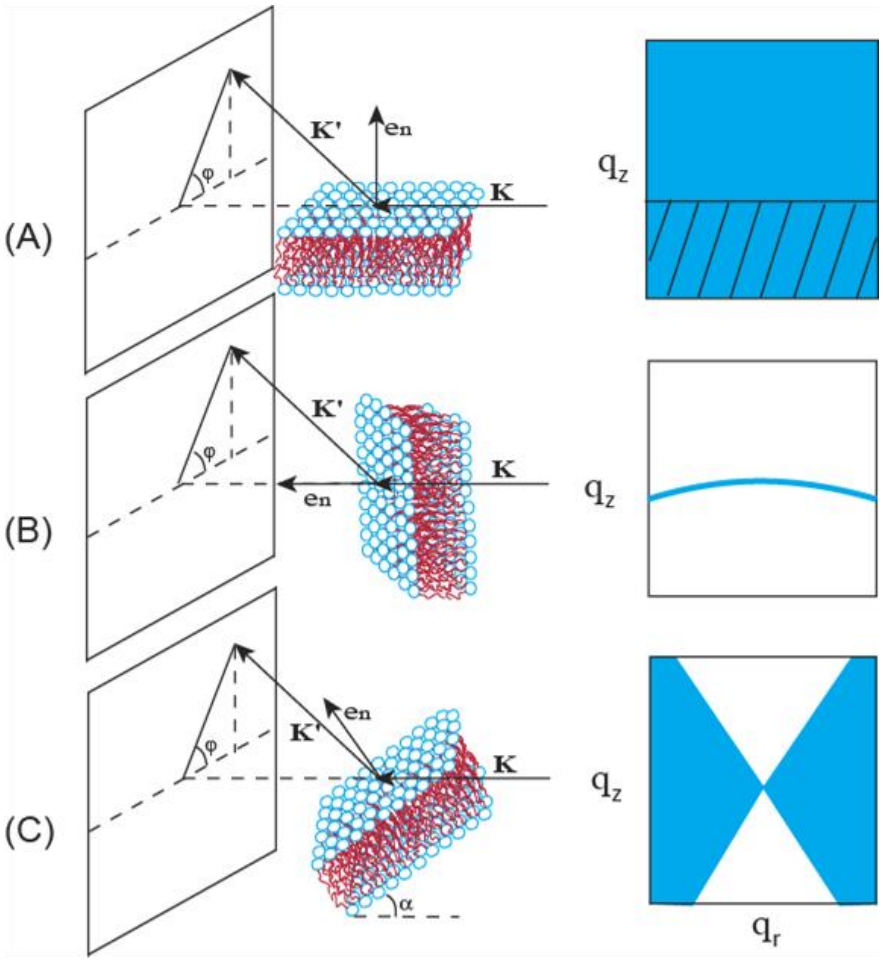


Figure 5.6: Examples of reciprocal space images at three rotation angles α (A) $0^o$ (the tilted lines indicate the region cut off by the substrate), (B) $90^o$, and (C) Between $0^o$ and $90^o$. The blue regions on the right side indicate the available reciprocal space in the sample frame.

## 5.4 Crystal scattering patterns of Alm:DOPC 1:10

The sample we investigated by using the transmission scattering experimental setup

is Alm:DOPC 1:10. The substrate is a silicon wafer with thickness 35μm which is small compared with the attenuation length 150μm (http://www-cxro.lbl.gov/). This means the incident x-ray beam is not attenuated much by the substrate. Figure 5.7A shows an example of the CCD image for the sample at a lamellar repeat spacing D=42Å with sample rotation angle $\alpha=30^{o}$. Figure 5.7B shows the reciprocal space image in the sample frame by applying equation (5.14) and (5.15). The two red triangular regions show the unavailable reciprocal space due to the sample rotation.

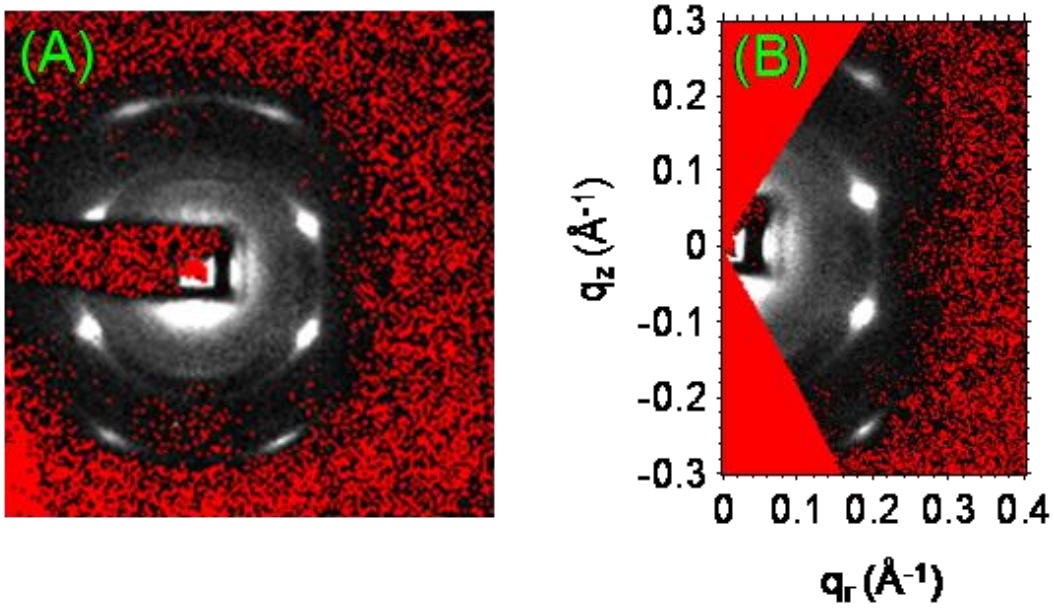


Figure 5.7: (A) CCD frame image for Alm:DOPC 1:10 (D=42Å) with the sample rotation angle $\alpha=30^{o}$. The finger shaped region is a piece of molybdenum attenuator used to attenuate the incident beam which is shown by the white region behind the right side of the finger. (B) Reciprocal space image in the sample frame at $q_r>0$ converted from the CCD image (A). The red pixels indicate the smallest intensity.

The scattering pattern in Fig. 5.7B is very similar to the scattering pattern for Alm in a DMPC multilayer sample [39]. The authors claimed that the packing structure is hexagonal AB stacking. However, by comparing Fig. 5.7B to Fig. 5.2B and Fig. 5.4B, we see that both the hexagonal AB stacking and the body centered tetragonal packing fit the observed scattering pattern equally well (assuming the weak peaks at L=0 and L=2 for the hexagonal AB stacking in Fig. 5.2B are extinct). This ambiguity is caused by the lack of extra orders at larger $q_r$ value which is mainly due to the thermal fluctuations and the form factor of the scattering entity.

## 5.5 Hexagonal and tetragonal models

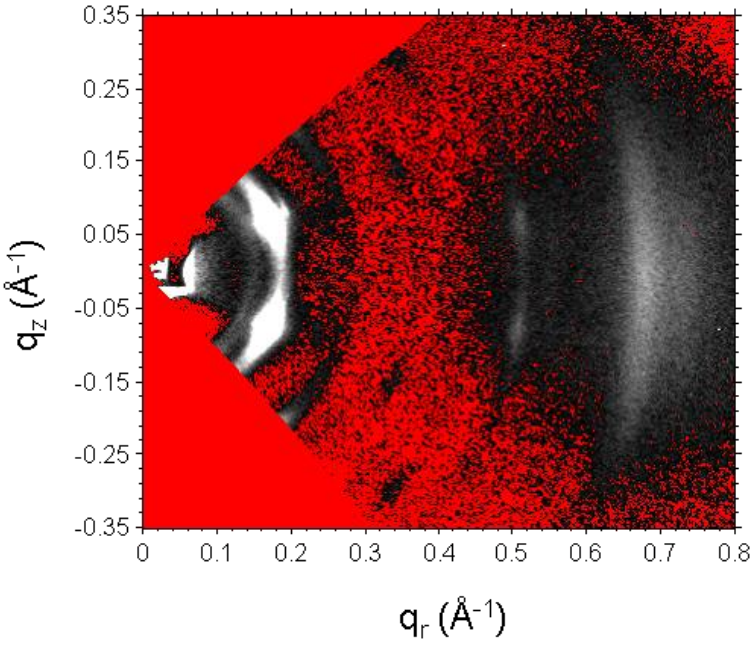


Figure 5.8: Experimental data for Alm:DOPC 1:10 (D=43Å) with sample rotation angle $\alpha=45^{o}$.

Figure 5.8 shows a better scattering pattern for Alm:DOPC 1:10 (D=43Å) with sample rotation angle $\alpha=45^{o}$ in the sense that it has more scattering peaks. The numerical values of the peak positions in Fig. 5.7B and Fig. 5.8 are listed in Table 5.1 and 5.2. The peak positions are averaged over the pair at the opposite $q_z$ value. The difference of the peak I position in Table 5.1 and 5.2 is due to the slightly different hydration level.

Table 5.1 Experimental peak positions in Fig. 5.8 at $q_z \geq 0$.

| | Exp $q_r$ ($Å^{-1}$) | Exp $q_z$ ($Å^{-1}$) |
|---|---|---|
| peak I | 0.173 | 0.069 |
| peak II | 0.340 | 0.143 |
| peak III | 0.338 | 0.299 |
| peak IV | 0.510 | 0.070 |
| peak V | 0.680 | 0.00 |

Table 5.2 Experimental peak positions in Fig. 5.7B at $q_z \geq 0$.

| | Exp $q_r$ ($Å^{-1}$) | Exp $q_z$ ($Å^{-1}$) |
|---|---|---|
| peak I | 0.186 | 0.078 |
| peak VI | 0.190 | 0.231 |

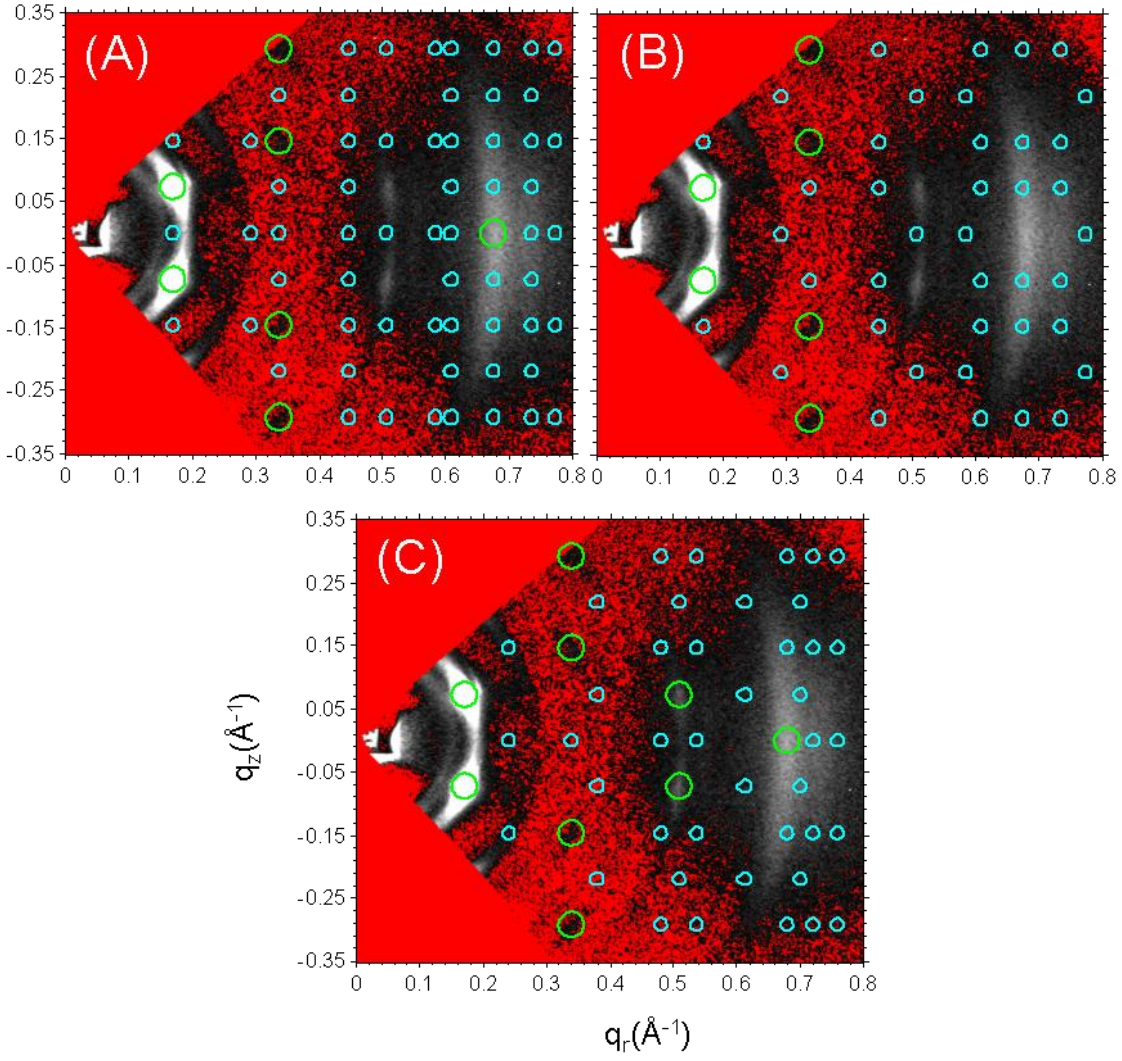


Figure 5.9: Composites of experimental peaks in Fig. 5.8 and (A) hexagonal AB stacking (a=43 Å and c=86Å), (B) hexagonal ABC stacking (a=43 Å and c=86Å), and (C) body centered tetragonal packing (a=37 Å and c=86Å). The large green circles indicate the predictions from the models that are observed in the experiment while the small cyan circles indicate the predictions from the models that are not observed in the data.

Figure 5.9 shows the composite of the experimental peaks in Fig. 5.8 and the

predictions from the hexagonal AB stacking (a=43 Å and c=86 Å), the hexagonal ABC stacking (a=43 Å and c=86 Å) and the body centered tetragonal packing (a=37 Å and c=86 Å) models respectively. The green circles indicate the match between the models and the data and the cyan circles indicate peaks predicted by the models but missing in the data. In Fig. 5.9A and B the observed peaks at ($q_r$, $q_z$)=(0.17, ±0.07) and (0.34, ±0.14) are well predicted by the hexagonal AB and ABC stacking models, while the peaks at ($q_r$, $q_z$)=(0.51, ±0.07) are not predicted by these two models. This inconsistency indicates that the real packing model can not be the hexagonal AB or ABC stacking. On the other hand, as shown in Fig. 5.9C, all of the observed peaks are well predicted by the body centered tetragonal packing model. However there are many peaks by the model that are not observed in the data. The [H, K] Miller indices for the peaks in each column in Fig. 5.9A, B and Fig. 5.9C are listed in Table 5.3 and 5.4 respectively.

An interesting peak in Fig. 5.9 is peak V centered at ($q_r$, $q_z$)=(0.68, 0) with a very broad tail in the $q_z$ direction. It can be well fit by the [H, K, L]=[4,0,0] peak in the body centered tetragonal model. However the tail of that peak can not be from the mosaicity of the sample because the rest of the peaks have a much narrower distribution in the $q_z$ direction. In fact, the peak looks more like a Bragg rod caused by 2-D in-plane distributed scattering entities, different from the source for the rest of the peaks. The possibility of the coexistence of two types of scattering entities will be discussed further in the following chapters. Another explanation for the wide $q_z$ distribution of the peak centered at ($q_r$, $q_z$) =(0.68, 0) is that it is a combination of the three peaks, [4,0,2], [4,0,0]

and [4,0,-2], in the body centered tetragonal model. By examining the 2 peaks at the sixth column ($q_r$~0.51Å$^{-1}$) in Fig. 5.9 we see that they have fairly broad tails along the $q_z$ direction. If there is another peak centered at the equator at that $q_r$ value, the combination of the three peaks at the sixth column will look similar to the broad peak at the ninth column centered at ($q_r$, $q_z$) =(0.68, 0).

The diffuse scattering at $q_r$>0.68 Å$^{-1}$ is another complication of the scattering pattern in Fig. 5.9. It is too broad to be a Bragg peak. One explanation is that if the two peaks, [3,3,0] and [4,2,0] which are located at $q_r$=0.72 and 0.76 Å$^{-1}$ respectively in the body centered tetragonal model, have similar peak widths as [4,0,0] at $q_r$=0.68 Å$^{-1}$ in the $q_r$ direction with weaker intensities, the combination of them will look similar to the diffuse scattering in Fig. 5.9.

Table 5.3 Miller indices for hexagonal AB and ABC stacking models in Fig.5.9A and B.

| column | 1st | 2nd | 3rd | 4th | 5th | 6th | 7th | 8th |
|---|---|---|---|---|---|---|---|---|
| $q_r/2\pi a$ | $(4/3)^{1/2}$ | 2 | $(16/3)^{1/2}$ | $(28/3)^{1/2}$ | $(12)^{1/2}$ | 4 | $(52/3)^{1/2}$ | $(64/3)^{1/2}$ |
| [H,K] | ±1, ±1<br>±1,0<br>0, ±1 | ±2, ±1<br>±1, ±2<br>±1, ∓1 | ±2, ±2<br>±2,0<br>0, ±2 | ±3, ±2<br>±3, ±1<br>±2, ±3<br>±2, ∓1<br>±1, ±3<br>±1,-+2 | ±3, ±3<br>±3,0<br>0, ±3 | ±4, ±2<br>±2, ±4<br>±2, ∓2 | ±4, ±3<br>±4, ±1<br>±3, ±4<br>±3, ∓1<br>±1, ±4<br>±1, ∓3 | ±4, ±4<br>±4,0<br>0, ±4 |
| observed peaks (AB) | I (L=1)<br>VI(L=3) | None | II (L=2)<br>III (L=4) | None | IV(L=1) | None | None | V(L=0) |
| observed peaks (ABC) | I (L=1)<br>VI(L=3) | None | II (L=2)<br>III (L=4) | None | IV(L=1) | None | None | V(L=0) |

Note: Red indicates the peaks that are observed in the experiment but missing in the model. The structure factor is zero when 2(H+K)/3+L=2n+1 for the hexagonal AB stacking and H+K+L≠3n for the hexagonal ABC stacking.

Table 5.4 Miller indices [H, K] for body centered tetragonal model in Fig. 5.9C.

| column | 1st | 2nd | 3rd | 4th | 5th | 6th | 7th | 8th | 9th |
|---|---|---|---|---|---|---|---|---|---|
| $q_r/2\pi a$ | 1 | $2^{1/2}$ | 2 | $5^{1/2}$ | $8^{1/2}$ | 3 | $10^{1/2}$ | $13^{1/2}$ | 4 |
| [H,K] | ±1, 0<br>0, ±1 | ±1, ±1<br>±1, ∓1 | ±2, 0<br>0, ±2 | ±2, ±1<br>±2, ∓1<br>±1, ±2<br>±1, ∓2 | ±2, ±2<br>±2, ∓2 | ±3,0<br>0, ±3 | ±3, ±1<br>±3, ∓1<br>±1, ±3<br>±1, ∓3 | ±3, ±2<br>±3, ∓2<br>±2, ±3<br>±2, ∓3 | ±4,0<br>0, ±4 |
| observed peaks | I (L=1)<br>VI(L=3) | None | II (L=2)<br>III (L=4) | None | None | IV(L=1) | None | None | V(L=0) |

Note: The structure factor is zero when H+K+L=2n+1 for body centered tetragonal model.

## 5.6 Monoclinic models

Let us consider another crystal packing structure, the 2-D monoclinic structure illustrated in Fig. 5.10A. The ripple phase of pure lipids has been shown to form this structure [132, 133] and it has been invoked to interpret the scattering of the protegrin peptide in DMPC multilayer samples [38]. The (reciprocal) primitive vectors are

$$\begin{aligned} a_1 &= [a, 0] & a_2 &= [c\cos(\alpha), c\sin(\alpha)] \\ b_1 &= [\frac{1}{a}, -\frac{\cot(\alpha)}{a}] & b_2 &= [0, \frac{1}{c\sin(\alpha)}] \end{aligned} \quad , \qquad (5.16)$$

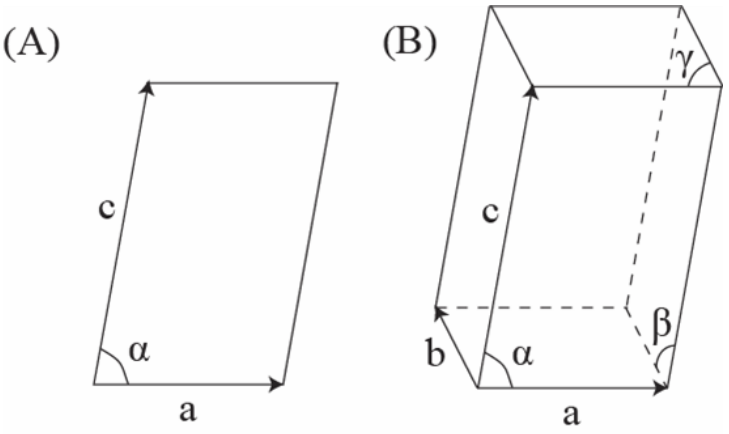


Figure 5.10: (A) 2-D monoclinic and (B) 3-D monoclinic packing models. $\alpha \neq 90^o$, $\beta=\gamma=90^o$.

Figure 5.11 compares the experimental data to the theoretical peaks of the 2-D monoclinic structure with a=37 Å, c=46.8 Å and $\alpha=66.8^o$. The model fits the experimental peaks very well. There are fewer extinct peaks compared to the body centered tetragonal model in Fig. 5.9C. The only extinct one at low $q_z$ in the 2-D monoclinic model is the [H, L]=[2, -1]=(0.34, 0) which will be discussed later. By examining Table 5.2 we see that the $q_z$ value of peak VI is about 3 times as large as peak I. This is an intrinsic requirement for the body centered tetragonal packing model. However, it is not necessary for the 2-D monoclinic structure. It is more like a coincidence for the 2-D monoclinic packing model due to its packing parameters. For the peak at $(q_r, q_z)=(0.68, 0)$ with large $q_z$ distribution, similar arguments for the body centered tetragonal model can be applied here. However, the diffuse like scattering at $q_r>0.68$ $Å^{-1}$ is more difficult to reconcile because there are no predicted peaks at that q region.

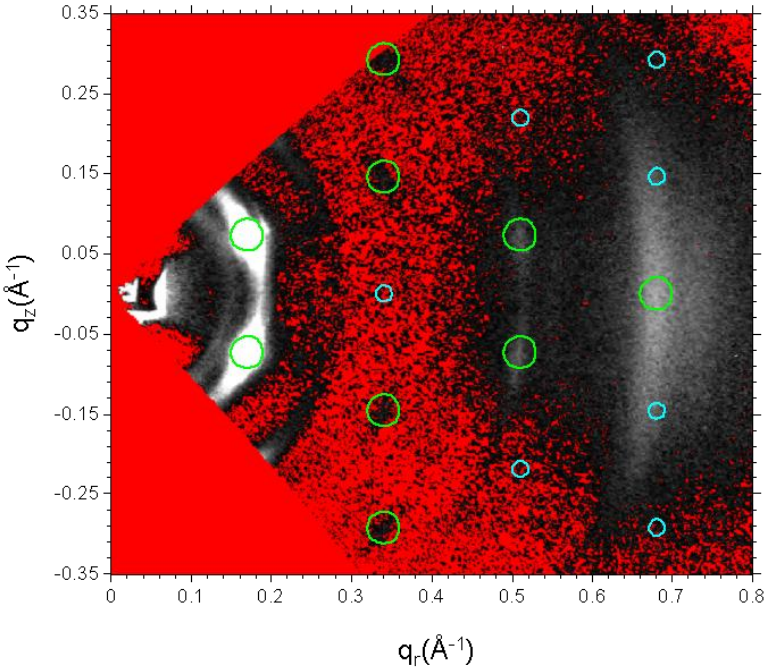


Figure 5.11: Composite of peaks in Fig. 5.8 and the theoretical predictions of the 2-D monoclinic model with a=37 Å, c=46.8 Å and α=66.8$^{o}$. The green and cyan circles have the same meaning as in Fig. 5.9.

Table 5.5 Miller indices [H, L] for peaks listed in Table 5.1 and 5.2 based on the 2-D monoclinic structure.

| | peak I | peak II | peak III | peak IV | peak V | peak VI |
|---|---|---|---|---|---|---|
| [H, L] | ±1,0 | ±2, 0 | ±2, ∓1 | ±3, ±1 | ±4, ±2 | ±1, ∓1 |

The 2-D monoclinic structure of Alm peptides in oriented multilayer samples might seem a little bit of stretch since this requires the length scale in the y direction to be

infinite (or large enough to not see significant Bragg rod extension). Since our sample is a 2-D in-plane fluid like powder average, it is natural to assume that there are two periodicities parallel to the bilayer surface and they are the same. This packing model is the so called 3-D monoclinic structure illustrated in Fig. 5.10B (if $\gamma=60^{o}$, the packing model will be the so called rhombohedral structure, the same as the hexagonal ABC stacking which has been disproved in section 5.5). The (reciprocal) primitive vectors of the 3-D monoclinic structure are

$$\begin{aligned} a_1 &= [a, 0, 0] & a_2 &= [0, b, 0] & a_3 &= [c\cos(\alpha), 0, c\sin(\alpha)] \\ b_1 &= [\frac{1}{a}, 0, 0] & b_2 &= [0, \frac{1}{b}, -\frac{\cot(\alpha)}{b}] & b_3 &= [0, 0, \frac{1}{c\sin(\alpha)}] \end{aligned} \qquad (5.17)$$

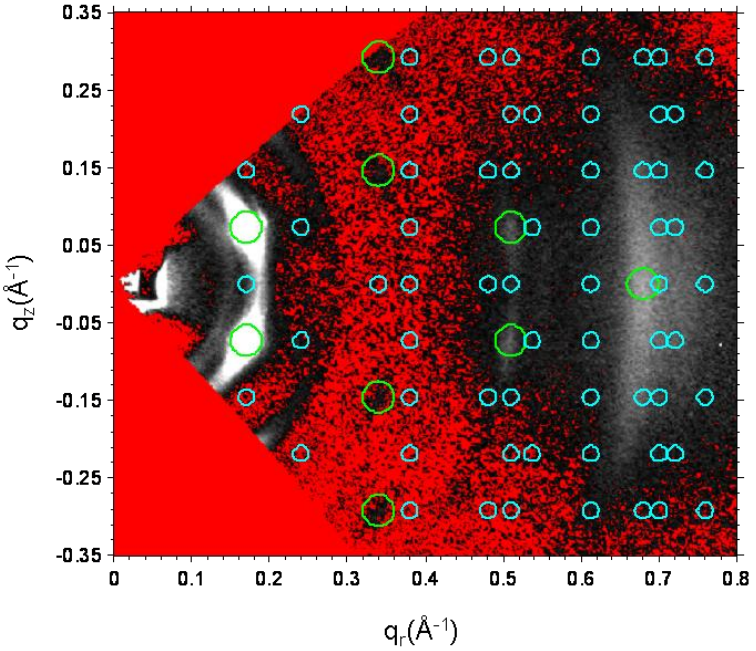


Figure: 5.12: Composite of the peaks in Fig. 5.8 and the theoretical predictions of the 3-D monoclinic model with a=b=37 Å, c=46.8 Å and $\alpha=66.8^{o}$. The green and cyan circles have the same meaning as in Fig. 5.9.

Figure 5.12 shows the composite of the experimental data and the predictions of the 3-D monoclinic packing model with a=b=37 Å, c=46.8 Å and $\alpha=66.8^{o}$. The additional in-plane dimension makes the appearance of a lot of extra scattering peaks that are not present in the experiment. One of the missing peaks is the second order peak along the first column which should be a strong one similar to peak VI in Fig. 5.7B. This makes the 3-D monoclinic packing model unlikely and leads us to at least consider the possibility that the Alm peptides form a 2-D monoclinic structure in the oriented multilayer samples at extremely dehydrated conditions.

Table 5.6 Miller indices [H, K] for 3-D monoclinic model in Fig.5.12.

| column | 1st | 2nd | 3rd | 4th | 5th | 6th | 7th | 8th | 9th |
|---|---|---|---|---|---|---|---|---|---|
| $q_r/2\pi a$ | 1 | $2^{1/2}$ | 2 | $5^{1/2}$ | 2 | 3 | $10^{1/2}$ | $13^{1/2}$ | 4 |
| [H, K] | ±1, 0<br>0, ±1 | ±1, ±1<br>±1, ∓1 | ±2, 0<br>0, ±2 | ±2, ±1<br>±2, ∓1<br>±1, ±2<br>±1, ∓2 | ±2, ±2<br>±2, ∓2 | ±3,0<br>0, ±3 | ±3, ±1<br>±3, ∓1<br>±1, ±3<br>±1, ∓3 | ±3, ±2<br>±3, ∓2<br>±2, ±3<br>±2, ∓3 | ±4,0<br>0, ±4 |

## 5.7 Extinction effect

In Fig. 5.11 we have seen that the 2-D monoclinic packing model fits the experimental data fairly well except the [2, -1]=(0.34,0) peak which is somehow missing. Recall that the scattering intensity is the product of the structure factor, which are delta

functions in the reciprocal space as indicated by the circles in Fig. 5.11, and the form factor, which is the Fourier transform of the electron density distribution of the scattering entity (peptide bundle in this case), the predicted theoretical peak based on the structure factor can get extinct if the form factor at that peak position is zero.

To explore this possibility we constructed a hexamer bundle based on a known hexamer obtained from vacuo restrained MD simulations [81, 113] illustrated in Fig. 5.13A. The modification involves moving each peptide toward or away from the bundle center by a certain amount. Fourier transform was performed for each new bundle and its value was examined at (0.34, 0) position. The bundle that has near zero value at (0.34, 0) shown in Fig. 5.14 was obtained by moving each peptide toward the bundle center by 2.4Å illustrated in Fig. 5.13B. Other bundles with different number of peptides are also tried using similar procedures. Local minimum value at (0.34, 0) can always be obtained by adjusting the travel distance of each peptide toward the bundle center. Even though this does not necessarily mean that the real scattering entity in our experiment corresponds to the constructed peptide bundles, it is certainly promising that the missing peak at (0.34, 0) could be due to the extinction effect from the form factor of the scattering entities. Other sources that can result in peak extinction includes the thermal fluctuations of the unit cell or hopping from one lattice site to another [24].

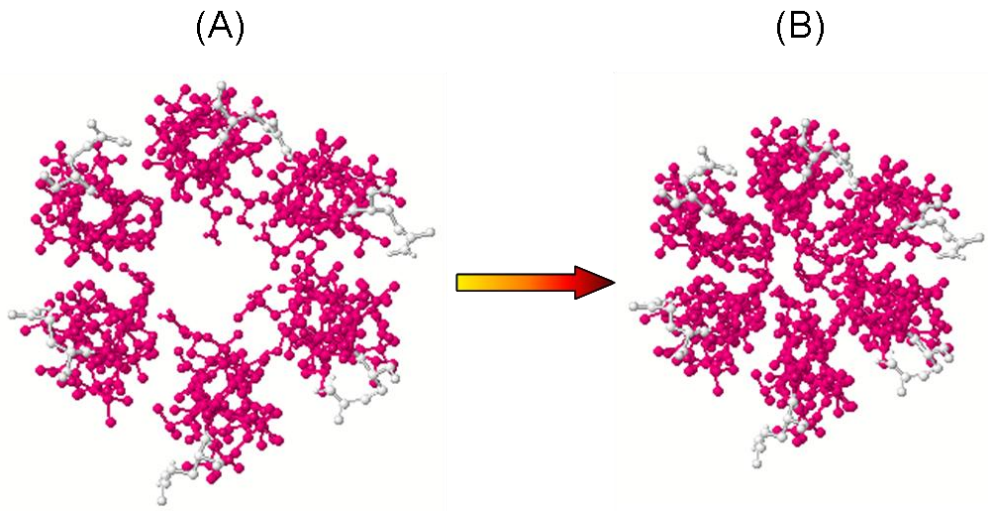


Figure 5.13: (A) Hexamer bundle generated with vacuo restrained MD simulations [81, 113]. (B) Modified hexamer bundle by moving each peptide toward their center by 2.4Å from (A).

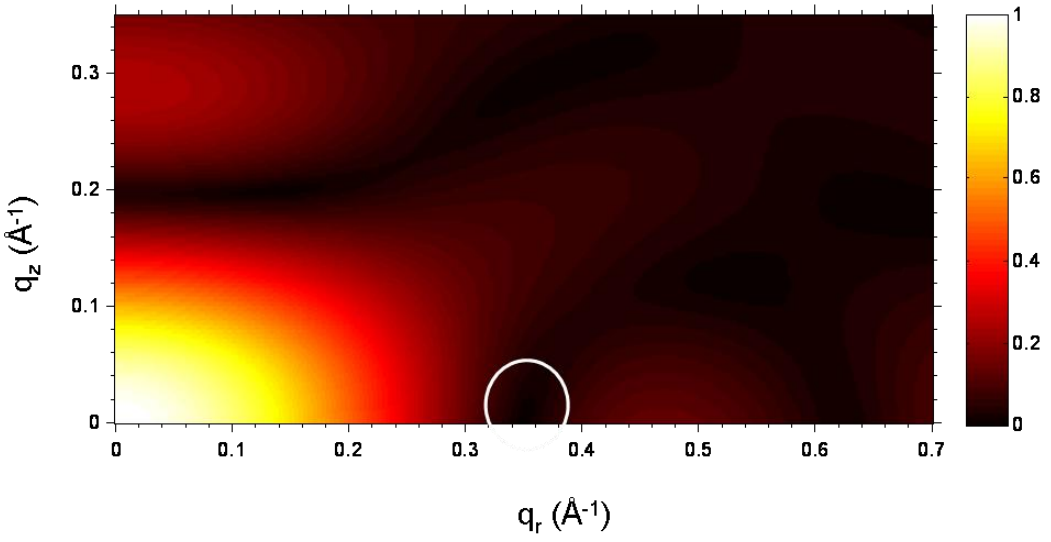


Figure 5.14: Form factor of a constructed Alm hexamer (Fig.5.15B) with local minimum at ($q_r$, $q_z$) = (0.35, 0) indicated by the white circle.

## 5.8 Effect of thermal fluctuations and disorder

The lack of enough scattering peaks makes it difficult to determine the space group of the scattering entities. One major source of this problem is thermal fluctuations and disorder which are usually described by the well known Debye-Waller factor (DWF) [36], also called the B factor or the temperature factor. To illustrate the idea of DWF, let us consider a one dimensional case in which the thermal fluctuations follow a harmonic oscillation. Showing without proof, the Debye-Waller factor is $\exp(-q^2\langle u^2\rangle/3)$, where u is the deviation of the harmonic oscillation from the center. The DWF is dependent on the reciprocal space vector q. As q increases, the DWF decreases rapidly. This means the attenuation due to the thermal fluctuations or disorder is more prominent for scattering at larger q value. This explains the disappearance of the higher orders of the Bragg peaks when the multilamellar samples become more hydrated.

In practice, it has been shown that it is more difficult to obtain higher orders in the $q_r$ direction than in the $q_z$ direction for Alm/lipid samples [24, 39]. The source of the horizontal disorder of an Alm bundle that limits the scattering in the in-plane direction includes the positional variation of each bundle within a unit cell and the positional variation of the peptides within each bundle [24]. This inherent nature of the soft matter lattice within lipid membranes prohibits us from being able to determine the molecular structure of the scattering entities like in protein crystallography.

## 5.9 Hydration effect on the scattering patterns

As has been shown in the previous chapter, when the multilayer sample gets hydrated, the strong correlation between Alm bundles in different layers becomes weaker and vanishes eventually. This trend is illustrated in Fig. 5.15. From the figure we see that when the lamellar repeat spacing D increases from 42 to 48Å, the scattering peaks become much more diffuse. This is related to the increased thermal fluctuations of the Alm bundles. Figure 5.15 also shows an important feature we mentioned in chapter 3 that when there are correlations between the scattering entities in different layers, the scattering maximum of the side peak at $q_r$ ~0.1Å$^{-1}$ is not located at $q_z$=0, which is indicative of the repulsive interactions at short distances between the scattering entities in different layers.

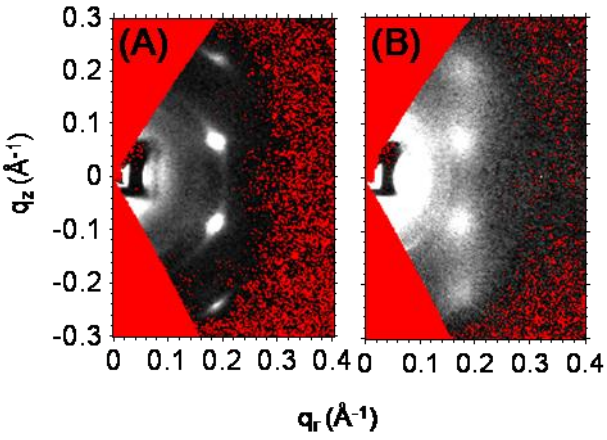


Figure 5.15: The scattering pattern of Alm:DOPC 1:10 with sample rotation angle α=30$^o$ at (A) D=42Å and (B) D=48Å.

## 5.10 Conclusions

To explore the Alm peptide packing structure in oriented multilayer samples at low hydration, a transmission scattering experiment was applied. Sufficient scattering orders were obtained to enable us to unambiguously determine that Alm peptides in our samples do not form the conventionally anticipated hexagonal AB or hexagonal ABC stacking. Hexagonal AB stacking for Alm in DMPC bilayers was suggested in [39], and their observed orders ruled out hexagonal ABC stacking. We also observed the same orders they did, but it is the additional orders we observed that rule out hexagonal AB stacking for Alm in DOPC bilayers. Hexagonal ABC (rhombohedral) stacking has been reported for Alm in DSPC [24, 38]. The observed orders for $q_r \sim 0.1$ Å$^{-1}$ had a distinctive pattern in $q_z$ consistent with hexagonal ABC stacking, but quite different from our pattern or from [39], and clearly require a different structure than for our samples. Such differences could be due to the different lipid and/or to different levels of hydration and sample preparation.

For our data, other packing models were considered including the body centered tetragonal, 2-D and 3-D monoclinic structures, all of which have predicted scattering peaks at all the experimental peak positions. Although it is usually supposed that in-plane circular objects will tend towards hexagonal in-plane packing, repulsive interactions between adjacent bilayers could favor the in-plane square packing that occurs in the body centered tetragonal structure. However, the body centered tetragonal structure requires extinction of rather many peaks. By this criterion, the 2-D monoclinic structure would be

favored because it requires many fewer extinctions, but it has a rather counter-intuitive structure with no spatial variation in one of the in-plane directions.

Transmission experiments also confirmed that the maximum scattering intensity for the first Bragg rod is off the equator when there is correlation between the scattering entities in different layers in samples at intermediate hydration.

## 5.11 Appendix: Electron density map

The electron density map can be constructed from the peak positions and peak intensities in reciprocal space by assigning phases to each peak.

$$\rho(\mathbf{R}) = \sum_i \pm \sqrt{I_i}\, \exp(i\mathbf{q} \bullet \mathbf{R}) \tag{5.18}$$

The ± sign represents the phase of each peak. It can be +1 or -1 by assuming centrosymmetry of the unit cell. Although there are several ways that can be applied to solve the phase problem in lipid bilayer systems including the mutliwavelength anomalous diffraction (MAD) [24] and the swelling method [134], these could not be performed in this work. The summation of equation (5.18) is over all of the peaks including the lamellar diffraction peaks centered at $q_r$=0. Assuming there is a mirror plane parallel to the bilayer, equation (5.18) can be reorganized into

$$\begin{aligned}\rho(\mathbf{r}, z) &= \sum_{i, q_z \geq 0, q_r \geq 0} \pm \sqrt{I_i} \begin{pmatrix} \exp(iq_z z + iq_r \bullet \mathbf{r}) + \exp(-iq_z z + iq_r \bullet \mathbf{r}) \\ + \exp(iq_z z - iq_r \bullet \mathbf{r}) + \exp(-iq_z z - iq_r \bullet \mathbf{r}) \end{pmatrix} \\ &= \sum_{i, q_z \geq 0, q_r \geq 0} \pm 2\sqrt{I_i} \left(\cos(q_z z + q_r \bullet \mathbf{r}) + \cos(q_z z - iq_r \bullet \mathbf{r})\right) \\ &= \sum_{i, q_z \geq 0, q_r \geq 0} \pm 2\sqrt{I_i}\, \cos(q_z z)\cos(q_r \bullet \mathbf{r}) \end{aligned} \tag{5.19}$$

The peak positions and intensities at $q_z$, $q_r \geq 0$ listed in Table 5.7 are obtained from Fig. 5.7B and 8. The peak position in Fig 5.7B was adjusted in order to make the hydration level the same as in Fig. 5.8. One issue for the transmission scattering experiment is that there are missing peaks at $q_r=0$ due to the rotation of the sample. The omission of these peaks in electron density constructions is known to cause severe distortion due to their strong peak intensity [24]. To deal with this issue, an arbitrary large intensity was assigned to the first order lamellar diffraction peak [0,0,1] at $q_r=0$. The phase for each peak is another problem based on equation (5.19). However, as the intensity of the lamellar peak which defines the main feature of the electron density in the z direction and the intensity of peak I which defines the main feature in the in-plane direction are the largest, the exact phase choices for the rest of the peaks do not matter much.

Table 5.7 Experimental peaks from Fig. 5.7B and Fig. 5.8.

| | Exp ($q_r$, $q_z$) ($Å^{-1}$) | Average intensity I | Phase |
|---|---|---|---|
| peak I | 0.173, 0.069 | 7500 | -1 |
| peak II | 0.340, 0.143 | 100 | -1 |
| peak III | 0.338, 0.299 | 86 | -1 |
| peak IV | 0.510, 0.070 | 265 | -1 |
| peak V | 0.680, 0.00 | 470 | -1 |
| peak VI | 0.17, 0.21 [a] | 1796 | -1 |
| [0,0,1] | 0.00, 0.07 | 20000 [b] | +1 |

[a] The position of peak VI was adjusted from Table 5.2 in order to make the hydration level the same for all of the peaks.

[b] An arbitrary intensity was assigned to the first order lamellar peak [0,0,1].

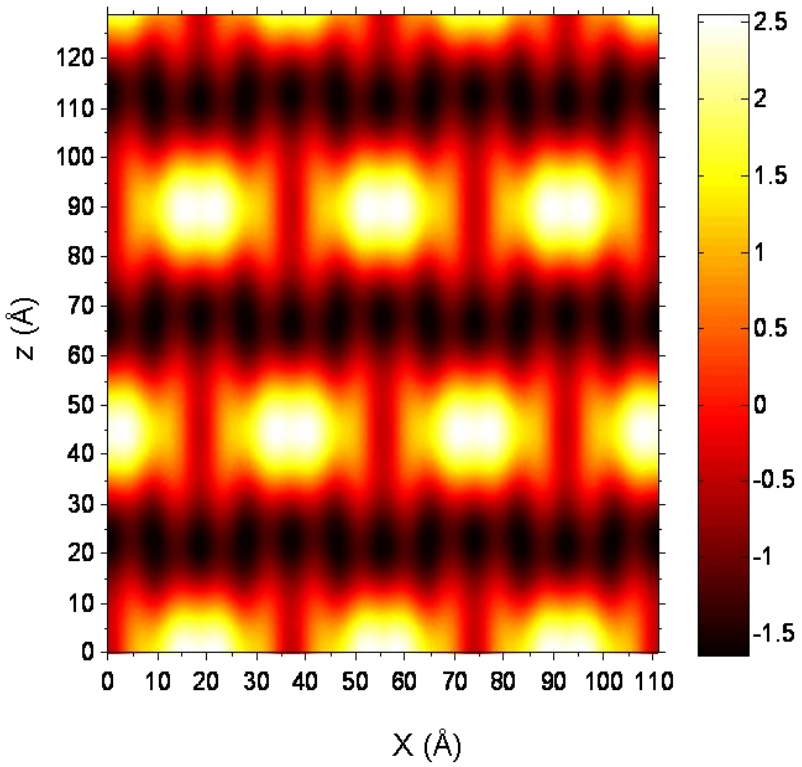


Figure 5.16: Electron density map in the x-z plane constructed from Table 5.7 based on equation (5.19).

An example of the electron density map in the x-z plane based on the phases listed in the last column in Table 5.7 is shown in Fig. 5.16. Within the unit cell there is an electron dense region with height h ~30Å and width r ~30 Å, corresponding very well to the suggested peptide bundle structure [32, 35]. The staggered arrangement of the electron dense regions in the neighboring rows is consistent with the in-plane repulsive interactions between neighboring layers in chapter 3. Other combinations of the phases are also tried out. Many of them yield similar electron dense regions consistent with the peptide bundle structure.

One weakness of Fig. 5.16 is that the phosphate headgroup is not obvious. A similar problem has been noticed for the electron density map constructed from samples with brominated lipids [24]. One possible source of this problem is thermal fluctuations of the headgroups. Another issue in Fig 5.16 is that the electron dense region corresponding to the peptide occupies most of the volume in one unit cell. This is inconsistent with the peptide to lipid ratio 1:10. A similar result was reported for a rhombohedral lattice where the peptide to lipid ratio does not change as a function of the peptide concentration and the ratio is far larger than the experimental ratio [24]. This difference of the peptide to lipid ratio in the unit cell and in the bulk sample suggests that there might be phase separation between the peptide bundles and the lipid molecules. The lack of lipid molecules in the unit cell may also contribute to the lack of phosphate headgroups in Fig. 5.16.

Figure 5.17 shows another electron density map constructed from Table 5.7 by reversing the phases of each peak. This map makes more sense in a way that the electron dense phosphate is observable (the rows with the largest electron density). The peptide is represented by the thin vertical strips (medium electron density region) staggered with the lipid hydrocarbon chains (the lowest electron density region). The peptide to lipid ratio is more consistent with the experimental ratio. The disadvantage of this map is that it does not show any peptide bundle structure.

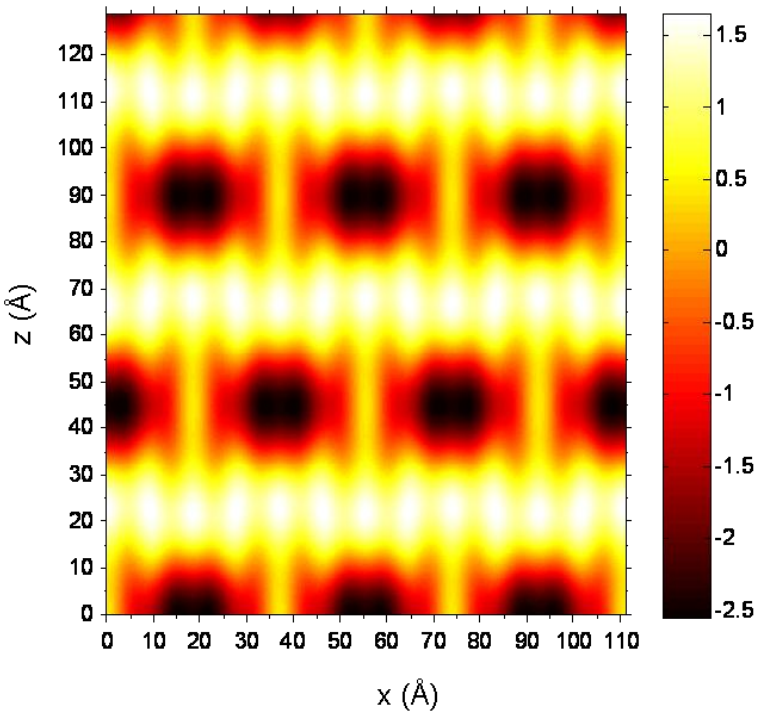


Figure 5.17: Electron density map constructed from Table 5.7 by reversing the phases of each peak.

# Chapter 6
# A second peak due to alamethicin incorporation

## 6.1 Introduction

In chapter 4, we were focusing at $q_r$ range less than 0.6 $Å^{-1}$. Other interesting features due to Alm incorporation are observed at larger $q_r$. A second scattering peak at medium $q_r$ value was observed for all of the peptide concentrations in both DOPC and diC22:1PC. By model fitting, this peak was found to be located at $q_r \sim 0.7 Å^{-1}$ and is much broader than the side peak at $q_r \sim 0.1 Å^{-1}$. This q value reflects the characteristic distance, ~10Å, between the scattering entities, which is the diameter of an α-helix. In this chapter, three models are proposed in order to explore the source of this peak and two of them are rejected. Another interesting result in the large q region is that the chain wide angle scattering at $q \sim 1.4$ $Å^{-1}$ is well preserved.

## 6.2 Wide angle scattering for Alm/DOPC mixtures

Figure 6.1 shows the background subtracted wide angle x-ray scattering images at four Alm:DOPC ratios. As the concentration of the peptide increases, the chain wide angle scattering peak at q~1.4Å$^{-1}$ is well preserved. This is very different to another antimicrobial peptide magainin which has been shown to severely disrupt the bilayer structure and consequently decrease the chain wide angle scattering [135, 136]. Figure 6.1 also shows that there is a diffuse scattering like peak at $q_r$ ~0.7Å$^{-1}$ that becomes more intense as the peptide concentration increases.

In order to have a quantitative idea about how the intensity of the peak at $q_r$ ~0.7Å$^{-1}$ changes as a function of the peptide concentration, we plotted the intensity along the $q_r$ direction near $q_z$ ~0 in Fig. 6.2. The intensity is obtained by averaging a width of $0.04<q_z<0.17$ Å$^{-1}$. The obtained intensity is then fit by the sum of three components, two Gaussian functions representing the two peaks centered at $q_r$ ~0.7 and 1.4 Å$^{-1}$ and a second order polynomial background. The chain wide angle scattering peak at $q_r$ ~1.4 Å$^{-1}$ is normalized in order to compare the intensity of the peak at $q_r$ ~0.7 Å$^{-1}$. The figure shows that even for the pure lipid, there is a peak at $q_r$ ~0.7 Å$^{-1}$ which is due to the less pronounced correlation between the lipid headgroups [135, 137]. As the concentration of the peptide increases, the peak becomes more and more intense. The first thought might be that since the peak in pure lipids is due to the heapgroup correlation, then the reason for the increased intensity might be that the peptide makes the lipid headgroups more rigid. However MD simulations have shown that the electron density distribution of the

lipid headgroup is almost not affected by the incorporation of Alm peptides in a DOPC bilayer [97]. This eliminates one possibility for the enhanced peak intensity at $q_r$ ~0.7Å$^{-1}$.

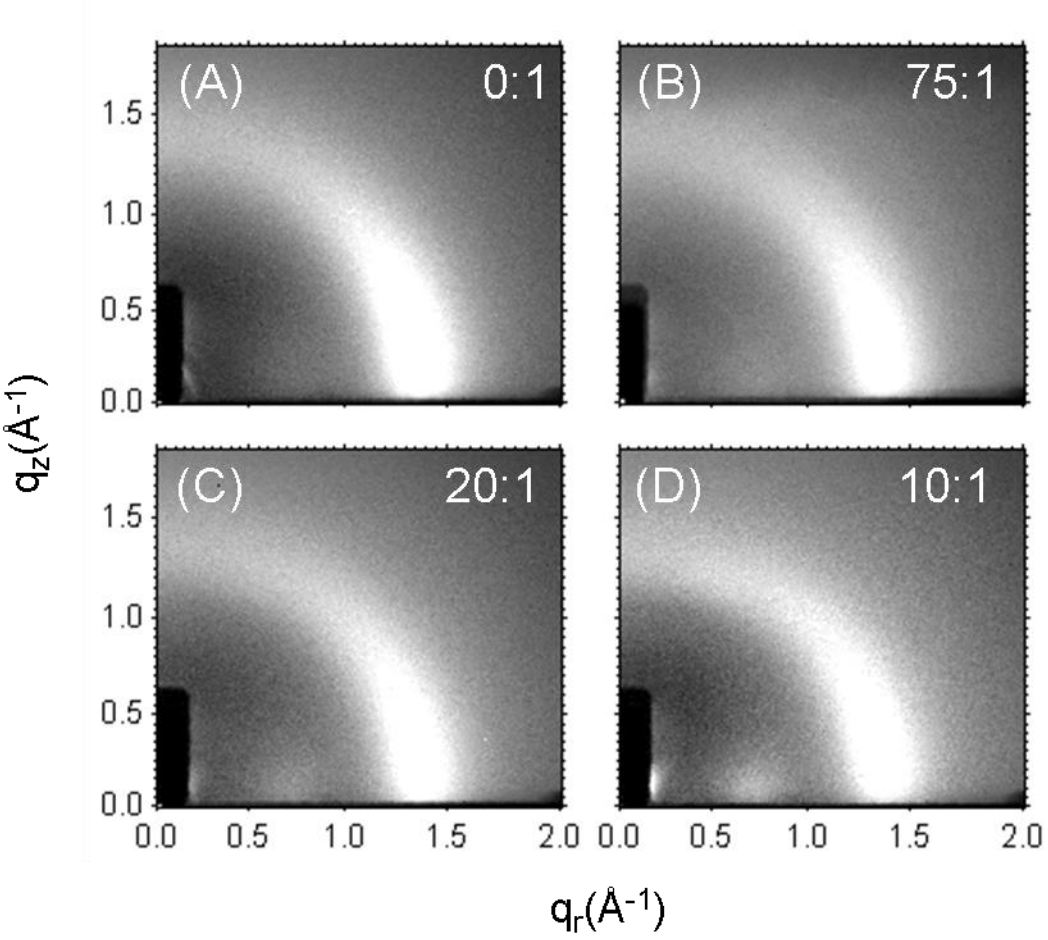


Figure 6.1: Background subtracted wide angle x-ray scattering images for Alm:DOPC. The ratios are indicated by the white numbers. The black region in the left bottom corner in each panel is where a piece of molybdenum attenuator is used to attenuate the direct beam and the lamellar peaks.

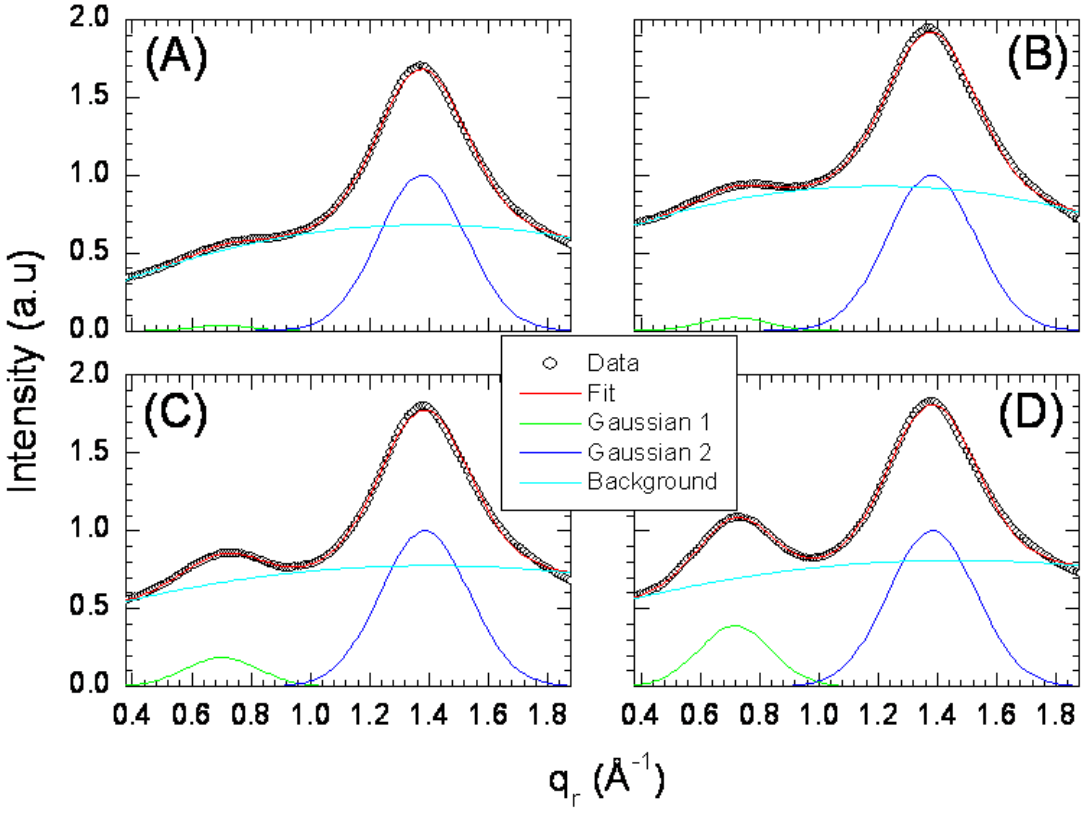


Figure 6.2: Intensity along the $q_r$ direction averaged over $0.04<q_z<0.17$ Å$^{-1}$ for Alm:DOPC in Fig.6.1. (A) 0:1, (B) 1:75, (C) 1:20, and (D) 1:10. Each data set is fit by the sum of three components: two Gaussian functions representing the two peaks centered at $q_r$ ~0.7 and 1.4 Å$^{-1}$ and a second order polynomial background.

## 6.3 Wide angle scattering for Alm/diC22:1PC mixtures

Figure 6.3 shows the wide angle scattering for Alm:diC22:1PC at four ratios. Similar to DOPC, the peak at $q_r$ ~0.7Å$^{-1}$ becomes more and more intense as the peptide concentration increases. The scattering intensity along the $q_r$ direction is shown in Fig. 6.4. A similar peak decomposition as in Fig. 6.2 was carried out. The fitting parameters for the peaks are listed in Table 6.1 (the fits for the samples with low peptide concentrations are less obvious due to the large background.). From the table we see that the width and the position of the peak almost do not change as a function of the peptide concentration for both lipids. This is different from the side peak at $q_r$ ~0.1 Å$^{-1}$ in chapter 4 where we have shown that the side peak consistently moves to smaller $q_r$ value when the peptide concentration decreases. Another difference is that the side peak at $q_r$ ~0.1 Å$^{-1}$ is at smaller $q_r$ value for diC22:1PC than for DOPC, while Table 6.1 shows that the peak at $q_r$ ~0.7Å$^{-1}$ for diC22:1PC has essentially the same $q_r$ value as for DOPC. Of course, the above statements are all subject to uncertainties such as modeling the peak as a Gaussian function and the background as a second order polynomial function.

Table 6.1 The width and position of the peaks at $q_r$ ~0.7Å$^{-1}$ in Fig. 6.2 and Fig. 6.4 modeled as a Gaussian function.

| | σ (Å$^{-1}$) | $q_r$ (Å$^{-1}$) |
|---|---|---|
| Alm:DOPC 1:10 | 0.122 | 0.717 |
| Alm:DOPC 1:20 | 0.123 | 0.701 |
| Alm:diC22:1PC 1:10 | 0.104 | 0.722 |
| Alm:diC22:1PC 1:21 | 0.094 | 0.723 |

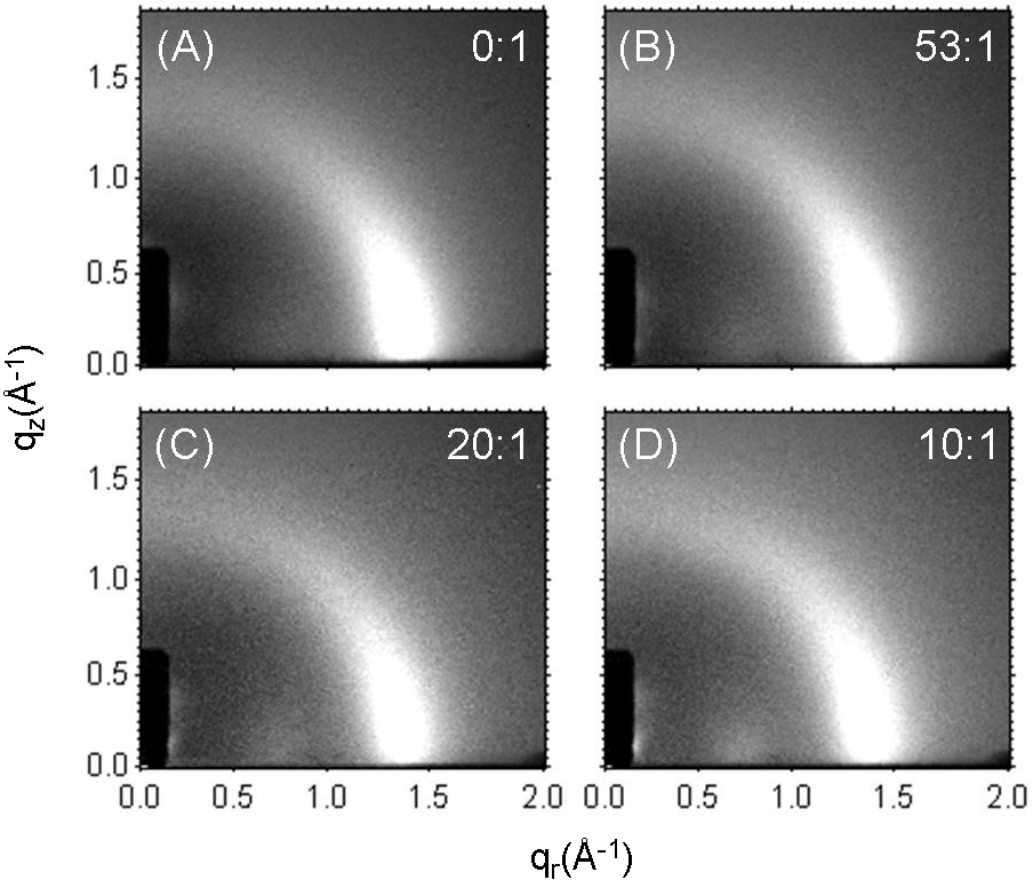


Figure 6.3: Background subtracted wide angle x-ray scattering images for Alm:diC22:1PC at four ratios indicated by the white numbers.

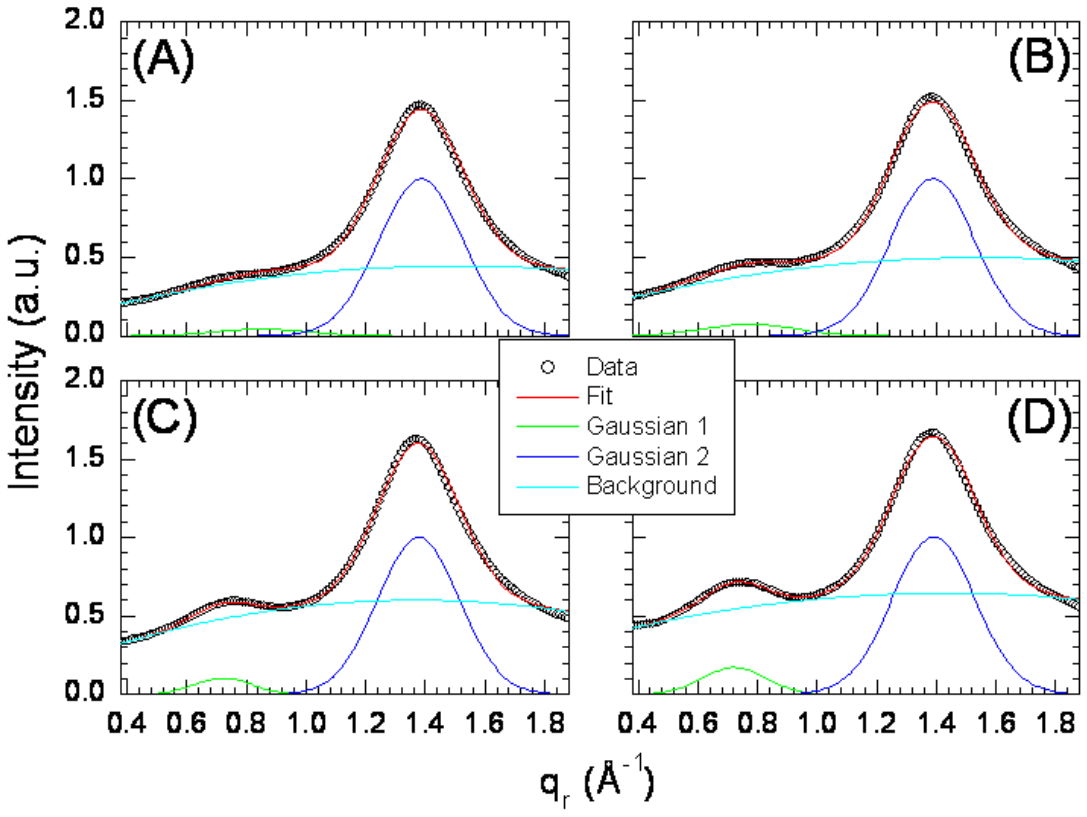


Figure 6.4: Intensity along the $q_r$ direction averaged over $0.04<q_z<0.17$ Å$^{-1}$ for Alm:diC22:1PC in Fig.6.3. (A) 0:1, (B) 1:53, (C) 1:20, and (D) 1:10. The peak decomposition procedure is the same as in Fig.6.2.

## 6.4 Scattering over a larger range of q

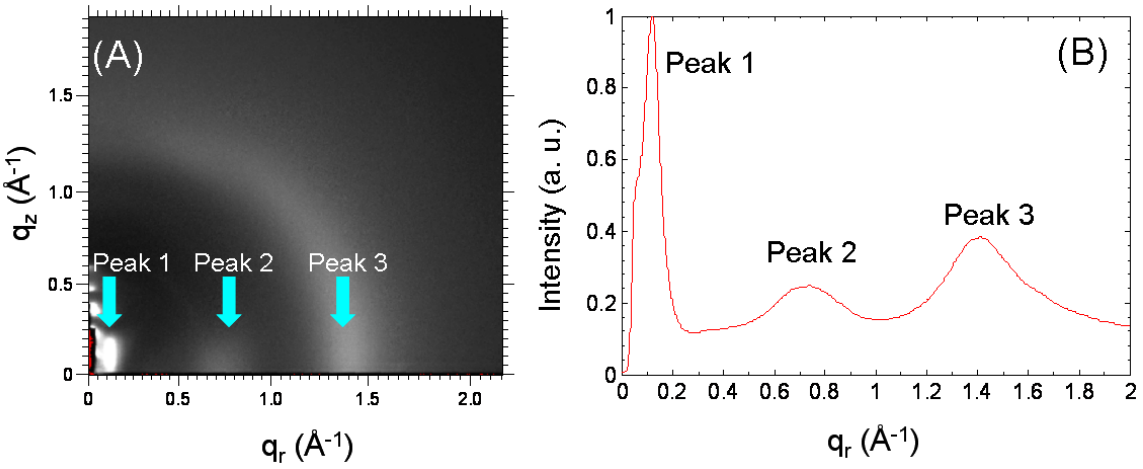


Figure 6.5: (A) Background subtracted wide angle x-ray scattering image for Alm:DOPC 1:10. There are two peaks caused by the incorporation of Alm peptides, peak 1 at $q_r$ ~0.1 Å$^{-1}$ and peak 2 at $q_r$ ~0.7 Å$^{-1}$. Peak 3 at $q_r$ ~1.4 Å$^{-1}$ is the usual lipid chain wide angle scattering. (B) Intensity along the $q_r$ direction averaged over $0.04<q_z<0.17$ Å$^{-1}$.

So far we have seen two scattering peaks due to the incorporation of Alm peptides. An illustration is shown in Fig. 6.5A for Alm:DOPC 1:10. The intensity plot along the $q_r$ direction near $q_z$ ~0 is shown in Fig. 6.6B. To make the discussion easier, we note the scattering at $q_r$ ~0.1Å$^{-1}$ as peak 1 and the scattering at $q_r$ ~0.7Å$^{-1}$ as peak 2. From the figure we see that peak 1 has a much narrower width and larger intensity than peak 2. In section 6.2 we have ruled out the possibility that the source of peak 2 is the increased ordering of the lipid headgroups. This leads us to the hypothesis that peak 2 is also related to the Alm peptides. We will discuss the possible sources of peak 2 in the following section.

## 6.5 What is the source of peak 2?

The position of peak 2 indicates that the characteristic distance between the scattering entities is around 10 Å, which is the diameter of an α-helix. There are several ways to obtain this distance based on the possible peptide arrangements.

### 6.5.1 The well defined peptide-peptide distance within a bundle

He et al. [22] reported a similar peak to our peak 2 in an Alm:DLPC 1:10 sample. The authors claimed that it was due to the nearest peptide-peptide packing distance within a bundle. In order to test their theory, we are going to use the cylinder bundle model established in chapter 5 except that this time we distinguish each peptide within the bundle. The procedure is to discretize the hollow cylinder into N (integer) solid cylinders, each of which represents a peptide as shown in Fig. 6.6B. In the refined bundle model, the peptides are packed in a barrel-stave structure [35].

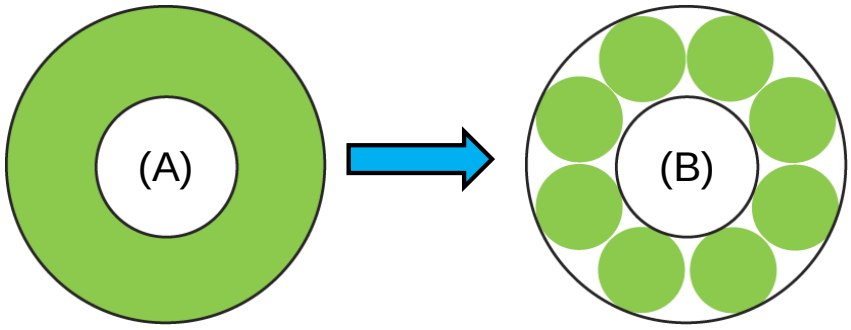


Figure 6.6: Discretize a hollow cylinder bundle into a bundle with N solid cylinders.

There are two ways to calculate the scattering intensity from the bundle structure in

Fig. 6.6B. One way is to consider each bundle as a scattering entity. Then the structure factor S(q) can be calculated by the same 2-D hard disk model as in chapter 4. The peptide-peptide distance is only involved in the form factor $F_P(q)$ of each bundle. Define $\mathbf{R}_k$ as the position of the kth peptide relative to the bundle center and **r** as the coordinate in the peptide frame, the form factor of the refined bundle model in Fig. 6.6B with N peptides in each bundle can be calculated as following

$$\begin{aligned} F_P(\mathbf{q}) &= \sum_{k=1}^{N} \int \exp[-i\mathbf{q}\bullet(\mathbf{R}_k + \mathbf{r})]d^2\mathbf{r} \\ &= \left[\int \exp[-i\mathbf{q}\bullet\mathbf{r}]d^2\mathbf{r}\right] \times \left[\sum_{k=1}^{N} \exp(-i\mathbf{q}\bullet\mathbf{R}_k)\right] \\ &= F_{mon}(\mathbf{q}) \times F_{pos}(\mathbf{q}) \end{aligned} \tag{6.1}$$

where $F_{mon}(\mathbf{q}) = \int \exp[-i\mathbf{q}\bullet\mathbf{r}]d^2\mathbf{r}$ is the form factor of a peptide monomer; $F_{pos}(\mathbf{q}) = \sum_{k=1}^{N} \exp[-i\mathbf{q}\bullet\mathbf{R}_k]$ reflects the positional correlation between the peptides forming a polygon with N vertices within the N-bundle. Defining d as the distance between each vertex and the polygon center, the $F_{pos}(q_r)$ can be written as [25]

$$\begin{aligned} |F_{pos}(q_r)|^2 &= \left|\sum_{k=1}^{N} \exp[-iq_r\bullet\mathbf{R}_k]\right|^2 \\ &= 1 + 2\sum_{k=1}^{N} (1 - k/N) J_0\left(2qd \times \sin(\pi k/N)\right) \end{aligned} \tag{6.2}$$

The form factors of the refined bundle models based on equation (6.1) with the number of peptides per bundle N changing from 6 to 8 are shown in Fig. 6.7. From the figure we see that $|F_{pos}(q_r)|^2$ does have peaks at q~0.3 and 0.7 $Å^{-1}$ for all of the bundles due to the well defined peptide-peptide distance within the bundle. However, when it is multiplied by the form factor of the monomer $|F_{mon}(q_r)|^2$ which decreases very fast until $q_r$~0.6 $Å^{-1}$,

the peaks at $q_r$~0.7 $Å^{-1}$ are almost not noticeable. The form factor $|F_{mon}(q_r)|^2$ can also be calculated from the molecular structure of Alm which is available from MD simulations and crystallography study. The resulting form factor is very similar to the form factor calculated from the simple cylindrical model.

Figure 6.8 shows the theoretical scattering intensity which is the product of the form factor shown in Fig. 6.7 and the structure factor which is estimated by the same 2-D hard disk model introduced in chapters 3 and 4. The rapidly decreasing form factor and the rapidly increasing structure factor at $q_r$<0.2 $Å^{-1}$ give rise to the peak at $q_r$ ~0.1 $Å^{-1}$ which is consistent with peak 1 in our experiment. A second peak at $q_r$ ~0.3 $Å^{-1}$ is also present in Fig. 6.8. However, there is no observable peaks at $q_r$ ~0.7 $Å^{-1}$.

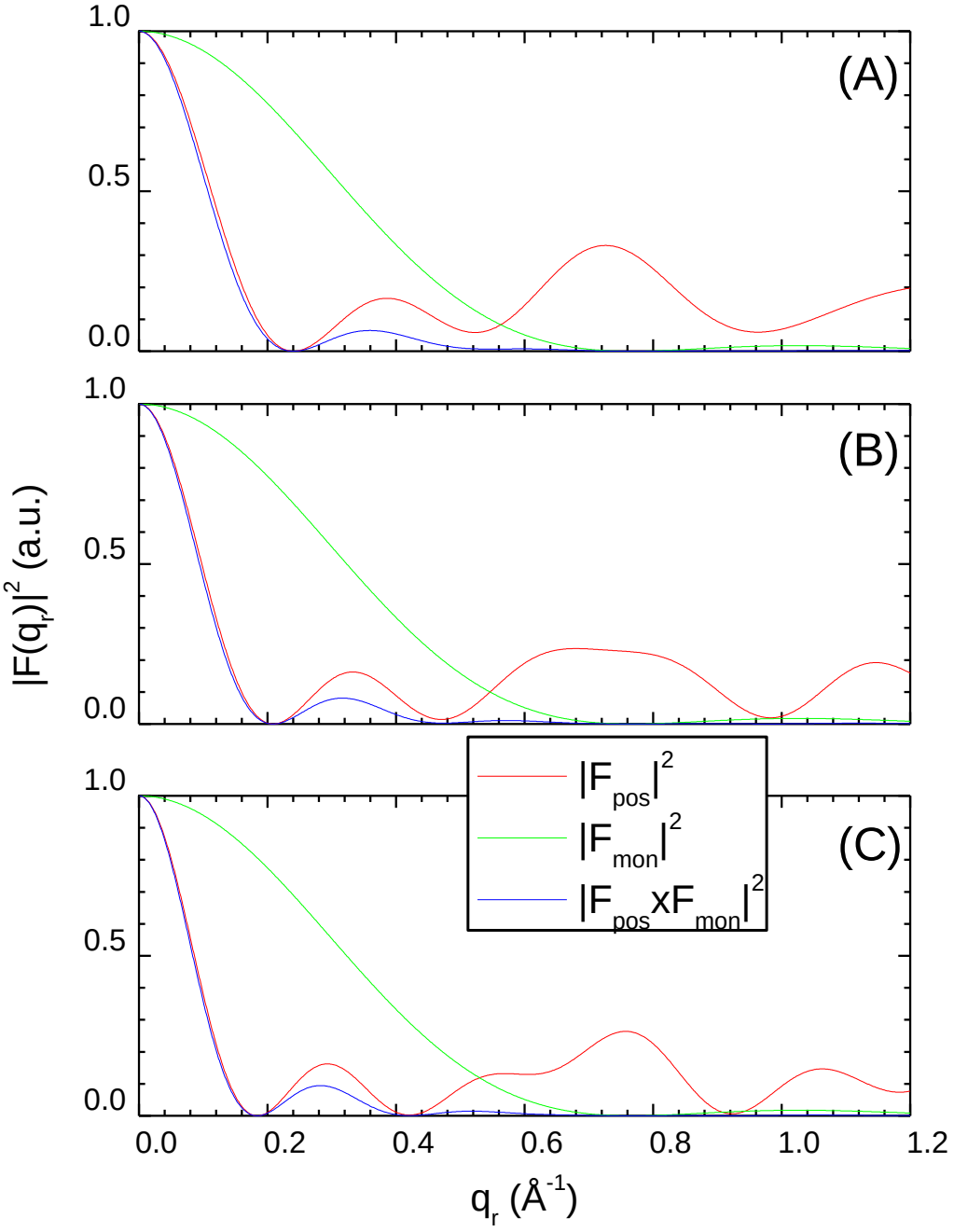


Figure 6.7: Form factors of the refined bundle model in Fig. 6.6B with number of peptides N (A) 6, (b) 7, and (C) 8.

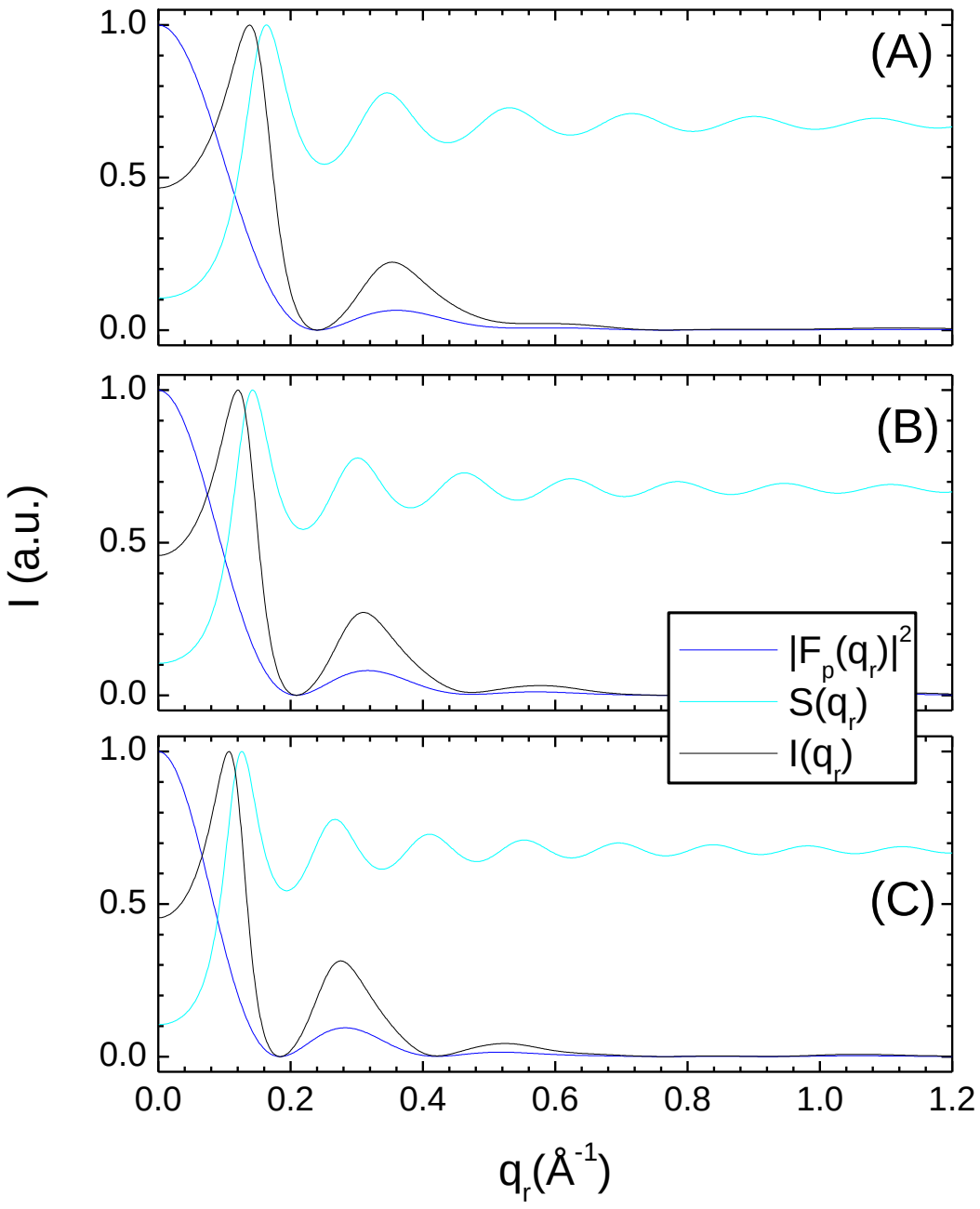


Figure 6.8: The product of the peptide bundle form factor $|F_p(q_r)|^2$ in Fig. 6.7 and the structure factor $S(q_r)$ obtained from 2-D hard disk models with area packing fraction $\eta$=0.4. (A) N=6, (B) N=7, (C) N=8.

The second way to calculate the scattering from the bundle model in Fig. 6.6B is to consider each peptide as a scattering entity. In this case, only the peptide-peptide distance is involved in the structure factor $S(q_r)$. Similar to chapter 3, we use MC simulations to calculate the positional correlation between the peptides. First we apply the same 2-D hard disk model, where no pairs of bundles can overlap, to generate the 2-D distribution of the bundles centered at $(X_1,Y_1)$, $(X_2,Y_2)$,...,$(X_M,Y_M)$, where M is the total number of bundles. After obtaining the position of each bundle, we calculate the coordinates $(X_{i,1}, Y_{i,1})$,..,$(X_{i,N}, Y_{i,N})$ for the N peptides within bundle $(X_i,Y_i)$ based on the model in Fig. 6.6B. A random orientation of the peptides within each bundle is considered. After obtaining the coordinates for all of the peptides in one state, we calculate the radial pair distribution function n(r). The simulation goes on until enough states are generated. The averaged radial pair distribution function n(r) is shown in Fig. 6.9 with the number of peptides per bundle N varying from 6 to 8 (the area packing fraction $\eta$~0.4). The structure factor can be calculated following equation (3.7),

$$S(q_r) \approx 1 + \frac{1}{N}\int (n(r) - \bar{n})\, J_0(q_r r) 2\pi\, r dr \qquad (6.3)$$

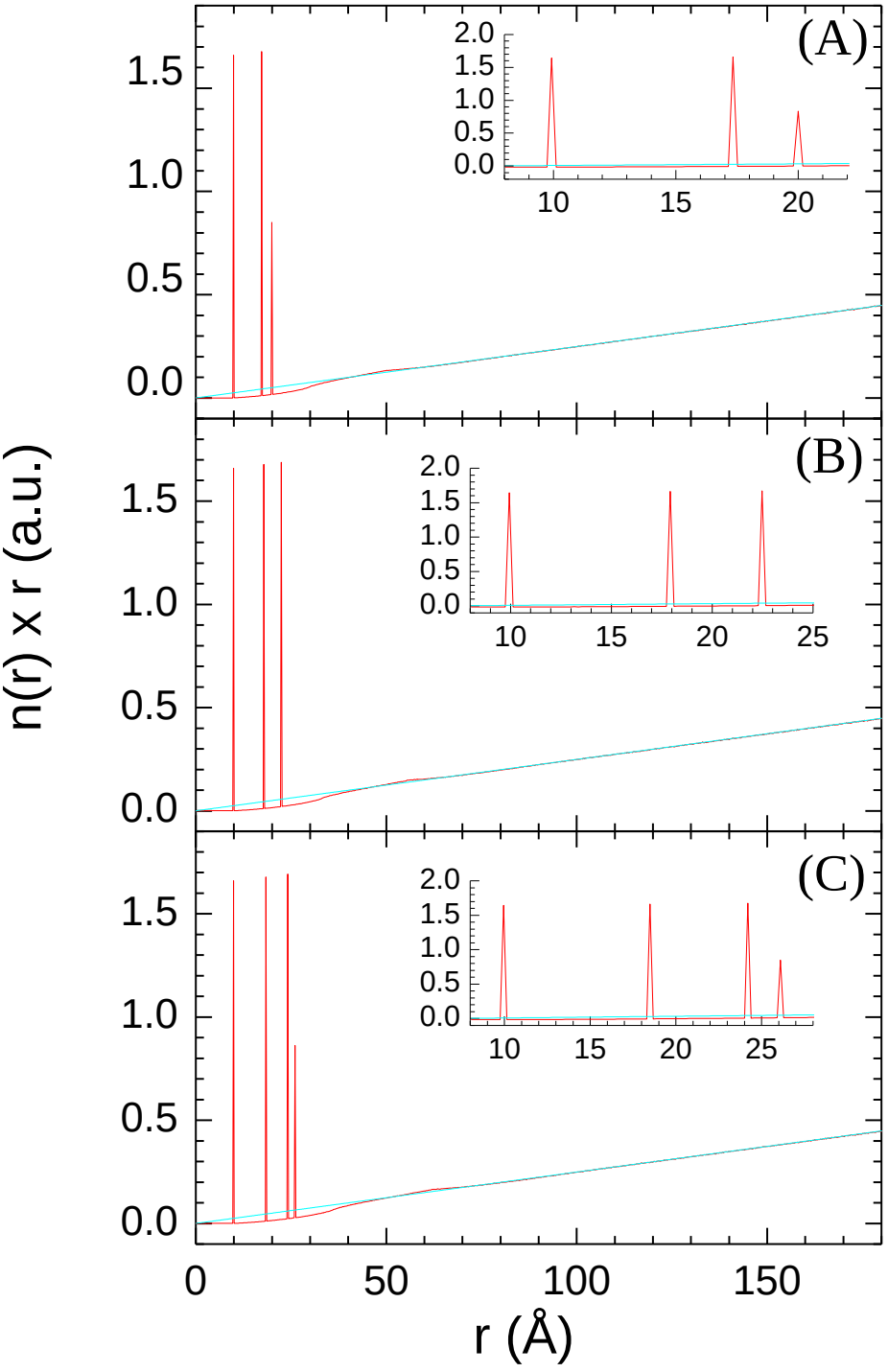


Figure 6.9: Radial pair distribution function n(r) for bundles with number of peptides (A) N=6, (B) N=7, and (C) N= 8. The cyan lines indicate the average pair density. Insets show smaller r range.

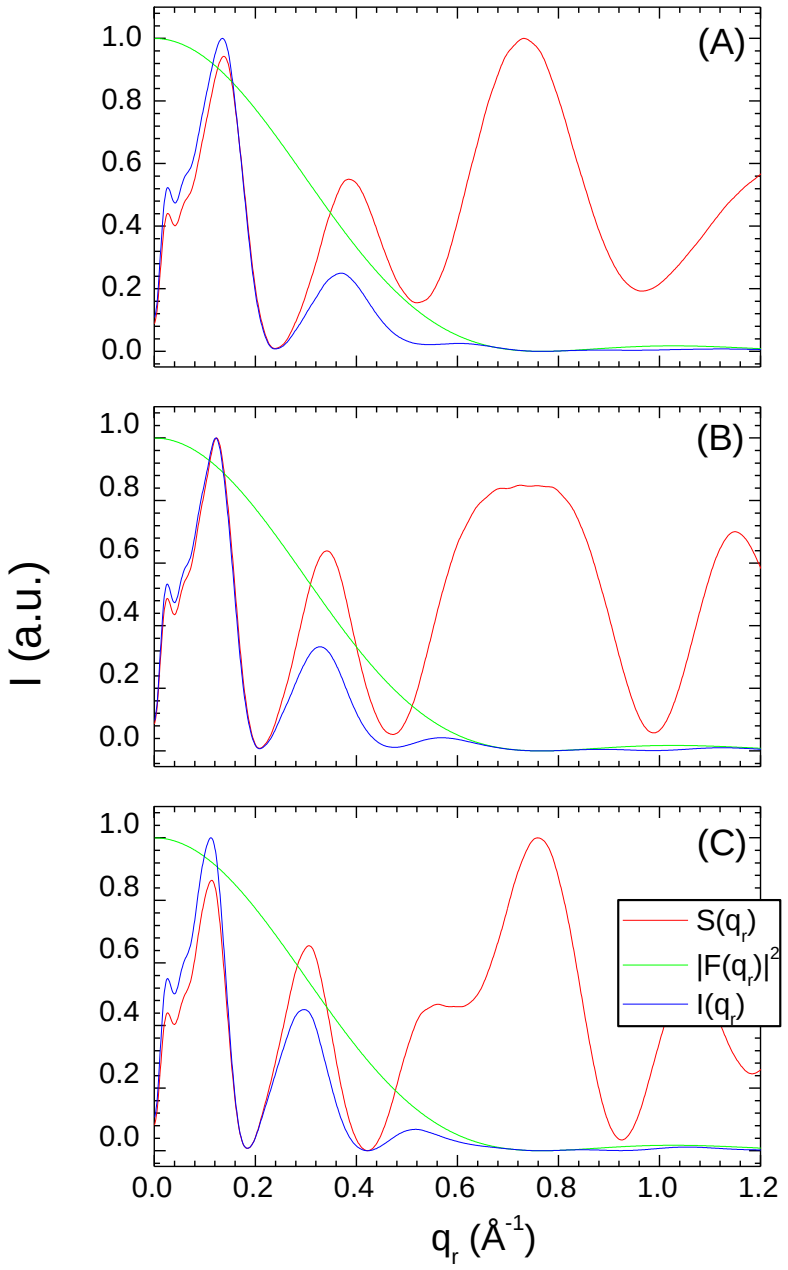


Figure 6.10: The product of the structure factor calculated from the radial pair distribution function n(r) in Fig. 6.9 and the form factor of a cylindrical peptide with radius 5 Å. (A) N=6, (B) N=7, and (C) N=8.

Figure 6.10 shows the product of the structure factor calculated from the radial pair distribution function n(r) in Fig. 6.9 based on equation (6.3) and the form factor of a cylindrical peptide with radius 5 Å. By comparing Fig. 6.10 with Fig. 6.7 we see that the peaks of $|F_{pos}(q_r)|^2$ in Fig. 6.7 are very similar to the peaks of the structure factors in Fig. 6.10 except at small $q_r<0.1$ Å$^{-1}$ region. This is because both of them are related to the well defined peptide-peptide distances within the bundle which are shown as distinctive peaks in the n(r) plot in Fig. 3.9. Based on equation (6.3) these peaks are the main contributions to the structure factor $S(q_r)$ which is basically the addition of several zeroth order Bessel functions $J_0(q_r r_i)$ where $r_i$ is the sharp peak position in the n(r) plot. As the nearest peptide-peptide distance is ~10 Å, this will give rise to a scattering peak at $q_r$~0.7 Å$^{-1}$ based on the shape of $J_0(x)$. However the peaks at other $r_i$ (next nearest neighbor distance for example) will also give rise to scattering peaks at other $q_r$ values (smaller than 0.7 Å$^{-1}$ due to the larger distance), such as the one at 0.3-0.4 Å$^{-1}$ in Fig. 3.10. When this peak is multiplied by the form factor of a single peptide, it is much stronger than the one at 0.7 Å$^{-1}$ due to the rapid decrease of the form factor. Since we do not see any scattering peak at 0.3-0.4 Å$^{-1}$, which is mainly due to the thermal fluctuations and the fluffy shape of the peptide, there is no reason why we should be able to see the scattering peak at $q_r$~0.7 Å$^{-1}$ based on the well defined peptide-peptide distance within a bundle.

### 6.5.2 Surface cluster model

The second possibility is the surface cluster model. Using a monolayer configuration, Ionov et al. [49] reported a 2-D monoclinic crystalline lattice where Alm peptides form a

planar structure parallel to the air/water interface as shown in Fig. 6.11. The (reciprocal) primitive vectors have been shown in chapter 4.

$$\begin{aligned} a_1 &= [a, 0] & a_2 &= [b\cos(\gamma), b\sin(\gamma)] \\ b_1 &= [\frac{1}{a}, -\frac{\cot(\gamma)}{a}] & b_2 &= [0, \frac{1}{b\sin(\gamma)}] \end{aligned} \tag{6.4}$$

where a is the diameter (~10Å) and b is the length of the peptide (~30Å). The peak positions in the reciprocal space for [H, K]=[1, 0] and [0, 1] are

$$\begin{aligned} q_r[1, 0] &= 2\pi\sqrt{\left(\frac{1}{a}\right)^2 + \left(-\frac{\cot(\gamma)}{a}\right)^2} \\ q_r[0, 1] &= \frac{2\pi}{b\sin(\gamma)} \end{aligned} \tag{6.5}$$

By simple calculation we find that for [H, K]=[1,0]=0.7Å$^{-1}$, γ needs to be 63.8$^{o}$. This gives [0, 1]=0.23 Å$^{-1}$. However, we did not see any scattering peak at this position which makes the surface model incorrect. Aside from that, there are other reasons that make the surface model unlikely. The first one is that oriented circular dichroism (OCD) measurement showed that at high peptide concentration all of the peptides are transmembrane (TM) [138]. Our recent paper also showed that the peptides are transmembrane at the peptide concentration used in this thesis [97]. The second reason is that when there are large amounts of peptides lying at the surface of the lipid bilayer, the lipid bilayer integrity will be disrupted. The disruption will be reflected in the lipid chain wide angle scattering which becomes very weak as the disruption becomes larger [135, 136]. However our data in Fig. 6.1 and Fig. 6.3 show that the chain wide angle scattering is well preserved even at high peptide concentration. This eliminates the possibility of the surface cluster model as the source of peak 2.

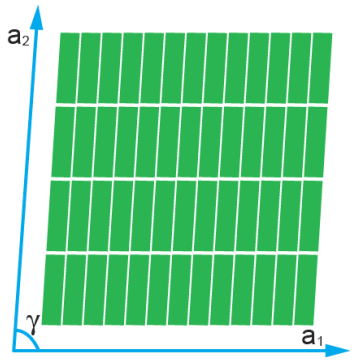


Figure 6.11: Top view of the 2-D monoclinic crystalline lattice of Alm peptides at the air/water interface.

### 6.5.3 Transmembrane cluster model

The main reason for the failure of the bundle model in Fig. 6.6B to predict peak 2 is because there is more than one characteristic distance within the bundle other than the nearest peptide-peptide distance. A possible picture that only involves one characteristic distance, the peptide diameter, is shown in Fig. 6.12 where the peptides form a hexagonally packed cluster. In this model, the peptides pack in a very similar way to lipid chains which are known to cause chain wide angle scattering as shown in Fig. 6.1 and Fig. 6.3. Then the peptide cluster can also result in similar wide angle scattering except at a different position, $q_r = \frac{2\pi}{d \times \cos(30^o)}$ =0.73 Å$^{-1}$, where d=10 Å is the diameter of the peptide.

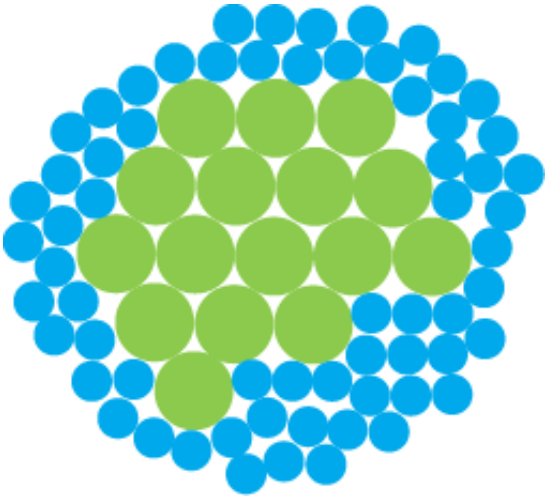

Figure 6.12: Top view of hexagonally packed peptide cluster in a lipid bilayer (green circles represent Alm monomers and blue circles represent hydrocarbon chains).

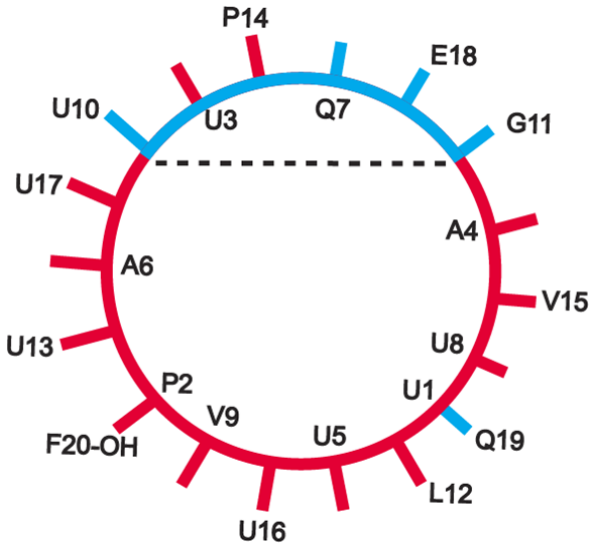


Figure 6.13: Helical wheel of the Alm peptide based on its crystal structure. The dashed line separates the hydrophobic (below the line) and the hydrophilic (above the line) faces.

Although this model fits the x-ray data, it is unusual in the peptide literature. We next consider the driving forces that have been supposed to favor the traditional bundle

formation, and we show that these same forces could also be involved in creating the cluster in Fig. 6.12. Figure 6.13A shows the helical wheel of the Alm peptide based on its crystal structure [32]. Most of the polar groups (the $Gln^{7}$ and $Glu^{18}$ side chains and the carbonyl oxygen atoms of $Aib^{10}$ and $Gly^{11}$) lie along a strip parallel to the helical axis in the tertiary structure indicated by the portion above the dashed line. This strip occupies ~1/3 of the circumference of the peptide. The amphiphilic structure of Fig. 6.13A favors the peptide bundle configuration compared to a non-clustered monomer because the hydrophilic strips face the water pore and the hydrophobic portion of the circumference faces the lipids. Indeed, almost all of the proposed Alm pore structures applied this configuration [32, 139]. Figure 6.14 shows two building blocks that can form hexagonal packing structure mimicking Fig.6.12 that has all the hydrophilic residues facing each other (any combination of the two blocks can form hexagonal packing structures with a hydrophobic circumference and hydrophilic residues facing each other; other orientations of the hexagonal cluster can be obtained by rotating the clusters formed by these two blocks).

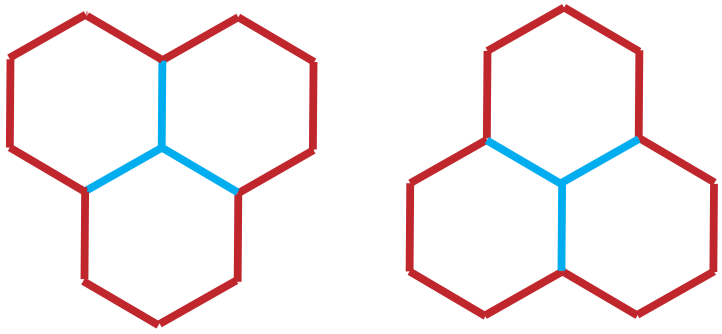

Figure 6.14: Two building blocks that can form hexagonal packing structures with hydrophilic residues facing each other.

In chapter 4 we confirmed that peak 1 is due to the Alm bundle structure. Then in the current model we are assuming that the peptide cluster is in equilibrium with peptide bundles. This model not only explains the source of peak 1 and peak 2, but also explains the result at the end of chapter 4 that a certain amount of peptides are not involved in bundle formation based on the model fitting (Qian et al. [24] also suggested that only ~30% of Alm is involved in bundle formation.).

Our peptide cluster model is also consistent with a recent MD simulation work combining coarse-grained (CG) and all-atom (AA) simulations [40]. The authors found that Alm peptides form large clusters spontaneously over a long time scale. First they distribute the TM peptides evenly in a DMPC lipid bilayer. After a ~150ns simulation, small clusters (2 to 3 peptides per cluster) were formed through peptide random diffusion. The small clusters continued to grow in size until only one large cluster existed after ~3.1μs (there are 25 peptides total in the simulation). One main source stabilizing the cluster configuration is through the H-bonding network of the $Gln^7$ residues as illustrated in Fig. 6.15. This mechanism is very similar to the proposed Alm bundle model by Fox and Richards [32] where the barrel-stave bundle is also stabilized through the H-bonding of the neighboring $Gln^7$ residues. The radial pair distribution function of the peptides in the cluster indicates that the peptides form either hexagonal packing or square packing with nearest neighboring distances ranging from 9 to 11Å based on two slightly different algorithms.

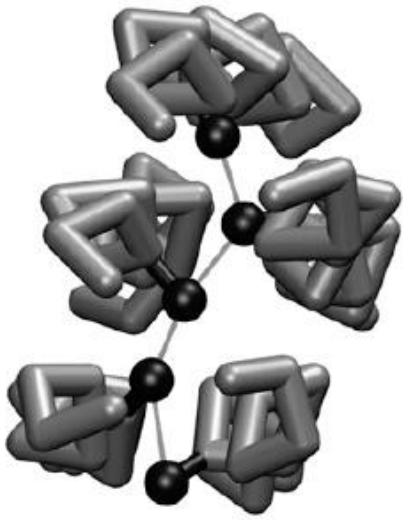

Figure 6.15: Example of clustering through H-bonding network of $Gln^7$ (black sphere) [40].

One experimental evidence for phase separation in a lipid multilayer system is the observation of a doublet lamellar repeat spacing D which has been applied to investigate the binary and ternary phase coexistence in lipid membranes [140-142]. Figure 6.16 shows an x-ray lamellar scattering pattern of Alm/DOPC (the lipid concentration in the aqueous dispersion is 25% by weight and the Alm concentration is $10^{-4}$ M) [143]. The splitting of the lamellar peaks is suggested by the arrows. The authors attributed the 63.4 Å peak to the peptide free lipid domains and the 60.3 Å peak to the domains where DOPC interacts with Alm peptides. Although their explanation of the two peaks can be argued in different ways, one conclusion that can be safely drawn is the existence of phase separation in Alm/DOPC system which is consistent with our model where Alm monomers aggregate together to form large clusters and phase separate from the rest of

the system.

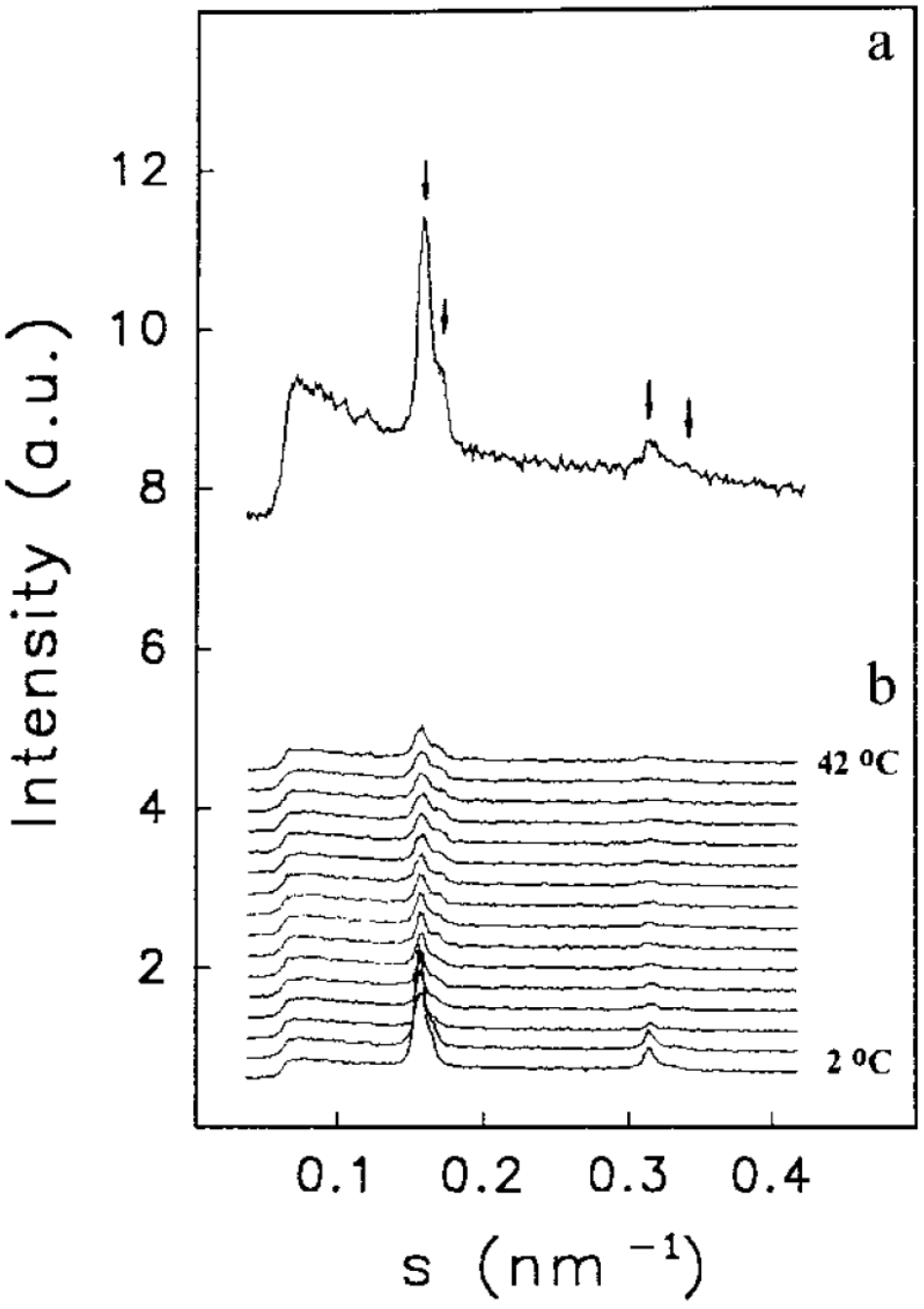


Figure 6.16: Lamellar scattering pattern of Alm/DOPC in aqueous dispersion obtained from Fig. 3 in [143] ($s=q/2\pi$).

## 6.6 Conclusions

In addition to the scattering (peak 1) due to the Alm bundle structure, we observed a second peak (peak 2) due to Alm incorporation. By comparing the position and the width of peak 2 from peak decomposition we found that its trend as a function of the peptide concentration and lipid type is different from the trend of peak1. Three models were proposed for the source of peak 2: the well defined peptide-peptide distance within the bundle model, the surface cluster model, and the transmembrane cluster. The first one fails because there are other well defined distances within the bundle which give rise to other scattering peaks with larger intensity which are not observed in our experiment. The second one fails because it disrupts the bilayer integrity in addition to a lot of missing peaks. It also disagrees with the OCD measurement which showed that at high peptide concentration Alm is perpendicular to the bilayer surface. Only the third one survives and it agrees with a recent MD simulation work as well as the doublet lamellar scattering peaks.

## 6.7 Appendix: Scattering from a helix

The main secondary structure of the Alm peptide in a hydrophobic environment is an α-helix as has been shown by both x-ray diffraction [32] and NMR spectrum [77, 139, 144] studies. By investigating Alm/lipid mixtures at very dehydrated conditions (lamellar repeat spacing D~50 Å), Spaar et al.[145] reported a broad peak at q~1.4 $Å^{-1}$ centered at the meridian ($q_z$=0). The authors claimed that this peak was due to the peptide helical structure with a broad tilt angle distribution. One complication of this peak is that the

chain wide angle scattering also appears at q~1.4 $Å^{-1}$. Our lab has observed that at dehydrated conditions, strong chain wide angle scattering can occur near the meridian. Their missing peak 1 and peak 2 are also hard to reconcile. Since our experimental data are more consistent with the canonical view of the peptide bundle structure, it is to our interest to check whether such a helical scattering peak is also present in our data.

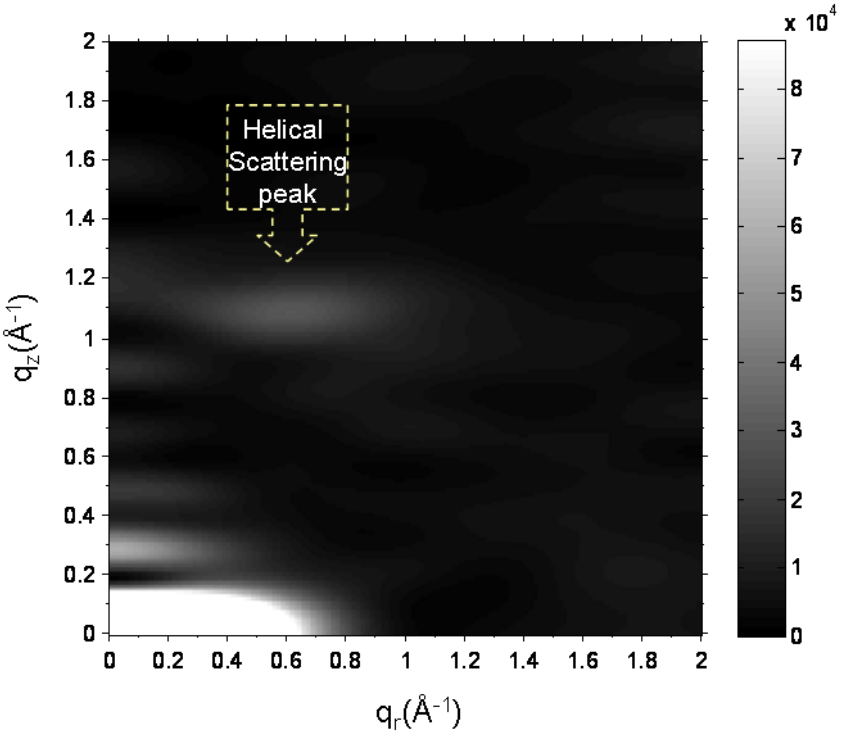


Figure 6.17: Form factor of an Alm monomer calculated from the coordinates in the protein data bank (1AMT.pdb).

Figure 6.17 shows the form factor of an Alm monomer obtained from crystallography study [32]. The scattering peak centered at ($q_r$, $q_z$)=(0.6, 1.1) $Å^{-1}$ due to the helical structure is observable. The helical radius $R_h$ and pitch P are related to the

helical peak position by the following equation [25] (assuming the scattering source is an ideal helix).

$$R_h = \frac{5\pi}{8q_r}, \qquad P = \frac{2\pi}{q_z} \tag{6.6}$$

A simple calculation shows that pitch P is 5.7 Å which corresponds very well to the helical structure and helical radius $R_h$ is of 3.2 Å. The smaller helical radius compared to the peptide steric radius (~5 Å) is mainly due to the side chain effect [25]. The main effort of this appendix is to explore whether a similar helical scattering peak is observable in our wide angle scattering region.

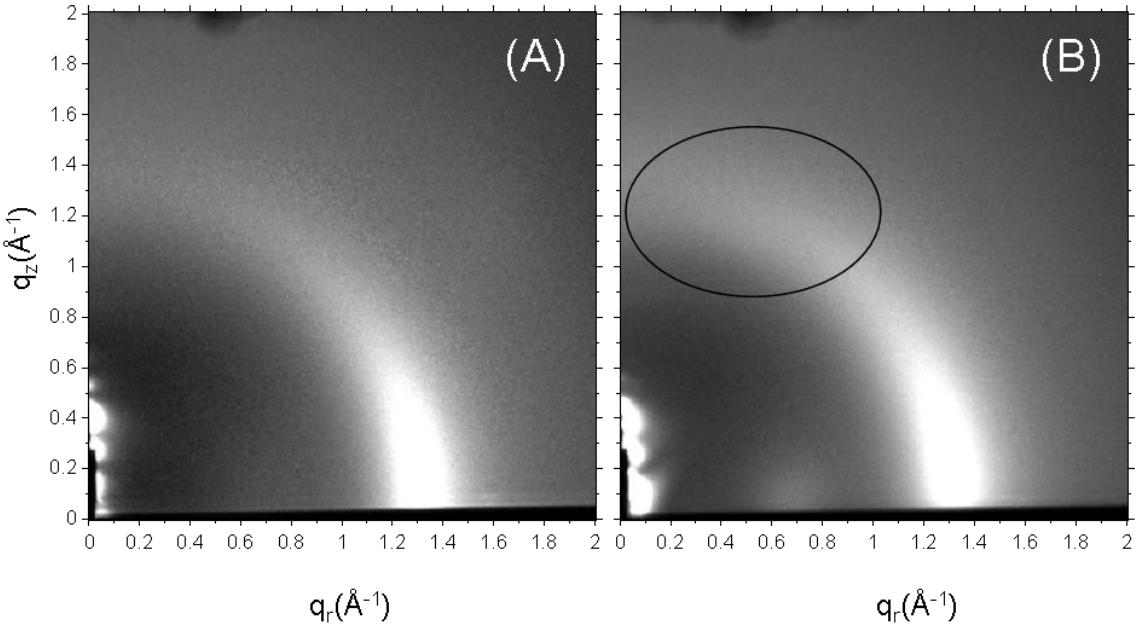


Figure 6.18: Background subtracted wide angle x-ray scattering ($\alpha$=0.2$^o$) images for (A) diC22:1PC and (B) Alm:diC22:1PC 1:10 at similar hydration conditions.

Figure 6.18 shows the wide angle scattering images for pure diC22:1PC (panel A) and Alm:diC22:1PC 1:10 (panel B) at similar hydration conditions using synchrotron x-ray beam line (G1 station) at CHESS. Contrast to [25], Fig. 6.18 shows that our chain wide angle scattering is well preserved upon peptide addition and it is much stronger than the scattering at the helical peak position. ([25] showed scattering on an arc centered at the meridian at q~1.4 $Å^{-1}$ which was much stronger than the chain wide angle scattering. They suggested that the weak chain scattering was due to the frustrated chain packing upon peptide insertion.).

However the scattering at the helical peak position indicated by the ellipse in Fig. 6.18B seems to be a bit stronger compared to the pure lipid in Fig. 6.18A. Figure 6.19 shows the subtraction of Fig. 6.18B by Fig. 6.18A. The strong scattering at small q corresponds to peak 1 and the satellite peaks in addition to some lamellar diffuse scattering due to the modified elastic property by Alm insertion [97]. Peak 2 at $q_r$ ~0.7 $Å^{-1}$ is clearly shown in the subtracted image. Aside from these peaks a broad peak near the helical peak position is observable, although by changing the scaling factor between Fig. 6.18A and B the angular distribution of the remaining scattering can be made different. Unlike [25], the broad peak in Fig. 6.19 is not centered at the meridian. The intersection of the two solid lines indicates the approximate center of this broad peak. Its position is ($q_r$, $q_z$)≈(0.5, 1.1) $Å^{-1}$, corresponding to helical radius $R_h$=3.9 Å and pitch P=5.7 Å based on equation (6.6). Our similar helical pitch and a bit larger helical radius compared with the values determined from the crystal structure indicate that the helical

structure of the Alm peptide in lipid membranes is quite similar to the crystal structure.

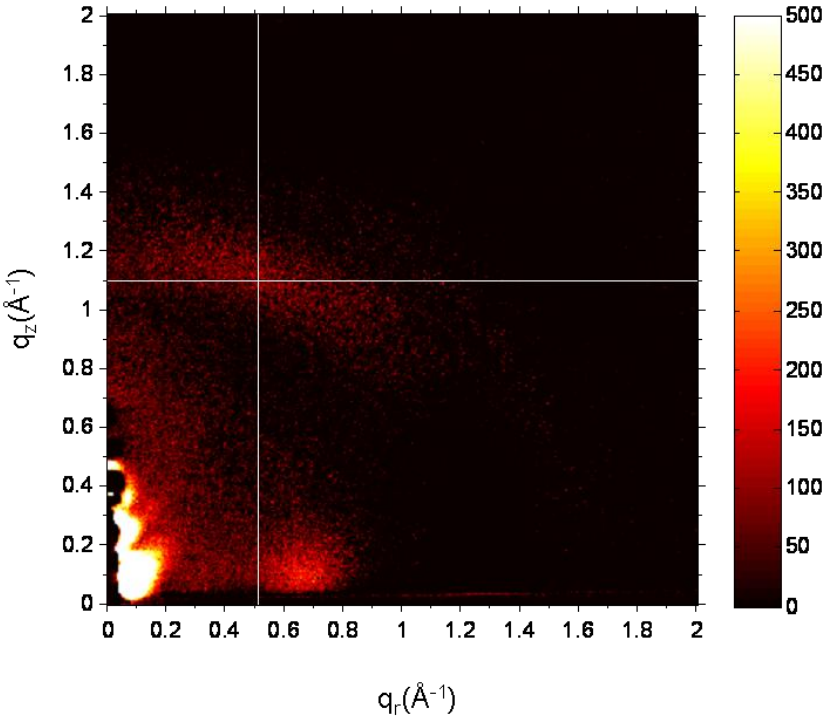


Figure 6.19: Subtraction of Fig. 6.18B by Fig. 6.18A. The intersection of the two solid lines indicates the approximate center of the broad peaks.

# Chapter 7

## Conclusions and future directions

Many experimental results have provided insights into the mechanisms through which lipid membranes affect integral protein channel activity [146-148]. Our result of the larger Alm bundle in a thicker lipid model membrane sheds extra light on the importance of lipid compositions. One way to test our hypothesis of hydrophobic matching on peptide bundle size distribution is to investigate the bundle size in other lipids with a much different hydrophobic thickness such as DLPC which is thinner than DOPC by 6 Å [88]. Another way to check our hypothesis is to add cholesterol molecules to a pure lipid model membrane. By varying the cholesterol concentration, the membrane thickness can be modified [118]. The relationship between the bundle size and the cholesterol concentration can then be investigated.

Other mechanisms can also be examined by varying lipid compositions. Lipid bilayer thickness measurements have shown that the bilayer thickness is very close for diC22:1PC and SOPC:Chol (1:1) [118]. However, the area stretch modulus $K_A$ is very different, ~260 mN/m and 1000 mN/m respectively [119, 130]. The relationship between the bundle size and the area stretch modulus can then be investigated. For the monolayer spontaneous curvature effect, because DOPC and DOPE have the same chain, the bundle size can be compared in these two lipids.

Our peptide hexagonal packing cluster model in chapter 6 was introduced to explain the diffuse like scattering peak at $q_r$ ~0.7Å$^{-1}$. The observed phase separation based on lamellar peak splitting [143] and large aggregate formation [40] in MD simulations are consistent with our model where peptide clusters are in equilibrium with peptide bundles. There are other methods to directly visualize such large peptide clusters. Figure 7.1 shows a fluorescence microscopy image of Alm in a DOPE monolayer. The dark region corresponds to peptide aggregates where the fluorescent probe is insoluble. Discrete Alm domains have also been observed in a DMPC monolayer by using Brewster angle microscopy (BAM) [149]. However, unlike the bilayer configuration, the N-terminal segment needs to be exposed to the air if the peptide adopts a TM conformation which might be too energetically expensive. Indeed, x-ray scattering indicates that the peptide adopts a parallel orientation at the air/water interface [49]. An ideal system for such TM cluster visualization is the GUV system which has been broadly applied to investigate model membrane phase separation [150, 151]. By utilizing similar fluorescent probes as in Fig. 7.1, large TM peptide clusters can be visualized if they exist.

Another adventure would be to quantitate the relative intensity in peak 1 and peak 2 as a function of Alm concentration in order to determine the equilibrium constant between bundles (peak 1) and clusters (peak 2).

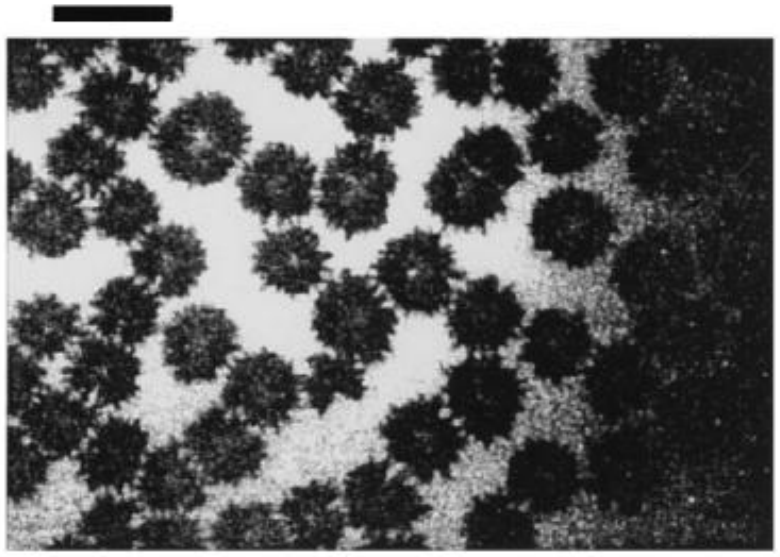

Figure 7.1: Fluorescence microscopy image of Alm in a DOPE monolayer (image was taken from [49]). The bar corresponds to 50μm. The bright region corresponds to the fluorescent probe which is soluble in fluid DOPE monolayer. The peptide in aqueous phase is ~$10^{-7}$ M.

# References


[1] Phillips, R., T. Ursell, P. Wiggins, and P. Sens. *Emerging roles for lipids in shaping membrane-protein function.* Nature, 2009. **459**(7245): p. 379-385.

[2] Marsh, D., *Protein modulation of lipids, and vice-versa, in membranes.* Biochim Biophys Acta, 2008. **1778**(7-8): p. 1545-1575.

[3] Andersen, O.S. and R.E. Koeppe, 2nd. *Bilayer thickness and membrane protein function: an energetic perspective.* Annu Rev Biophys Biomol Struct, 2007. **36**: p. 107-130.

[4] Nielsen, C., M. Goulian, and O.S. Andersen. *Energetics of inclusion-induced bilayer deformations.* Biophysical Journal, 1998. **74**(4): p. 1966-1983.

[5] Huang, H.W., *Deformation free energy of bilayer membrane and its effect on gramicidin channel lifetime.* Biophysical Journal, 1986. **50**(6): p. 1061-1070.

[6] Marsh, D., *Energetics of hydrophobic matching in lipid-protein interactions.* Biophys J, 2008. **94**(10): p. 3996-4013.

[7] McIntosh, T.J. and S.A. Simon. *Roles of bilayer material properties in function and distribution of membrane proteins.* Annu Rev Biophys Biomol Struct, 2006. **35**: p. 177-198.

[8] Mueller, P. and D.O. Rudin. *Action potentials induced in biomolecular lipid membranes.* Nature, 1968. **217**(5130): p. 713-9.

[9] Eisenberg, M., J.E. Hall, and C.A. Mead. *The nature of the voltage-dependent conductance induced by alamethicin in black lipid membranes.* Journal of Membrane Biology, 1973. **14**(2): p. 143-176.

[10] Gordon, L.G. and D.A. Haydon. *Potential-dependent conductances in lipid membranes containing alamethicin.* Philos Trans R Soc Lond B Biol Sci, 1975. **270**(908): p. 433-47.

[11] Lau, A.L. and S.I. Chan. *Voltage-induced formation of alamethicin pores in lecithin bilayer vesicles.* Biochemistry, 1976. **15**(12): p. 2551-5.

[12] Hall, J.E., I. Vodyanoy, T.M. Balasubramanian, and G.R. Marshall. *Alamethicin - a Rich Model for Channel Behavior.* Biophysical Journal, 1984. **45**(1): p. 233-247.

[13] Woolley, G.A. and C.M. Deber. *A Lipid Vesicle System for Probing Voltage-Dependent Peptide Lipid Interactions - Application to Alamethicin*

*Channel Formation.* Biopolymers, 1989. **28**(1): p. 267-272.

[14] Archer, S.J. and D.S. Cafiso. *Voltage-Dependent Conductance for Alamethicin in Phospholipid-Vesicles - a Test for the Mechanism of Gating.* Biophysical Journal, 1991. **60**(2): p. 380-388.

[15] Hanke, W. and G. Boheim. *The lowest conductance state of the alamethicin pore.* Biochim Biophys Acta, 1980. **596**(3): p. 456-62.

[16] Sansom, M.S., *The biophysics of peptide models of ion channels.* Prog Biophys Mol Biol, 1991. **55**(3): p. 139-235.

[17] Mak, D.O. and W.W. Webb. *Two classes of alamethicin transmembrane channels: molecular models from single-channel properties.* Biophysical Journal, 1995. **69**(6): p. 2323-36.

[18] Keller, S.L., S.M. Bezrukov, S.M. Gruner, M.W. Tate, I. Vodyanoy, and V.A. Parsegian. *Probability of Alamethicin Conductance States Varies with Nonlamellar Tendency of Bilayer Phospholipids.* Biophysical Journal, 1993. **65**(1): p. 23-27.

[19] Dan, N. and S.A. Safran. *Effect of lipid characteristics on the structure of transmembrane proteins.* Biophysical Journal, 1998. **75**(3): p. 1410-1414.

[20] Cantor, R.S., *Size distribution of barrel-stave aggregates of membrane peptides: influence of the bilayer lateral pressure profile.* Biophysical Journal, 2002. **82**(5): p. 2520-2525.

[21] Sperotto, M.M., *A theoretical model for the association of amphiphilic transmembrane peptides in lipid bilayers.* European Biophysics Journal with Biophysics Letters, 1997. **26**(5): p. 405-416.

[22] He, K., S.J. Ludtke, D.L. Worcester, and H.W. Huang. *Neutron scattering in the plane of membranes: structure of alamethicin pores.* Biophysical Journal, 1996. **70**(6): p. 2659-2666.

[23] He, K., S.J. Ludtke, H.W. Huang, and D.L. Worcester. *Antimicrobial peptide pores in membranes detected by neutron in-plane scattering.* Biochemistry, 1995. **34**(48): p. 15614-8.

[24] Qian, S., W. Wang, L. Yang, and H.W. Huang. *Structure of the alamethicin pore reconstructed by x-ray diffraction analysis.* Biophysical Journal, 2008. **94**(9): p. 3512-3522.

[25] Constantin, D., G. Brotons, A. Jarre, C. Li, and T. Salditt. *Interaction of alamethicin pores in DMPC bilayers.* Biophysical Journal, 2007. **92**(11): p. 3978-3987.

[26] Sansom, M.S., *Structure and function of channel-forming peptaibols.* Q Rev Biophys, 1993. **26**(4): p. 365-421.

[27] Woolley, G.A. and B.A. Wallace. *Model ion channels: gramicidin and alamethicin.* Journal of Membrane Biology, 1992. **129**(2): p. 109-136.

[28] Cafiso, D.S., *Alamethicin: a peptide model for voltage gating and protein-membrane interactions.* Annu Rev Biophys Biomol Struct, 1994. **23**: p. 141-65.

[29] Latorre, R. and O. Alvarez. *Voltage-dependent channels in planar lipid bilayer membranes.* Physiological Reviews, 1981. **61**(1): p. 77-150.

[30] Bechinger, B., *Structure and functions of channel-forming peptides: Magainins, cecropins, melittin and alamethicin.* Journal of Membrane Biology, 1997. **156**(3): p. 197-211.

[31] Duclohier, H. and H. Wroblewski. *Voltage-dependent pore formation and antimicrobial activity by alamethicin and analogues.* Journal of Membrane Biology, 2001. **184**(1): p. 1-12.

[32] Fox, R.O. and F.M. Richards. *A Voltage-Gated Ion Channel Model Inferred from the Crystal-Structure of Alamethicin at 1.5-a Resolution.* Nature, 1982. **300**(5890): p. 325-330.

[33] Fox, R.O. and F.M. Richards. *The Crystal-Structure of Alamethicin.* Biophysical Journal, 1982. **37**(2): p. A179-a179.

[34] Banerjee, U., F.P. Tsui, T.N. Balasubramanian, G.R. Marshall, and S.I. Chan. *Structure of Alamethicin in Solution - One-Dimensional and Two-Dimensional H-1 Nuclear Magnetic-Resonance Studies at 500-Mhz.* Journal of Molecular Biology, 1983. **165**(4): p. 757-775.

[35] Baumann, G. and P. Mueller. *A molecular model of membrane excitability.* Journal of Supramolecular Structure, 1974. **2**(5-6): p. 538-557.

[36] Als-Nielsen, J. and D. McMorrow, *Elements of modern x-ray physics*. 2001.

[37] Pan, J., S. Tristram-Nagle, N. Kucerka, and J.F. Nagle. *Temperature dependence of structure, bending rigidity, and bilayer interactions of dioleoylphosphatidylcholine bilayers.* Biophysical Journal, 2008. **94**(1): p. 117-124.

[38] Yang, L., T.M. Weiss, R.I. Lehrer, and H.W. Huang. *Crystallization of antimicrobial pores in membranes: magainin and protegrin.* Biophysical Journal, 2000. **79**(4): p. 2002-2009.

[39] Salditt, T., C.H. Li, and A. Spaar. *Structure of antimicrobial peptides and lipid membranes probed by interface-sensitive X-ray scattering.* Biochimica Biophysica Acta, 2006. **1758**(9): p. 1483-1498.

[40] Thøgersen, L., B. Schiøtt, T. Vosegaard, N.C. Nielsen, and E. Tajkhorshid. *Peptide Aggregation and Pore Formation in a Lipid Bilayer: A Combined Coarse-Grained and All Atom Molecular Dynamics Study.* Biophysical Journal, 2008. **95**(9): p. 4337-4347.

[41] Archer, S.J., J.F. Ellena, and D.S. Cafiso. *Dynamics and Aggregation of the Peptide Ion Channel Alamethicin - Measurements Using Spin-Labeled Peptides.* Biophysical Journal, 1991. **60**(2): p. 389-398.

[42] Barranger-Mathys, M. and D.S. Cafiso. *Collisions between Helical Peptides in Membranes Monitored Using Electron-Paramagnetic-Resonance - Evidence That Alamethicin Is Monomeric in the Absence of a Membrane-Potential.* Biophysical Journal, 1994. **67**(1): p. 172-176.

[43] Marsh, D., M. Jost, C. Peggion, and C. Toniolo. *TOAC spin labels in the backbone of alamethicin: EPR studies in lipid membranes.* Biophysical Journal, 2007. **92**(2): p. 473-481.

[44] Salnikov, E.S., M. De Zotti, F. Formaggio, X. Li, C. Toniolo, J.D.J. O'Neil, J. Raap, S.A. Dzuba, and B. Bechinger. *Alamethicin Topology in Phospholipid Membranes by Oriented Solid-state NMR and EPR Spectroscopies: a Comparison.* Journal of Physical Chemistry B, 2009. **113**(10): p. 3034-3042.

[45] de Kruijff, B., J.A. Killian, D.N. Ganchev, H.A. Rinia, and E. Sparr. *Striated domains: self-organizing ordered assemblies of transmembrane alpha-helical peptides and lipids in bilayers.* Biol Chem, 2006. **387**(3): p. 235-41.

[46] Rinia, H.A., J.W. Boots, D.T. Rijkers, R.A. Kik, M.M. Snel, R.A. Demel, J.A. Killian, J.P. van der Eerden, and B. de Kruijff. *Domain formation in phosphatidylcholine bilayers containing transmembrane peptides: specific effects of flanking residues.* Biochemistry, 2002. **41**(8): p. 2814-24.

[47] Rinia, H.A., R.A. Kik, R.A. Demel, M.M. Snel, J.A. Killian, J.P. van Der Eerden, and B. de Kruijff. *Visualization of highly ordered striated domains induced by transmembrane peptides in supported phosphatidylcholine bilayers.* Biochemistry, 2000. **39**(19): p. 5852-8.

[48] Mou, J., D.M. Czajkowsky, and Z. Shao. *Gramicidin A aggregation in supported gel state phosphatidylcholine bilayers.* Biochemistry, 1996. **35**(10): p. 3222-6.

[49] Ionov, R., A. El-Abed, A. Angelova, M. Goldmann, and P. Peretti. *Asymmetrical ion-channel model inferred from two-dimensional crystallization of a peptide*

*antibiotic*. Biophysical Journal, 2000. **78**(6): p. 3026-3035.

[50] Volinsky, R., S. Kolusheva, A. Berman, and R. Jelinek. *Investigations of antimicrobial peptides in planar film systems.* Biochim Biophys Acta, 2006. **1758**(9): p. 1393-407.

[51] Blaurock, A.E. and W. Stoeckenius. *Structure of the purple membrane.* Nat New Biol, 1971. **233**(39): p. 152-5.

[52] Michel, H., D. Oesterhelt, and R. Henderson. *Orthorhombic two-dimensional crystal form of purple membrane.* Proc Natl Acad Sci U. S. A., 1980. **77**(1): p. 338-342.

[53] Sabra, M.C., J.C. Uitdehaag, and A. Watts. *General model for lipid-mediated two-dimensional array formation of membrane proteins: application to bacteriorhodopsin.* Biophysical Journal, 1998. **75**(3): p. 1180-1188.

[54] Meyer, C.E. and F. Reusser. *A polypeptide antibacterial agent isolated from Trichoderma viride.* Experientia, 1967. **23**(2): p. 85-6.

[55] Izadpanah, A. and R.L. Gallo. *Antimicrobial peptides.* Journal of American Academy of Dermatology, 2005. **52**(3 Pt 1): p. 381-390.

[56] Radek, K. and R. Gallo. *Antimicrobial peptides: natural effectors of the innate immune system.* Semin Immunopathol, 2007. **29**(1): p. 27-43.

[57] Matsuzaki, K., O. Murase, N. Fujii, and K. Miyajima. *An antimicrobial peptide, magainin 2, induced rapid flip-flop of phospholipids coupled with pore formation and peptide translocation.* Biochemistry, 1996. **35**(35): p. 11361-11368.

[58] Ludtke, S.J., K. He, W.T. Heller, T.A. Harroun, L. Yang, and H.W. Huang. *Membrane pores induced by magainin.* Biochemistry, 1996. **35**(43): p. 13723-8.

[59] Li, C. and T. Salditt. *Structure of magainin and alamethicin in model membranes studied by x-ray reflectivity.* Biophysical Journal, 2006. **91**(9): p. 3285-3300.

[60] Payne, J.W., R. Jakes, and B.S. Hartley. *The primary structure of alamethicin.* Biochem J, 1970. **117**(4): p. 757-66.

[61] Jung, G. and N. Dubischar. *Conformational changes of alamethicin induced by solvent and temperature. A 13C-NMR and circular-dichroism study.* Eur J Biochem, 1975. **54**(2): p. 395-409.

[62] Martin, D.R. and R.J. Williams. *The nature and function of alamethicin.* Biochem Soc Trans, 1975. **3**(1): p. 166-7.

[63] Pandey, R.C., J.C. Cook, and K.L. Rinehart. *Peptaibophol Antibiotics .3.*

*High-Resolution and Field Desorption Mass-Spectrometry Studies and Revised Structures of Alamethicin-I and Alamethicin-Ii.* Journal of the American Chemical Society, 1977. **99**(26): p. 8469-8483.

[64] Gisin, B.F., S. Kobayashi, and J.E. Hall. *Synthesis of a 19-Residue Peptide with Alamethicin-Like Activity.* Proceedings of the National Academy of Sciences of the United States of America, 1977. **74**(1): p. 115-119.

[65] McMullen, A.I., *Some properties of the ion-gating polypeptide alamethicin.* Biochem J, 1970. **119**(3): p. 10P-11P.

[66] McMullen, A.I. and J.A. Stirrup. *The aggregation of alamethicin.* Biochim Biophys Acta, 1971. **241**(3): p. 807-814.

[67] Kirschbaum, J., C. Krause, R.K. Winzheimer, and H. Bruckner. *Sequences of alamethicins F30 and F50 reconsidered and reconciled.* Journal of Peptide Science, 2003. **9**(11-12): p. 799-809.

[68] Marshall, G.R. and H.E. Bosshard. *Angiotensin-Ii - Studies on Biologically-Active Conformation.* Circulation Research, 1972. **31**(3): p. I143-150.

[69] Burgess, A.W. and S.J. Leach. *An obligatory alpha-helical amino acid residue.* Biopolymers, 1973. **12**(11): p. 2599-605.

[70] Balaram, P., *Peptides as Bioorganic Models.* Proceedings of the Indian Academy of Sciences-Chemical Sciences, 1984. **93**(4): p. 703-717.

[71] Karle, I.L. and P. Balaram. *Structural characteristics of alpha-helical peptide molecules containing Aib residues.* Biochemistry, 1990. **29**(29): p. 6747-56.

[72] Yee, A.A., K. Marat, and J.D.J. ONeil. *The interactions with solvent, heat stability, and C-13-labelling of alamethicin, an ion-channel-forming peptide.* European Journal of Biochemistry, 1997. **243**(1-2): p. 283-291.

[73] Banerjee, U. and S.I. Chan. *Structure of alamethicin in solution: nuclear magnetic resonance relaxation studies.* Biochemistry, 1983. **22**(15): p. 3709-13.

[74] Esposito, G., J.A. Carver, J. Boyd, and I.D. Campbell. *High-resolution 1H NMR study of the solution structure of alamethicin.* Biochemistry, 1987. **26**(4): p. 1043-50.

[75] Yee, A.A. and J.D.J. Oneil. *Uniform N-15 Labeling of a Fungal Peptide - the Structure and Dynamics of an Alamethicin by N-15 and H-1-Nmr Spectroscopy.* Biochemistry, 1992. **31**(12): p. 3135-3143.

[76] Kelsh, L.P., J.F. Ellena, and D.S. Cafiso. *Determination of the Molecular-Dynamics of Alamethicin Using C-13 Nmr - Implications for the*

*Mechanism of Gating of a Voltage-Dependent Channel*. Biochemistry, 1992. **31**(22): p. 5136-5144.

[77] Franklin, J.C., J.F. Ellena, S. Jayasinghe, L.P. Kelsh, and D.S. Cafiso. *Structure of Micelle-Associated Alamethicin from H-1-Nmr - Evidence for Conformational Heterogeneity in a Voltage-Gated Peptide.* Biochemistry, 1994. **33**(13): p. 4036-4045.

[78] Schwarz, G. and P. Savko. *Structural and dipolar properties of the voltage-dependent pore former alamethicin in octanol/dioxane.* Biophysical Journal, 1982. **39**(2): p. 211-219.

[79] Yantorno, R., S. Takashima, and P. Mueller. *Dipole moment of alamethicin as related to voltage-dependent conductance in lipid bilayers.* Biophysical Journal, 1982. **38**(2): p. 105-110.

[80] Molle, G., J.Y. Dugast, G. Spach, and H. Duclohier. *Ion channel stabilization of synthetic alamethicin analogs by rings of inter-helix H-bonds.* Biophysical Journal, 1996. **70**(4): p. 1669-1675.

[81] Breed, J., P.C. Biggin, I.D. Kerr, O.S. Smart, and M.S.P. Sansom. *Alamethicin channels - modelling via restrained molecular dynamics simulations.* Biochimica Biophysica Acta, 1997. **1325**(2): p. 235-249.

[82] Tieleman, D.P., H.J.C. Berendsen, and M.S.P. Sansom. *An alamethicin channel in a lipid bilayer: Molecular dynamics simulations.* Biophysical Journal, 1999. **76**(4): p. 1757-1769.

[83] Jayasinghe, S., M. Barranger-Mathys, J.F. Ellena, C. Franklin, and D.S. Cafiso. *Structural features that modulate the transmembrane migration of a hydrophobic peptide in lipid vesicles.* Biophysical Journal, 1998. **74**(6): p. 3023-3030.

[84] Vodyanoy, I., J.E. Hall, and T.M. Balasubramanian. *Alamethicin-induced current-voltage curve asymmetry in lipid bilayers.* Biophysical Journal, 1983. **42**(1): p. 71-82.

[85] Tristram-Nagle, S., R. Zhang, R.M. Suter, C.R. Worthington, W.J. Sun, and J.F. Nagle. *Measurement of chain tilt angle in fully hydrated bilayers of gel phase lecithins.* Biophysical Journal, 1993. **64**(4): p. 1097-1109.

[86] Tristram-Nagle, S., *Preparation of oriented, fully hydrated lipid samples for structure determination using x-ray scattering*. Methods in molecular biology 400: methods in membrane lipids, ed. A. Dopico. 2007, Totowa, N.J.: Humana Press. 63-75.

[87] Katsaras, J., *Highly aligned lipid membrane systems in the physiologically*

*relevant "excess water" condition.* Biophysical Journal, 1997. **73**(6): p. 2924-2929.

[88] Kučerka, N., Y. Liu, N. Chu, H.I. Petrache, S. Tristram-Nagle, and J.F. Nagle. *Structure of fully hydrated fluid phase DMPC and DLPC lipid bilayers using X-ray scattering from oriented multilamellar arrays and from unilamellar vesicles.* Biophysical Journal, 2005. **88**(4): p. 2626-2637.

[89] Mills, T.T., *Wide angle x-ray scattering probes chain order and indentifies liquid-liquid phase coexistence in oriented lipid membranes*. 2008, Cornell University: Ithaca. p. 294.

[90] Barna, S.L., M.W. Tate, S.M. Gruner, and E.F. Eikenberry. *Calibration procedures for charge-coupled device x-ray detectors.* Review of Scientific Instruments, 1999. **70**(7): p. 2927-2934.

[91] Mills, T.T., G.E. Toombes, S. Tristram-Nagle, D.M. Smilgies, G.W. Feigenson, and J.F. Nagle. *Order parameters and areas in fluid-phase oriented lipid membranes using wide angle X-ray scattering.* Biophysical Journal, 2008. **95**(2): p. 669-681.

[92] Warren, B.E., *X-ray diffraction*. 1969, New York: Dover Publications, INC.

[93] Huang, T.C., H. Toraya, T.N. Blanton, and Y. Wu. *X-Ray-Powder Diffraction Analysis of Silver Behenate, a Possible Low-Angle Diffraction Standard.* Journal of Applied Crystallography, 1993. **26**: p. 180-184.

[94] Yang, L., T.A. Harroun, W.T. Heller, T.M. Weiss, and H.W. Huang. *Neutron off-plane scattering of aligned membranes. I. Method Of measurement.* Biophysical Journal, 1998. **75**(2): p. 641-645.

[95] Metropolis, N., A.W. Rosenbluth, M.N. Rosenbluth, A.H. Teller, and E. Teller. *Equation of State Calculations by Fast Computing Machines.* Journal of Chemical Physics, 1953. **21**(6): p. 1087-1092.

[96] Yang, L., T.M. Weiss, T.A. Harroun, W.T. Heller, and H.W. Huang. *Supramolecular structures of peptide assemblies in membranes by neutron off-plane scattering: method of analysis.* Biophysical Journal, 1999. **77**(5): p. 2648-2656.

[97] Pan, J., D.P. Tieleman, J.F. Nagle, N. Kucerka, and S. Tristram-Nagle. *Alamethicin in lipid bilayers: Combined use of X-ray scattering and MD simulations.* Biochim et Biophys Acta, 2009. **1788**(6): p. 1387-1397.

[98] Kučerka, N., S. Tristram-Nagle, and J.F. Nagle. *Structure of fully hydrated fluid phase lipid bilayers with monounsaturated chains.* Journal of Membrane Biology,

2005. **208**(3): p. 193-202.

[99] Bowman, F., *Introduction to Bessel functions*. 1958, New York.

[100] Gaskill, J.D., *Linear systems, Fourier transforms, and optics*. 1978, New York: Wiley.

[101] McQuarrie, D.A., *Statistical mechanics*. 1976, New York: Harper & Row.

[102] Hansen, J.P. and I.R. McDonald, *Theory of simple liquids*. 1976, New York: Academic press. INC.

[103] Rosenfeld, Y., *Free-Energy Model for the Inhomogeneous Hard-Sphere Fluid in D-Dimensions - Structure Factors for the Hard-Disk (D = 2) Mixtures in Simple Explicit Form.* Physical Review A, 1990. **42**(10): p. 5978-5989.

[104] Reif, F., *Fundamentals of statistical and thermal physics*. 1965: McGraw-Hill, Inc.

[105] He, K., S.J. Ludtke, Y. Wu, and H.W. Huang. *X-ray scattering with momentum transfer in the plane of membrane. Application to gramicidin organization.* Biophysical Journal, 1993. **64**(1): p. 157-162.

[106] Zhang, R., R.M. Suter, and J.F. Nagle. *Theory of the structure factor of lipid bilayers.* Physical Review E, 1994. **50**(6): p. 5047-5060.

[107] Lyatskaya, Y., Y. Liu, S. Tristram-Nagle, J. Katsaras, and J.F. Nagle. *Method for obtaining structure and interactions from oriented lipid bilayers.* Physical Review E, 2001. **63**(1 Pt 1): p. 011907.

[108] Liu, Y. and J.F. Nagle. *Diffuse scattering provides material parameters and electron density profiles of biomembranes.* Physical Review E, 2004. **69**(4 Pt 1): p. 040901.

[109] Tristram-Nagle, S., Y. Liu, J. Legleiter, and J.F. Nagle. *Structure of gel phase DMPC determined by X-ray diffraction.* Biophysical Journal, 2002. **83**(6): p. 3324-3335.

[110] Edholm, O. and J.F. Nagle. *Areas of molecules in membranes consisting of mixtures.* Biophysical Journal, 2005. **89**(3): p. 1827-1832.

[111] Lagüe, P., M.J. Zuckermann, and B. Roux. *Lipid-mediated interactions between intrinsic membrane proteins: a theoretical study based on integral equations.* Biophysical Journal, 2000. **79**(6): p. 2867-2879.

[112] Lagüe, P., M.J. Zuckermann, and B. Roux. *Lipid-mediated interactions between intrinsic membrane proteins: dependence on protein size and lipid composition.*

Biophysical Journal, 2001. **81**(1): p. 276-284.

[113] Tieleman, D.P., B. Hess, and M.S.P. Sansom. *Analysis and evaluation of channel models: Simulations of alamethicin.* Biophysical Journal, 2002. **83**(5): p. 2393-2407.

[114] Tristram-Nagle, S., H.I. Petrache, and J.F. Nagle. *Structure and interactions of fully hydrated dioleoylphosphatidylcholine bilayers.* Biophysical Journal, 1998. **75**(2): p. 917-925.

[115] Killian, J.A., *Hydrophobic mismatch between proteins and lipids in membranes.* Biochim Biophys Acta, 1998. **1376**(3): p. 401-15.

[116] Jensen, M.O. and O.G. Mouritsen. *Lipids do influence protein function-the hydrophobic matching hypothesis revisited.* Biochim Biophys Acta, 2004. **1666**(1-2): p. 205-26.

[117] Latorre, R. and J.J. Donovan. *Modulation of alamethicin-induced conductance by membrane composition.* Acta Physiol Scand Suppl, 1980. **481**: p. 37-45.

[118] Pan, J.J., T.T. Mills, S. Tristram-Nagle, and J.F. Nagle. *Cholesterol perturbs lipid bilayers nonuniversally.* Physical Review Letters, 2008. **100**(19): p. 198103.

[119] Rawicz, W., B.A. Smith, T.J. McIntosh, S.A. Simon, and E. Evans. *Elasticity, strength, and water permeability of bilayers that contain raft microdomain-forming lipids.* Biophysical Journal, 2008. **94**(12): p. 4725-4736.

[120] Boheim, G., W. Hanke, and H. Eibl. *Lipid phase transition in planar bilayer membrane and its effect on carrier- and pore-mediated ion transport.* Proc Natl Acad Sci U. S. A., 1980. **77**(6): p. 3403-3407.

[121] Boheim, G. and H.A. Kolb. *Analysis of Multi-Pore System of Alamethicin in a Lipid-Membrane .1. Voltage Jump Current Relaxation Measurements.* Journal of Membrane Biology, 1978. **38**(1-2): p. 99-150.

[122] Hanke, W., H. Eibl, and G. Boheim. *A new method for membrane reconstitution: fusion of protein-containing vesicles with planar bilayer membranes below lipid phase transition temperature.* Biophys Struct Mech, 1981. **7**(3): p. 131-7.

[123] Cantor, R.S., *Lipid composition and the lateral pressure profile in bilayers.* Biophysical Journal, 1999. **76**(5): p. 2625-2639.

[124] Abney, J.R., J. Braun, and J.C. Owicki. *Lateral interactions among membrane proteins. Implications for the organization of gap junctions.* Biophysical Journal, 1987. **52**(3): p. 441-454.

[125] Lewis, B.A. and D.M. Engelman. *Bacteriorhodopsin remains dispersed in fluid*

*phospholipid bilayers over a wide range of bilayer thicknesses.* Journal of Molecular Biology, 1983. **166**(2): p. 203-210.

[126] Reynwar, B.J. and M. Deserno. *Membrane composition-mediated protein-protein interactions.* Biointerphases, 2008. **3**(2): p. FA117-FA124.

[127] Mouritsen, O.G. and M. Bloom. *Mattress model of lipid-protein interactions in membranes.* Biophysical Journal, 1984. **46**(2): p. 141-153.

[128] Marčelja, S., *Lipid-mediated protein interaction in membranes.* Biochim Biophys Acta, 1976. **455**(1): p. 1-7.

[129] Hung, W.C., M.T. Lee, F.Y. Chen, and H.W. Huang. *The condensing effect of cholesterol in lipid bilayers.* Biophysical Journal, 2007. **92**(11): p. 3960-3967.

[130] Rawicz, W., K.C. Olbrich, T. McIntosh, D. Needham, and E. Evans. *Effect of chain length and unsaturation on elasticity of lipid bilayers.* Biophysical Journal, 2000. **79**(1): p. 328-339.

[131] Kittel, C., *Introduction to Solid State Physics*. 1976, New York: John Wiley &Sons.

[132] Wack, D.C. and W.W. Webb. *Synchrotron x-ray study of the modulated lamellar phase P beta ' in the lecithin-water system.* Physical Review A, 1989. **40**(5): p. 2712-2730.

[133] Sun, W.J., S. Tristram-Nagle, R.M. Suter, and J.F. Nagle. *Structure of the ripple phase in lecithin bilayers.* Proc Natl Acad Sci U. S. A., 1996. **93**(14): p. 7008-7012.

[134] Yang, L. and H.W. Huang. *Observation of a membrane fusion intermediate structure.* Science, 2002. **297**(5588): p. 1877-9.

[135] Münster, C., J. Lu, S. Schinzel, B. Bechinger, and T. Salditt. *Grazing incidence X-ray diffraction of highly aligned phospholipid membranes containing the antimicrobial peptide magainin 2.* European Biophysics Journal with Biophysics Letters, 2000. **28**(8): p. 683-688.

[136] Münster, C., A. Spaar, B. Bechinger, and T. Salditt. *Magainin 2 in phospholipid bilayers: peptide orientation and lipid chain ordering studied by X-ray diffraction.* Biochimica Biophysica Acta, 2002. **1562**(1-2): p. 37-44.

[137] Hub, J.S., T. Salditt, M.C. Rheinstadter, and B.L. de Groot. *Short-range order and collective dynamics of DMPC bilayers: a comparison between molecular dynamics simulations, X-ray, and neutron scattering experiments.* Biophysical Journal, 2007. **93**(9): p. 3156-3168.

[138] Huang, H.W., *Molecular mechanism of antimicrobial peptides: the origin of cooperativity.* Biochim Biophys Acta, 2006. **1758**(9): p. 1292-302.

[139] Bak, M., R.P. Bywater, M. Hohwy, J.K. Thomsen, K. Adelhorst, H.J. Jakobsen, O.W. Sorensen, and N.C. Nielsen. *Conformation of alamethicin in oriented phospholipid bilayers determined by N-15 solid-state nuclear magnetic resonance.* Biophysical Journal, 2001. **81**(3): p. 1684-1698.

[140] Mills, T.T., S. Tristram-Nagle, F.A. Heberle, N.F. Morales, J. Zhao, J. Wu, G.E. Toombes, J.F. Nagle, and G.W. Feigenson. *Liquid-liquid domains in bilayers detected by wide angle X-ray scattering.* Biophysical Journal, 2008. **95**(2): p. 682-690.

[141] Chen, L., Z. Yu, and P.J. Quinn. *The partition of cholesterol between ordered and fluid bilayers of phosphatidylcholine: a synchrotron X-ray diffraction study.* Biochim Biophys Acta, 2007. **1768**(11): p. 2873-2881.

[142] Gandhavadi, M., D. Allende, A. Vidal, S.A. Simon, and T.J. McIntosh. *Structure, composition, and peptide binding properties of detergent soluble bilayers and detergent resistant rafts.* Biophysical Journal, 2002. **82**(3): p. 1469-1482.

[143] Angelova, A., R. Ionov, M.H.J. Koch, and G. Rapp. *Interaction of the peptide antibiotic alamethicin with bilayer- and non-bilayer-forming lipids: Influence of increasing alamethicin concentration on the lipids supramolecular structures.* Archives of Biochemistry and Biophysics, 2000. **378**(1): p. 93-106.

[144] North, C.L., M. Barranger-Mathys, and D.S. Cafiso. *Membrane orientation of the N-terminal segment of alamethicin determined by solid-state 15N NMR.* Biophysical Journal, 1995. **69**(6): p. 2392-2397.

[145] Spaar, A., C. Munster, and T. Salditt. *Conformation of peptides in lipid membranes studied by X-ray grazing incidence scattering.* Biophysical Journal, 2004. **87**(1): p. 396-407.

[146] Martinac, B. and O.P. Hamill. *Gramicidin A channels switch between stretch activation and stretch inactivation depending on bilayer thickness.* Proc Natl Acad Sci U S A, 2002. **99**(7): p. 4308-4312.

[147] Perozo, E. and D.C. Rees. *Structure and mechanism in prokaryotic mechanosensitive channels.* Curr Opin Struct Biol, 2003. **13**(4): p. 432-442.

[148] Suchyna, T.M., S.E. Tape, R.E. Koeppe, 2nd, O.S. Andersen, F. Sachs, and P.A. Gottlieb. *Bilayer-dependent inhibition of mechanosensitive channels by neuroactive peptide enantiomers.* Nature, 2004. **430**(6996): p. 235-240.

[149] Volinsky, R., S. Kolusheva, A. Berman, and R. Jelinek. *Microscopic visualization*

*of alamethicin incorporation into model membrane monolayers.* Langmuir, 2004. **20**(25): p. 11084-11091.

[150] Baumgart, T., S.T. Hess, and W.W. Webb. *Imaging coexisting fluid domains in biomembrane models coupling curvature and line tension.* Nature, 2003. **425**(6960): p. 821-4.

[151] Veatch, S.L. and S.L. Keller. *Separation of liquid phases in giant vesicles of ternary mixtures of phospholipids and cholesterol.* Biophysical Journal, 2003. **85**(5): p. 3074-3083.

# List of Publications

1) Jianjun Pan, S. Tristram-Nagle, and J. F. Nagle, Effect of cholesterol on structural and mechanical properties of membranes depends on lipid chain saturation. Submitted to Physical Review E.

2) Jianjun Pan, D. P. Tieleman, J. F. Nagle, N. Kučerka, and S. Tristram-Nagle, Alamethicin in lipid bilayers: combined use of x-ray scattering and MD simulations. Biochimica et Biophysica Acta, 1788 (2009), 1387-1397.

3) Jianjun Pan, T. T. Mills, S. Tristram-Nagle, and J. F. Nagle, Cholesterol perturbs lipid bilayers nonuniversally. Physical Review Letters, 100 (2008), 198103.

4) Jianjun Pan, S. Tristram-Nagle, N. Kučerka, and J. F. Nagle, Temperature dependence of structure, bending rigidity and bilayer interations of DOPC bilayers. Biophysical Journal, 94 (2008), 117-124.

5) A. I. Greenwood, Jianjun Pan, T. T. Mills, J. F. Nagle, R. M. Epand, and S. Tristram-Nagle, CRAC motif peptide of the HIV-1 gp41 protein thins SOPC membranes and interacts with cholesterol. Biochimica et Biophysica Acta, 1778 (2008), 1120-1130.

6) N. Kučerka, J. D. Perlmutter, Jianjun Pan, S. Tristram-Nagle, J. Katsaras, and J. N. Sachs, The effect of cholesterol on short- and long-chain monounsaturated lipid bilayers as determined by molecular dynamics simulations and x-ray scattering. Biophysical Journal, 95 (2008), 2792-2805.

7) S. D. Guler, D. D. Ghosh, Jianjun Pan, J. C. Matthai, M. L. Zeidel, J. F. Nagle, and S. Tristram-Nagle, Effects of ether vs. ester linkage on lipid bilayer structure and water permeability. Chemistry and Physics of Lipids, 160 (2009), 33-44.

8) D. J. Kim, N. Akhunzada, J. C. Mathai, Jianjun Pan, M. Zeidel, J. F. Nagle, and S. Tristram-Nagle, Structure and water permeability of fully hydrated diphytanoylPC. Manuscript in preparation.